International Journal of Hydrogen Energy 101 (2025) 173–211

Contents lists available at ScienceDirect

International Journal of Hydrogen Energy

journal homepage: www.elsevier.com/locate/he

Next frontier in photocatalytic hydrogen production through CdS heterojunctions

Aminul Islam [a,b,c,**], Abdul Malek [a,b], Md. Tarekul Islam [d], Farzana Yeasmin Nipa [a], Obayed Raihan [e], Hasan Mahmud [f], Md. Elias Uddin [d], Mohd Lokman Ibrahim [g], G. Abdulkareem-Alsultan [h], Alam Hossain Mondal [i], Md. Munjur Hasan [j], Md. Shad Salman [k], Khadiza Tul Kubra [j], Md. Nazmul Hasan [l], Md. Chanmiya Sheikh [m], Tetsuya Uchida [m], Adiba Islam Rasee [j], Ariyan Islam Rehan [l], Mrs Eti Awual [k], Mohammed Sohrab Hossain [j], R.M. Waliullah [k], Md. Rabiul Awual [n,*]

[a] Department of Petroleum and Mining Engineering, Jashore University of Science and Technology, Jashore-7408, Bangladesh
[b] Hydrogen energy and CO2 conversion Lab, Department of Petroleum and Mining Engineering, Jashore University of Science and Technology, Jashore-7408, Bangladesh
[c] College of Engineering, Korea University, 145 Anam-ro, Seongbuk-gu, Seoul 02841, Republic of Korea
[d] Department of Leather Engineering, Faculty of Mechanical Engineering, Khulna University of Engineering and Technology, Khulna 9203, Bangladesh
[e] Department of Pharmaceutical Sciences, College of Health Sciences and Pharmacy, Chicago State University, 9501 S. King Drive, DH 3015, Chicago, IL 60628, USA
[f] Bangladesh Energy and Power Research Council (BEPRC), IEB Bhaban (11 th Floor), Ramna, Dhaka-1000, Bangladesh
[g] School of Chemistry and Environment, Faculty of Applied Sciences, Universiti Teknologi MARA, 40450, Shah Alam, Selangor, Malaysia
[h] Catalysis Science and Technology Research Centre, Faculty of Science, Universiti Putra Malaysia, Serdang 43400, Malaysia
[i] USAID - Bangladesh Advancing Development and Growth through Energy (BADGE) Project, Tetra Tech, House 10/C, Level 3&4, Road 90, Gulshan 2, Dhaka 1212, Bangladesh
[j] Department of Chemistry, Graduate School of Science, Osaka University, Osaka 560-0043, Japan
[k] Institute for Chemical Research, Kyoto University, Gokasho, Uji, Kyoto 611-0011, Japan
[l] Department of Chemistry, School of Science, The University of Tokyo, 7-3-1 Bunkyo-ku, Tokyo 113-0033, Japan
[m] Division of Applied Chemistry, Graduate School of Natural Science and Technology, Okayama University, 1-1 Tsushima-naka, 3-Chome, Okayama 700-8530, Japan
[n] Western Australian School of Mines: Minerals, Energy and Chemical Engineering, Curtin University, GPO Box U 1987, Perth, WA, 6845, Australia

ARTICLE INFO

Keywords:
H_2
Sustainability
Photocatalytic
Photo-stability
Heterojunction
CdS

ABSTRACT

Photocatalytic hydrogen (H_2) generation via solar-powered water splitting represents a sustainable solution to the global energy crisis. Cadmium sulfide (CdS) has emerged as a promising semiconductor photocatalyst due to its tunable bandgap, high physicochemical stability, cost-effectiveness, and widespread availability. This review systematically examines recent advancements in CdS-based heterojunctions, categorized into CdS-metal (Schottky), CdS-semiconductor (p-n, Z-scheme, S-scheme), and CdS-carbon heterojunctions. Various strategies employed to enhance photocatalytic efficiency and stability are discussed, including band structure engineering, surface modification, and the incorporation of crosslinked architectures. A critical evaluation of the underlying photocatalytic mechanisms highlights recent efforts to improve charge separation and photostability under operational conditions. This review highlights the challenges and opportunities in advancing CdS-based photocatalysts and provides a direction for future research. The insights presented aim to accelerate the development of efficient and durable CdS-based photocatalysts for sustainable H_2 production.

* Corresponding author. Western Australian School of Mines, Minerals, Energy and Chemical Engineering, Curtin University, GPO Box U 1987, Perth, WA, 6845, Australia.

** Corresponding author. Department of Petroleum and Mining Engineering, Jashore University of Science and Technology, Jashore-7408, Bangladesh.

E-mail addresses: aminul_pme@just.edu.bd (A. Islam), munjur.hasan@dims-bd.org (Md.M. Hasan), khadiza.kubra@dims-bd.org (K.T. Kubra), adiba.islam@dims-bd.org (A.I. Rasee), eti.awual@dims-bd.org (M.E. Awual), sohrab.hossain@dims-bd.org (M.S. Hossain), r.waliullah@dims-bd.org (R.M. Waliullah), rabiul.awual@dims-bd.org, rawual76@yahoo.com, rabiul.awual@curtin.edu.au (Md.R. Awual).

https://doi.org/10.1016/j.ijhydene.2024.12.300
Received 21 October 2024; Received in revised form 27 November 2024; Accepted 17 December 2024
Available online 31 December 2024

1. Introduction

Energy plays an emergent role in economic activity. The majority of the energy produced currently comes through fossil fuels'consumption. The extensive use of fossil fuel-based energy resources causes undesirable side effects including environmental pollution, global warming and climate change [1,2]. The supply of fossil fuel is not unlimited. The explosive enhancement of urbanization and manufacturing is the root reason for the world's energy resource shortage. It is crucial to address both present environmental risks and emerging energy difficulties as the global energy emergency intensifies. It is urgently necessary to switch from carbon-rich non-renewable resources to zero-carbon, safe, and renewable sources of energy in order to address both of these major concerns. Numerous initiatives for developing new and sustainable energy sources are being stimulated by the growing public's consciousness of the impacts of both the energy crisis and global warming. This necessitates promoting studies on environmentally friendly innovations to tackle those mentioned threats and energy challenges [3,4].

The advancement of technology to generate renewable energy has drawn an enormous amount of attention. Hydrogen (H_2) has been considered to be the fuel of the future in this context. H_2 fuel burns cleanly and has an extremely particular enthalpy of combustion. H_2 fuel has garnered a lot of interest as a possible environmentally friendly substitute to fossil fuels for addressing the present problem of energy and degradation of the environment [5]. In addition to being directly utilized in combustion engines to power automobiles like other fossil fuels, carbon-free H_2 can also be utilized to generate electricity through fuel cell technology. At the moment, the steam reforming of methane is the main technique for acquiring H_2 from natural gas, and the H_2 generated by this process is still a fossil fuel unlike a source of renewable energy [6,7]. The creation of a successful H_2 preparation strategy independent of the usage of fossil fuels is one of the fundamental challenges for the practical utilization of H_2 fuel. Amongst the available renewable energy options, if effective absorption and conversion are rendered possible, sunlight can become the greenest and cleanest energy source on Earth [8,9].

A substantial enhancement has been observed recently in the study of developing a process of turning sunlight into useable chemical energy. An approach for generating carbon-free H_2 by harnessing limitless solar energy is water splitting to produce H_2 photocatalytically. This approach has quickly become an effective and available option [10]. To minimize the degradation of hazardous elements and the reliance on fossil fuels in renewable energy production, it is essential to optimize the hydrogen (H2) manufacturing process to reduce energy consumption [11,12]. As well solar energy is the most likely alternative to other renewable energy sources since it has a lot of benefits them, including extensively existing, biodegradable, and releasing no hazardous gases [13]. The semiconductor-based photocatalysis by visible light has been regarded as one of the most likely approaches for concurrently resolving the issues of environmental pollution as well as the worldwide energy crisis [14,15].

Since the first time, Fujishima used TiO_2 to produce photocatalytic H_2 from water in 1972 [16,17]. To intensify H_2 production efficiency, researchers have concentrated mostly on TiO_2's photocatalytic efficiency. Because of TiO_2's wide bandgap (3.2 eV), the analogous photocatalytic H_2 evolution process can onl be carried out upon only illumination of UV light, which is merely 4% of sunlight [18]. In recent decades, numerous semiconductors are being explored as photocatalysts to split water. The majority of them suffer with issues including high cost, rarity on Earth, toxicities, poor stability, and ineffectiveness. Research into low-cost, ecologically friendly, metal-free semiconductor photocatalysts with incredibly potent and reliable performance is still very appealing. It is crucial to explore photocatalysts that are made from semiconductors of appropriate narrow bandgap with the goal of achieving high photocatalytic H_2 evolution rates upon illumination of visible light. It is imperative to explore semiconductor photocatalysts with suitable narrow bandgaps to attain significant rates of H_2 production by visible-light illumination.

Metal sulfides (MSs) have tremendous potential for developing efficient photocatalysts for the production of H_2 by exposing them to visible light because of their exceptional semiconductor features of significant specific surface areas and suitable band structures [19,20]. As an n-type photocatalyst of a tiny bandgap of almost 2.4 eV, CdS performs as a potent photocatalyst for H_2 production attributed to its auspicious negatively conduction band (CB) potential for converting H^+ to H_2 [21]. Apart from CdS, ZnS, MoS_2, and CuS having suitable semiconductor features were further extensively explored for H_2 production in photocatalysis [22–24]. The metal-sulfide photocatalysts also have some unavoidable limitations that are challenging to address at the present stage of the study. Even though CdS possesses outstanding semiconductor characteristics that facilitate effective visible light photocatalytic H_2 evolution, the relevant photoactivities still remain difficult to scale up to industrial levels. CdS-based photocatalysts typically have photo corrosion problems throughout the photocatalytic H_2 generation process, which leads to insufficient photostability. The fast charge carriers recombination renders the photoactivity of CdS insufficient [21,25].

To address these issues, it is urgent to develop a more effective Cds-based photocatalyst. CdS photocatalysts can be modified using several approaches, such as chemical doping, utilization of distinctive morphologies, surface functionalization, loading with co-catalysts and carbon compounds, and formation of heterojunctions. In recent years, the effectiveness of photocatalytic production of H_2 of CdS-based heterojunction has been optimized via significant research endeavors. Developing photocatalytic heterojunctions is an efficient path through coupling semiconductors of acceptable bandgap. The formation of heterojunction will enhance the function of photocatalysts by promoting charge-carrier separation. The electrons and holes migrate efficiently to the respective photocatalysts due to the formation of an electric field at the interface, generated by the transfer of charge carriers. This electric field enhances the photocatalytic process by facilitating the rapid separation and migration of photo-induced electron-hole pairs within the heterojunction, thereby promoting charge conduction and improving the efficiency of the photocatalytic reactions [26,27].

Various CdS-based heterojunctions were extensively investigated to improve their photocatalytic functions. Enhanced H_2 production was achieved with MoS_2/CdS heterostructures due to the efficient charge separation facilitated by the heterojunction interface. Kafadi et al. [28] synthesized CdS nanorods (NRs) combined with ultrathin Ti_3C_2 MXene sheets via a solvothermal route, demonstrating superior photocatalytic activity. Schottky heterostructures provided efficient charge partitioning and a reduced Schottky barrier for H_2 generation under solar irradiation, attributed to their unique interfacial properties [29,30]. Several recent studies focused on the advancement of CdS-based heterojunctions for energy and environmental applications [31,32]. However, a systematic investigation into the application of these heterojunctions for water-splitting photocatalysis remains limited, highlighting the need for further development. This review presents an in-depth evaluation of the mechanisms underlying photocatalytic H_2 evolution and the factors influencing efficiency. The crystal structures, optical and electronic properties, and synthesis strategies of CdS are summarized. Additionally, the photocatalytic mechanisms of diverse CdS-based heterojunctions, including their impact on performance and photostability, are critically assessed. Challenges and opportunities for improving CdS heterojunctions are outlined, with potential solutions suggested. The novelty of this review lies in providing a comprehensive analysis of CdS-based heterojunctions while offering recommendations for advancing their development as efficient photocatalysts for sustainable H_2 production.

2. Fundamental mechanisms of photocatalysis over CdS for H_2 evolution

The sunlight is transformed into a form of chemical energy through the process of photo-catalysis. For environmental remediation, it is incredibly efficient, environmentally friendly, and sustainable. Photocatalytic splitting of water is considered as an artificial form of photosynthesis, due to its similarity to the photosynthesis process which takes place in green plants under sunlight [33]. Utilizing the concept of photo-catalysis, H_2 could be generated from organic materials found in wastewater or even from freshwater by utilizing the rays of sunlight [34]. This process involves the redox reactions of water with electrons and holes [35]. For the production of H_2, a photocatalytic system usually needs a photoreactor, reactant, photocatalyst, and supply of light. Water alone or even with a mixture containing a sacrificial reagent can act as the reactant. Either visible or ultraviolet light is required to be utilized by a photocatalyst to allow for it to function properly. The photocatalysts that absorb visible light may ensure that they can capture a considerable portion of the energy released by the sun [36]. The interaction of light, photocatalyst, and reactants must be effective for hydrogen synthesis to be efficient [37]. Through intricating multi-step procedures, the photo-excited charges of a semiconductor are capable of converting sunlight into chemical energy during photo-catalysis.

Basically, through six complementary and crucial steps, a photocatalyst produces H_2 by photocatalytic splitting of water when it is exposed to light. 1) Photo-excitation: Electrons in the valence band (VB) of a photocatalyst (PC) become induced when it is exposed to photons with energies higher or equal to their forbidden energy gap. 2) Separation: photo-excited holes (h^+) in VB are released as photo-induced electron migrates to the conduction band (CB) (Eq. (1)). 3) Migration: photo-induced charges (electron-hole) migrate to the semiconductor periphery or interface. 4) Reduction reaction: the migrated photo-excited electrons at the surface of the photocatalyst lead to a reduction reaction. 5) Oxidation reaction: the migrated photo-excited holes at the surface of the photocatalyst lead to an oxidation reaction. 6) Recombination: the pairs of photo-excited electrons-holes recombine within the bulk of the photocatalysts or on the surfaces of photocatalysts (Eq. (2)), thereby releasing energy [38]. Water breaks down into H^+ in the oxidation reaction (Eq. (3)), and H^+ then acquires electron to generate H_2 in the reduction reaction (Eq. (4)). When CB and VB are upper and inferior to potentials of reduction and oxidation, correspondingly, redox reactions conduct on photocatalyst surface. As strong oxidants, photo-excited holes are able to oxidize water (Eq. (3)). Although the reactions perform at temperatures higher than 2070 K with the thermal dissociation of water. But by employing a photocatalyst and light that has an energy above the band-gap energy, it is possible to split water at ambient temperature [39].

$$PC \xrightarrow{h\nu} PC(e^-) + PC(h^+) \tag{1}$$

$$PC(e^-) + PC(h^+) \rightarrow PC \tag{2}$$

$$H_2O + 2h^+ \rightarrow \frac{1}{2}\,O_2 + 2H^+ \tag{3}$$

$$2e^- + 2H^+ \rightarrow H_2 \tag{4}$$

Electron-hole recombination is the main barrier to split water in photocatalysis. Through releasing unproductive heat, a pair of electrons and a hole might recombine. The effectiveness of H_2 generation is reduced as a result. Because of the rapid recombination of charges, conducting water splitting for producing H_2 is challenging through utilizing photo-catalysts, especially in pure water. That is why sacrificial reagents and electrolytes are frequently employed while investigating the photocatalytic splitting of water. The CB electrons and VB holes are neither reducing or oxidizing the electrolytes. Electrolytes serve as a means of transferring electrons and ions to nearby semiconductors. The acceleration of the water-splitting process during photocatalysis is provided by its reagents. To boost charges-separation, holes undergo reactions with reagents or donors of electrons [40]. Due to the limitations associated with hydrogen production from freshwater, maximizing the performance of photocatalysis can be achieved by analyzing the thermodynamics related to reduction-oxidation potentials and bandgap energies. In addition to the kinetics process, the basic thermodynamic conditions for a specific photo-catalytic process must be fulfilled. The multi-electron water-splitting process is endothermic [41]. Oxidation and reduction are both reactions that occur in this process, which is the thermodynamically uphill reaction (Eq. (5) and (6)), and has a change of typical Gibbs free energy of 237 kJ mol^{-1} [42]. Semiconductor's photocatalytic performances are influenced by their CB, VB, and band gap. The half-reactions for the production of O_2 and H_2 are described in Eqs. (5) and (6), correspondingly.

$$2H_2O \rightarrow 4H^+ + 4e^- + O_2\,;\, E^o_{ox} = +0.82\ \text{V vs. NHE},\ p^H = 7 \tag{5}$$

$$4H^+ + 4e^- \rightarrow 2H_2\,;\, E^o_{red} = -0.41\ \text{V vs. NHE},\ p^H = 7 \tag{6}$$

Water is unable to dissociate under normal circumstances until the potential difference between the two half processes is more than 1.23 eV. The energy barrier for the whole operation is 1.23 eV, making it thermodynamically nonspontaneous [43], which could be overcome using photocatalysts having optimum band-gap and redox potentials appropriate for the reduction of protons. In an ideal photocatalyst, the presence of oxidation and reduction potentials within the band gap is imperative to facilitate the generation of desired products. The reduction process for H^+/H_2 conducts at a reduction potential of −0.41 eV vs NHE ($p^H = 7$) and the oxidation process for O_2/H_2O conducts at +0.82 eV vs NHE ($p^H = 7$). The upper edge of VB needs to have a higher positive potential compared to the oxidation potential of O_2/H_2O. On the other hand, the bottom edge of CB ought to be larger negative to the potential of H^+ reduction into H_2 [41]. A single semiconductor with a lower negative CB would be less capable of conducting a reduction process. By coupling to other semiconductors of higher negative CB, transportation of electrons onto neighboring semiconductors for production of H_2 is possible by the reduction of H^+.

Due to the discrepancy between the quantity of absorbed photons and the incident photons, in a simple photocatalysis, the AQY is always lesser than the real QY. The photoelectrochemical and photocatalytic water splitting reactions correlate to a further parameter during solar to H_2 conversion efficiency (STH) (Eq. (7)) to demonstrate the water splitting effectiveness [44].

$$STH = \left(\frac{\text{mmoles of } H_2 \times 237\ \text{kJ mol}^{-1}}{P_{total}\ (\text{mW cm}^{-2}) \times Area\ (cm^2) \times t\ (sec)}\right)_{A.M_{1.5G}} \text{x } 100\% \tag{7}$$

Numerous reduction processes might be driven by their photo-excited electrons with greater reduction potentials migrating to the CdS with higher work function. The related semiconductor/CdS hybrids were widely used in numerous photo-catalytic sectors. During the last few years, several engineering methods have made substantial advancements in improving kinetic processes and meeting thermodynamic requirements [44]. Such engineering approaches might be separated into kinetics and thermodynamics. By creating excellent heterojunction interfaces, very effective charge-transfer nanostructures, and exceptionally reactive surfaces and cocatalysts [48], CdS could be employed to implement each of these approaches for improving photocatalysis kinetically. The development of broad-spectrum responding photocatalysts and the appropriate composition engineering of large band-gap semiconductors are two typical instances of thermodynamic approaches. Due to the much greater value of the Coulomb constant than the gravitational constant, the faster recombination of charge carriers on the surface of semiconductor photocatalysts poses a significant challenge for the development of viable photocatalysis techniques in large-scale commercialization [45]. From the perspective of practical

implementation, developing appropriate CdS-based heterojunctions has been determined to be one of the most likely techniques to construct efficient photo-catalysts with successfully separated photo-induced electron-hole pairs. Numerous CdS-based hetero-junctions have been developed for employing extensively in photocatalysis up to this moment [45].

3. Insights into the photocatalytic properties of CdS

3.1. Electronic properties of CdS

The visible light response and photo-generated carrier redox capabilities of CdS semiconductor materials are greatly influenced by the distinct band structures. The impact on photocatalyst performance is directly observed [46]. The photocatalysis effectiveness is significantly affected by the band configuration of the semiconductors [46]. A semiconductor's band structure, comprising VB, CB, and forbidden bandgap (E_g), serves as a significant component in assessing photo-stimulation outcomes [44]. During photo-stimulation, electrons are photo-excited to CB from VB, releasing behind holes. Simultaneously, the CB is filled with electrons. In wide bandgap semiconductors, the photo-excited electrons face a barrier preventing them from reaching higher energy-band locations. However, following a path established by previously formed internal electric fields (IEF), photo-induced electron-hole pairs can overcome potential barriers. This successfully enables to separation and transfer of electron-hole pairs through the depletion layer of contact, preventing charge recombination [44,47]. The Fermi level is situated near CB of n-type with a difference of 0.1 V or 0.2 V. It exists near VB of p-type. In CdS, the top edge of VB is exploited by the S 3p orbital, while the bottom edge of CdS CB is contributed by Cd 5s and 5p orbitals. Cd 3d orbital dominates the bottom location of CB [48,49]. The thermodynamic requirements for variously explored photocatalysis, notably water splitting, are fulfilled by CB and VB locations of CdS, which have been identified at −0.93 V and 1.47 V, respectively, vs NHE. Precise bandgap of CdS makes it suitable for absorbing light in the visible region. VB and CB locations of a photocatalyst signify its redox ability and photocatalytic performance. CdS emerges as a semiconductor with high potential quantum efficiency (QE) for photocatalysis activated by irradiation of light in visible range [50]. The photocatalytic function of bare CdS is constrained through the separation of charges, the charges transportation mechanism, and the recombination of charges [51], despite its broad optical absorption ability and substantial electron reduction potentiality. Achieving optimal photocatalytic efficiency and long-term reliability remains a significant challenge for CdS photocatalysts [52]. Numerous initiatives have been undertaken to improve the effectiveness of CdS-based photocatalysts in photocatalysis applications.

3.2. Optical properties of CdS photocatalysts

The ultraviolet (UV) range, visible range, and near-infrared (NIR) range are distinct regions of the electromagnetic spectrum, each offering varying advantages and limitations for photocatalytic hydrogen production. while each range of the electromagnetic spectrum has its merits, visible light stands out as the most practical and effective option for photocatalytic H_2 evolution.

Visible light-driven photocatalysts can harness the abundant sunlight, making them well-suited for sustainable and energy-efficient hydrogen generation processes. Researchers continue to focus on enhancing visible light-responsive photocatalysts, solidifying their importance in the quest for clean and renewable energy sources. Fig. 1 displays the photocatalytic H_2 production rates for various heterojunction photocatalysts illuminated with different wavelengths of light, alongside their corresponding optical absorbance wavelengths. UV range photocatalysts, including $Ni(OH)_2$/CdS [53] and NiS/Mo_2C/CdS [54], had shown to exhibit high hydrogen production rates (40.18 and

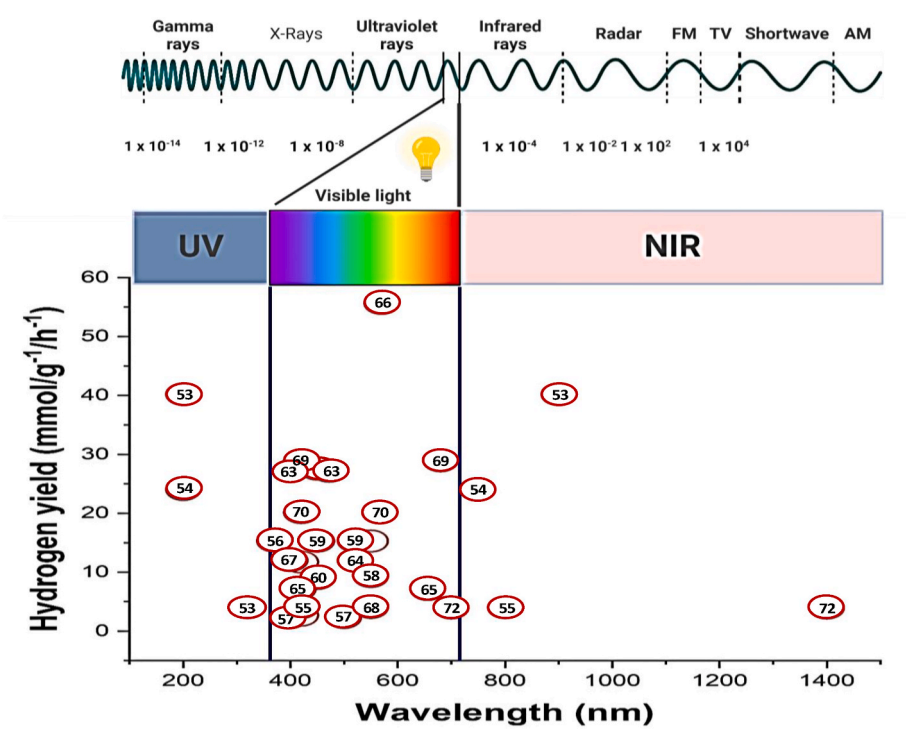

Fig. 1. Photocatalytic H_2 production rate over several heterojunction photocatalysts under the illumination of light of different wavelengths and their corresponding optical absorbance wavelength. UV Range: ($Ni(OH)_2$/CdS [53]; NiS/Mo_2C/CdS [54]; CuMOF/CdS [55]; 40 wt% CdS/$W_{18}O_{49}$ (CW40) [56]).Visible range: (TiO_2/CdS [57]; CdS/PT [58]; g-C_3N_4/CdS [59]; Ti_3C_2/ZIS/CdS [60]; 2D MX-CdS/WO_3 [61]; NiS/Mo_2C/CdS [54]; CdS@Nb_2O_5/Nb_2CT_x [62]; $Cd_xZn_{1x}In_2S_4$–CdS–MoS_2 [63]; Ni_2P–SNO/CdS-D [64]; CdS/NiAl LDH [65]; NiCoP-g-C_3N_4/CdS [66]; CdS@$W_{18}O_{49}$ [67]; ZnO/CdS hierarchical [68]; CdS/g-C_3N_4/$Ni(OH)_2$ [69]; $Ni(OH)_2$/CdS NFlake [70]; TiO_2–$Ni(OH)_2$/CNT/CdS [71]; CuMOF/CdS [55]). NIR range: (MnO_2@CdS [72]; $Ni(OH)_2$/CdS [53]).

24.03 mmol g^{-1} h^{-1}, respectively). However, they require UV light for activation, which is only a small fraction of the solar spectrum. Visible range photocatalysts, such as CdS/PT [58], g-C_3N_4/CdS [59], 2D MX-CdS/WO_3 [61], and NiCoP-g-C_3N_4/CdS [66], can utilize a extended range of solar spectrum and have also been shown to exhibit high hydrogen production rates (9.28, 15.3, 27.5, and 55.63 mmol g^{-1} h^{-1}, respectively). NIR range photocatalysts, such as MnO_2@CdS [72], are still under development and have lower hydrogen production rates (3.94 mmol g^{-1} h^{-1}) than UV and visible range photocatalysts. Visible-range photocatalysts are important because they can utilize a wider range of the solar spectrum, which makes them more efficient for solar-driven hydrogen production. Additionally, visible-range photocatalysts are generally more stable than UV-range photocatalysts, which makes them more suitable for long-term operation. The maximum H_2 evolution efficiency reported in the table is 55.63 mmol g^{-1} h^{-1} for NiCoP-g-C_3N_4/CdS upon visible light irradiation [66]. The lowest hydrogen production rate reported in the table is 3.94 mmol g^{-1} h^{-1} for MnO_2@CdS [72] by illumination in the NIR range. Visible range photocatalysts are the most promising class of photocatalysts for solar-driven hydrogen production because of their high efficiency and stability. NiCoP-g-C_3N_4/CdS is the most promising visible range photocatalyst reported in the table, with a hydrogen evolution of 55.63 mmol g^{-1} h^{-1} yielding rate [66]. The importance of visible range photocatalysts is evident from their ability to efficiently harness solar energy for hydrogen production, with significantly higher rates compared to both UV and NIR range photocatalysts. The development of visible range photocatalysts holds great promise for sustainable and efficient hydrogen production processes. Performances of CdS-based heterojunction photo-catalysts for H_2 production from water splitting and their corresponding optical absorbance wavelength are presented in Table 1.

The effectiveness of the photocatalysis for producing H_2 in a usual photocatalytic process is largely dependent on how well solar light is harvested, how well charges are generated, and how well charges are transported. The photocatalytic performance was increased by the speed up separation of photo-induced charges. Combining of more than one substance to built heterojunction at nanoscale range is a successful method for enhancing spatial charges-separation and photocatalytic performance. With appropriate band structure, CdS for its visible light response ability displayed a significant role for reducing water to H_2.

Table 1
Evaluation of CdS-based heterojunction photo-catalysts in the context of H_2 evolution from water splitting, along with analysis of their associated optical absorbance wavelengths.

Catalysts	H_2 evolution rate (mmol g^{-1} h^{-1})	Light response (nm)	Reference
Ni(OH)2/CdS NFlake	20.14	420–566	[70]
CdS@W18O49	11.732	420	[73]
TiO2/CdS	2.32	400–500	[57]
CdS/PT	9.28	<550	[58]
Ti3C2/ZIS/CdS	8.93	450	[60]
NiS/Mo2C/CdS	24.03	200 to 750	[54]
TiO2–Ni(OH)2/CNT/CdS	12	>400	[71]
Ni(OH)2/CdS	40.18	200–900	[53]
CuMOF/CdS	4.017	420, 320-550−800	[55]
40 wt% CdS/$W_{18}O_{49}$ (CW40)	15.4	370	[56]
g-C3N4/CdS	15.3	520, 450-550	[59]
2D MX-CdS/WO3	27.5	450	[61]
CdS@Nb2 O5/Nb2CTx	2.7158	>420	[62]
CdxZn1xIn2S4–CdS–MoS2	27.14	400, 471.9	[63]
Ni2P–SNO/CdS-D	11.992	520	[64]
CdS/NiAl LDH	7.0918	415 to 656	[65]
NiCoP-g-C3N4/CdS	55.63	570	[66]
ZnO/CdS hierarchical	4.134	550	[68]
CdS@g-C3N4/Ni(OH)2	28.91	420–680	[69]
MnO2@CdS	3.94	700 to 1400	[72]
Ni–Ni(OH)2/CdS	428	500–800	[74]

Some limitations including high photo-corrosion, faster recombination of charges, lesser reactive sites as well as higher water splitting overpotential were identified over on modified CdS sample. These limitations lead to diminish QE in photocatalysis. The construction of heterojunction by coupling of CdS with appropriate substances could lead to accelerate separation of charges, which prevented photo-corrosion of the semiconductors. The photo-current, photo-luminescence (PL) and electro-chemical impedance spectroscopy (EIS) indicate the mechanisms of separation and transportation of charges of a photocatalyst. For example, co-doping of Bi and Ni onto CdS's surface exhibited excellent charge-carriers separation [75]. The Bi_{10}–Ni_6–CdS showed a significant photo-current density of almost 18 μA cm^{-2}, which indicatinted its optical-absorption capability. The lower resistance of electron mobility was indicated by the lowest arc radious of EIS of Bi_{10}–Ni_6–CdS [75]. The obtained Bi–Ni–CdS coralloid exhibited a significant efficiency for photocatalytivc H_2 production upon illumination of visible-light (≥400 nm). The Bi/Ni–CdS photocatalysts produced a mximum 5.2944 mmol g^{-1} h^{-1} yielding rate of H_2. This rate was 20-folds greater to that of CdS. By using a solvothermal technique, Ba et al. [76] prepared the 2D snow-flake CdS through the use of galvanic replacement by coating various Pd–Ni hollow alloys on CdS's surface. The maximum photo-current density of 42 mA cm^{-2} was observed over Pd–Ni/CdS sample. Photo-excited charges separation and enhance electric conductivity were improved by 2D CdS and Pd–Ni NPs. The transportation of electrons from CdS to Pd–Ni was greater to that of Pd–CdS. This enhancement was predominantly responsible for faster capture of electrons by Pd–Ni co-catalyst. The maximum H_2 production of 54 mmol g^{-1} h^{-1} yielding rate was achieved over Pd–Ni/CdS. This corresponds to QE of 63.97% at 420 nm. With coating of Zn-anchored C-layer on CdS's surface, charges separation was significantly increased [90]. The CdS@Zn–C photocatalyst's photo-current density was obtained up to 12 μA. This indicated that the CdS@Zn–C photocatalyst had accelerated charge separation. The higher photocurrent as well as the lesser Rct of EIS for CdS@Zn–C indicated that CdS@Zn–C was the remarkably efficient photocatalyst for the evolution of H_2. The optimum CdS@Zn–C displayed a remarkable evolution of H_2 with a 6.6 mmol g^{-1} h^{-1} yield rate. AQE of 13.1 % was also observed under illumination of 420 nm wavelength.

Mesoporous carbon matrix inclusion into photocatalysts substantially separated photo-induced charges, increased the durability of the substance, and prevented the recombination process. Banerjee et al. [77] prepared an MC-CdS sample through a facile route. The semiconductors' bandgap was run by mesoporous carbon matrix inclusion. The CdS's photostability was improved by promoting photocurrent responses through loading increasing of MC slowly. Compared to bare CdS NPs, the photocurrent response of about 25 μA cm^{-2} was remarkably larger. MC seemed to promote electrons' mobility through the porous and significantly reactive surface of mesoporous carbon, which was identified from the photo-current response. The lower arc radius (Rct) of 40-MC/CdS indicated the higher mobility of charges in CdS and MC. A maximum 37,641 μmol g^{-1} h^{-1} yielding rate of H_2 from water was obtained over the as-prepared photocatalyst in existence of CH_3OH.

Noble metals including Pt and Au are efficient co-catalysts. Electrons may be easily injected to precious metal NPs from semiconductor and rapid proton-reduction. The deficit and high-cost inhibit the usage of precious metals. Earth abundant and cost-effective metals necessity to be investigated. Several available and low-cost photocatalysts have benn studied including graphdiyne-CdS, Fe_2P–CdS, Ni_3S_2–CdS, Ni_2P–CdS, and so on [64,79,89]. Yang et al. [78] exhibited an excellent H_2 production over heterostructure composites of spatially charges separation. The as prepared MoP/CdS presented a fantastic H_2 evolution performance up to 13.88 mmol h^{-1} g^{-1} yielding rate and highly AQY of 66.7% using light of 420 nm wavelength. It was 1.44-times greater than that observed for Pt–CdS sample. The 2.5 wt% MoP-300/CdS exhibited very lesser arc radious than pure CdS and 2.5 wt% MoP-700/CdS samples, which suggested a smaller resistance of charge-mobility. A significant

photo-current of 1.4 μA was obtained over the optimal photocatalyst indicating a considerable photoelectrochemical function. The utmost proficient path to increase the photocatalytic performance of semiconductor is to develop 2D ultra-thin nanomaterials as co-catalysts. Liang et al. [79] fabricated the new 2D-1D Fe_2P–CdS photocatalyst. The optimized 11 wt % Fe_2P–CdS photocatalyst showed the maximum photocurrent density of 79.23 μA, while merely 7.73 μA photo-current was observed over CdS sample. The optimal 11 wt% Fe_2P–CdS photocatalyst exhibited a strong optical absorption performance and efficient separation photo-excited charges. These enhancement was benefitted owing to inclusion of Fe_2P NSs. EIS measurements revealed that arc radius of 11 wt% Fe_2P–CdS NSs' Nyquist plots was much lesser to CdS NSs. The electric conductivity of Fe_2P–CdS was increased efficiently by Fe_2P NSs. Upon irradiation of visible-light, an exceptional H_2 productivity of 207.82 mmol g^{-1} h^{-1} was determined over Fe_2P–CdS with 11% Fe_2P loading. This rate was significantly more compared to bare CdS.

NiS/CDs/CdS (NCCS) composites with excellent H_2 production efficiencies were reported by Wei et al. [80] without the use of noble metals. In contrast to unique CdS photocatalyst and binary composites such as NiS–CdS and CDs-CdS, the obtained NCCS composite showed noticeable enhancement of H_2 production. This performance was due to convenience of strong ability of absorbing light, electron buffering features of CDs, and the internally forming of p-n heterojunction. During exposure to light in visible region (>420 nm), the best ternary hybrid produced H_2 at a rate up to 1.4445 mmol g^{-1} h^{-1} yielding rate. This rate was 5.38-folds greater to pristine CdS spheres. Due to swift charges' recombination, bare CdS had a minimal photocurrent density. The increased photo-current of CDs-CdS indicated that CDs' deposition is advantageous for optical absorption and electron extracting. Compared to CDs-CdS and NiS–CdS, NiS-CDs-CdS sample had a substantially stronger photocurrent output. The NiS/CDs/CdS has a very high rate of photocatalytic release of H_2 owing to the combined advantages of CDs and flimsy NiS, which can minimize the recombination of charge-carrier. A brand-new and incredibly effective NiCoP/CdS/NiCoPi photocatalyst for H_2 production was constructed by Zhao et al. [81]. By employing sodium hypophosphate as a phosphorus source, during one phosphating phase, duplex co-catalysts were concurrently accumulated on CdS. In order to better understand interfacial charges-separation and migration in pristine CdS and 5 mol% Ni–CoP/CdS/Ni-CoPi, electrochemical studies were conducted. The surface impedance of 5 mol% Ni–CoP/CdS/Ni-CoPi mixture was lower compared topristine CdS. The addition of Ni–CoP/Ni-CoPi co-catalysts was advantageous of charges separation and transmission. CdS's photo-current greatly increased after dual-cocatalysts were loaded, whilst the impedance of the electricity and photo-luminescence emission sharply dropped, suggesting an improvement in charge-carriers' separation. It was claimed that the Ni–CoP co-catalyst donated electrons and speeded up the oxidation of sacrificial substances. NiCoPi co-catalyst taken electrons and encouraged the production of hydrogen. As a result, the evolution into hydrogen of this composite photocatalyst powered by visible light significantly boosted. Assuming a loading percentage of 5 mol%, CdS modifying by dual co-catalysts demonstrated an impressive H_2 evolution reached to 80.8 mmol g^{-1} h^{-1} yield rate. This rate was 202-folds better compared to that of unmodified. When CdS was treated with metal phosphide, this was the maximum enhancement factor. Additionally, it demonstrated impressive stability in an uninterrupted photo-catalytic testing with a 24 h. Various CdS-based heterojunction photocatalysts' H_2 generation rates are shown in Fig. 2 together with the corresponding photo-current responses.

Fig. 2 shows the photocurrent responses of CdS heterojunction in photocatalytic hydrogen production. Low current density with high hydrogen yield is a key factor in assessing the efficiency of photocatalysts. In this category, various photocatalysts demonstrate impressive hydrogen production rates even at low current densities, exemplifying their superior performance. For instance, Ni–Ni$(OH)_2$/CdS [74] exhibits a remarkable H_2 yield of 428 mmol g^{-1} h^{-1} at a current density of 60 mA cm^{-2}, highlighting the exceptional capability of this photocatalyst to efficiently convert light energy into hydrogen. Conversely, high current density with low hydrogen yield signifies less effective photocatalysts, leading to decreased hydrogen production. For example, TiO_2–Ni$(OH)_2$/CNT/CdS and CdS/CoO_x/Co-metal achieve only 12 mmol g^{-1} h^{-1} and 0.318 mmol g^{-1} h^{-1}, accordingly, at high current densities, reflecting their reduced ability to harness light energy for hydrogen generation [71,86]. Low current density with low hydrogen yield is associated with limited photocatalytic capabilities. Photocatalysts in this category, such as CdS/CeO_2 [98], and g-C_3N_4/CdS [102], exhibit low hydrogen production rates, indicating their suboptimal performance in converting light into hydrogen gas. Achieving low current density with high hydrogen yield is needed in the development of effective photocatalysts for sustainable and clean hydrogen production. These photocatalysts hold great promise for meeting the growing energy demands with minimal energy input. Photocurrent responses in the CdS-based heterojunction for photocatalytic H_2 production are presented in Table 2.

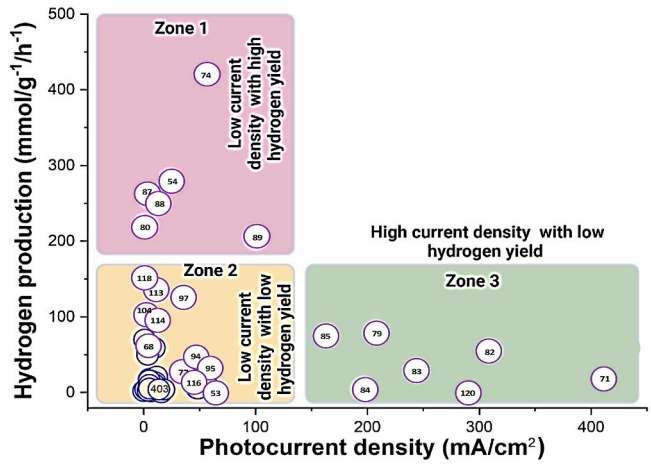

Fig. 2. Photocurrent response of several CdS-based heterojunction photocatalysts with corresponding H_2 production rate. High current density with low hydrogen yield: (TiO_2–Ni$(OH)_2$/CNT/CdS [71]; CQD/CdS [82]; CdS/NiO core-shell [83]; Fe_2P–CdS [79]; CdS/$BiVO_4$ [84]; MoP/CdS [85]; CdS/CoO_x/-Co-metal [120]). Low current density with high hydrogen yield: (Ni–Ni$(OH)_2$/CdS [74]; CdS/Mo_2C–NiS [54]; CdS@Au into Ultrathin Ti_3-xC_2T_y [87]; ultrathin CdS@BDC nanosheets [88]; NiS/CDs/CdS (NCCS) [80]; CdS–Ni_3S_2/NF [89]). Low current density with low hydrogen yield: (Bi_{10}/Ni_6–CdS [75]; CdS@Zn–C [90]; 40-MC-CdS [77]; MoP/CdS composites [78]; g-C_3N_4 NSs/CdS NPs [91]; Co_3O_4/CdS [92]; Cu_2S/CdS p-n [93]; CdS/ZnS (CSZS–VZn) [94]; $W_{18}O_{49}$/CdS [95]; CdS NR/CoS_x [96]; Pt–C_3N_4/CdS [97]; CdS/CeO_2 [98]; CdS/$W_{18}O_{49}$/g-C_3N_4 [99]; Co_9S_8/Cd/CdS [100]; NH_2-MIL-125 (Ti)/CdS [101]; g-C_3N_4/CdS [102]; CdS/$W_{18}O_{49}$ [73]; 20% CuMOF/CdS [55]; ZnO/CdS/MoS_2 [103]; NiCoP-g-C_3N_4/CdS [66]; In_2Se_3/CdS [104]; MnO_2@CdS [72]; 2 wt% PT with CdS [58]; Hollow Octahedral Cu_2S/CdS [93]; 2D CdS/Nb_2CTX MXene NSs [105]; Co_3O_4 (3 wt%)/CdS/Ni [106]; CdS/CoP [107]; 0D/2D NiS/CdS [108]; CoP NPs/CdS/$NiWO_4$ [109]; CdS NRs/Ag_2S/NiS [110]; C–N–Co_3O_4/CdS [111]; H–CdS@NiCoP [112]; CdS/MoS_2/rGO [113]; PRGO/CdS-DETA [114]; CdS@UiO-66@MoS_2 [115]; NiS_x/CdS [116]; WO_{3-x}NRs/Zn0.3Cd0.7S NPs [117]; CdS@G@TiO_2 [118]; Hierarchical ZnO/CdS [68]).

3.3. Morphological properties CdS photocatalysts

The impact of different morphologies of cadmium sulfide (CdS) on its photocatalytic activity for water splitting under visible light has been a subject of intense research. CdS is a well-known photocatalyst that is widely studied for its ability to generate hydrogen via water splitting when exposed to solar light. The photocatalytic performance of CdS, however, can vary considerably depending on its morphological structure. This variation arises from the influence of morphology on factors

Table 2
Photocurrent reactions in the heterojunction based on CdS for the photocatalytic production of H_2.

Photocatalyst	Type of heterojunction	H2 evolution rate (mmol g-1 h-1)	Photocurrent response (μA/cm2)	References
Bi10/Ni6–CdS	Schottky	5.2944	18	[75]
CdS–Ni_3S_2/NF	–	100.50	205	[89]
CdS/NiO core-shell	p-n	243.9	29	[83]
CdS NRs/Ag2S/NiS	p-n	48.3	5.4	[110]
Hollow Octahedral Cu2S/CdS	p-n	4.76	16.9	[93]
2D CdS /Nb2CTX MXene NSs	–	5.040	10	[105]
CdS@Au into Ultrathin Ti3−xC2Ty	Schottky junction	5.371	260	[87]
Co3O4/CdS	p-n	7.131	5.6	[92]
CdS/CoP hollow nanocages	p-n	15.74	0.24	[107]
H–CdS@NiCoP core–shell nanosphere	p-n	13.47	4.2	[112]
NH2-MIL-125 (Ti)/CdS	Z- scheme	6.62	1.5	[101]
CdS/ZnS (CSZS–VZn)	Z-scheme	46.63	44	[94]
CdS/BiVO4	Z- scheme	197	4.7	[84]
W18O49/CdS	Z- scheme	55.24	25	[95]
CdS/W18O49	S-scheme	5.9	16	[73]
2 wt% PT with CdS	S-scheme	9.28	11	[58]
CdS/Mo2C–NiS	S-scheme	24.03	280	[54]
CQD/CdS	–	309	55	[82]
TiO2–Ni(OH)2/CNT/CdS	–	12	410	[71]
CdS/MoS2/rGO	CdS-Graphene	11.33165	135	[113]
PRGO/CdS-DETA	–	10.5	95	[114]
CdS@Zn–C	Schottky	6.6	12	[90]
20% CuMOF/CdS	S-scheme	0.3348	>16	[55]
NiCoP-g-C3N4/CdS	S-scheme	55.63	12	[66]
Hierarchical ZnO/CdS	Z	4.134	60	[68]
MnO2@CdS	S-scheme	3.94	2.5	[119]
Ni–Ni(OH)2/CdS	–	428	60	[74]
40-MC-CdS	Schottky	37.641	25	[77]
MoP/CdS composites	–	13.88	1.4	[78]
Fe2P–CdS	–	207.82	79.23	[79]
NiS/CDs/CdS (NCCS)	–	1.4445	220	[80]
MoP/CdS	–	163.2	75	[85]
CdS/CoOx/Co-metal	–	0.318	290	[120]
ltrathin CdS@BDC NSs	–	13.081	250	[88]
g-C3N4 NSs/CdS NPs	Type II	3.67	52	[91]
CdS NR/CoSx	Z- scheme	9.47	59	[96]
Pt–C3N4/CdS	Z- scheme	35.3	126	[97]
CdS/CeO2	Z- scheme	0.0701	2.1	[98]
CdS/W18O49/g-C3N4	Z- scheme	11.658	21	[121]
Co9S8/Cd/CdS	Z- scheme	5.2	4.8	[100]
g-C3N4/CdS	Z- scheme	1.80907	4.4	[102]
ZnO/CdS/MoS2	S-scheme	10.2474	13.5	[103]
In2Se3/CdS	S-scheme	1.632	103	[104]
Co3O4(3 wt %)/CdS/Ni	p-n	5.120	5.4	[106]
0D/2D NiS/CdS	p-n	18.1	4	[108]
CoP NPs/CdS/$NiWO_4$	p-n	47.7	5.7	[109]
C, N co-doped Co_3O_4/CdS	p-n	64.36	1.3	[111]
CdS@UiO-66@MoS2	–	0.786	70	[115]
NiSx/CdS	–	44.7286	12	[116]
WO3–x NRs/Zn0.3Cd0.7S	–	3.521	50	[122]
0D/2D CdS/MoO3−x	S-scheme	7.44	740	[123]
CdS@G@TiO_2	–	1.510	150	[124]

such as surface area, charge carrier dynamics, light absorption properties, and the interaction between CdS and dopants, which collectively affect the overall photocatalytic efficiency. The morphology of CdS plays a significant role in its photocatalytic activity for water splitting under visible light. Common CdS morphologies, such as nanoparticles, nanorods, nanosheets, nanoflowers, and hollow structures, exhibit distinct characteristics that influence photocatalytic behavior. CdS nanoparticles, for example, are widely studied due to their high surface area-to-volume ratio, which is favorable for photocatalytic reactions. However, their small size can lead to rapid recombination of photogenerated charge carriers (electrons and holes), thereby reducing photocatalytic efficiency. This issue can be mitigated through modifications such as doping or coupling with other materials. For instance, doping CdS nanoparticles with transition metals like platinum (Pt) has been shown to enhance the separation of charge carriers, improving hydrogen evolution under visible light [125].

CdS nanorods, with their high aspect ratio, offer an efficient pathway for charge carrier transport along the rod axis, which helps to reduce charge recombination. The increased surface area of nanorods provides more active sites for photocatalytic reactions. Furthermore, the anisotropic shape of nanorods improves light absorption compared to spherical nanoparticles, which is beneficial for visible light-driven photocatalysis. Doping CdS nanorods with metals such as copper (Cu) has been shown to enhance photocatalytic activity by facilitating charge separation [126]. Two-dimensional (2D) CdS morphologies, such as nanosheets and nanoflowers, provide a high surface area and abundant active sites for photocatalytic reactions. These 2D structures facilitate efficient electron-hole separation, which is critical for improving photocatalytic efficiency. Doping with elements like nickel (Ni) and cobalt (Co) has been demonstrated to enhance the photoactivity of CdS nanosheets by reducing charge recombination and promoting the transfer of electrons to reaction sites [127]. CdS nanoflowers, with their hierarchical structure, improve light absorption and provide multiple pathways for charge separation, which further boosts photocatalytic performance [128]. Hollow CdS nanostructures, such as hollow spheres, have garnered attention for their unique ability to serve as reservoirs for reactants or charge carriers. These structures typically exhibit high surface areas and enhanced light scattering properties, which can increase light absorption efficiency. Additionally, hollow structures can reduce the recombination rate of charge carriers by extending the diffusion length of the charges. The photocatalytic hydrogen evolution performance of hollow CdS structures has been significantly enhanced by doping with metals like silver (Ag) [128]. The photocatalytic performance of CdS can also be further optimized through metal doping. Metal doping improves the electronic properties of CdS, facilitates charge carrier separation, and alters the optical absorption properties, thereby enhancing its performance for water splitting under visible

light. The interplay between morphology and metal doping is crucial for achieving the highest photocatalytic efficiency.

Platinum (Pt) is one of the most widely used co-catalysts for enhancing the photocatalytic activity of CdS. Pt nanoparticles act as electron sinks, facilitating the reduction half-reaction and improving the overall hydrogen production rate. In the case of CdS nanoparticles, the incorporation of Pt has been shown to reduce charge recombination and enhance hydrogen production [129]. Copper (Cu) doping in CdS nanorods has been reported to promote charge separation by acting as a hole sink, preventing recombination and improving photocatalytic performance [126]. In CdS nanosheets and nanoflowers, doping with nickel (Ni) and cobalt (Co) has been shown to act as electron traps, improving charge transfer efficiency and enhancing hydrogen evolution rates [130]. Among the various CdS morphologies, nanorods and nanosheets have shown the most promising photocatalytic performance for visible-light-driven water splitting. Nanorods offer efficient charge carrier transport due to their anisotropic structure, and they are highly effective when doped with metals like Cu or Pt. Similarly, CdS nanosheets provide abundant active sites and efficient charge carrier separation, both of which are crucial for high photocatalytic efficiency. On the other hand, CdS nanoflowers and hollow structures present significant advantages, particularly in terms of light scattering and charge separation. However, they may suffer from lower stability and more complex synthesis procedures. CdS nanoparticles, although extensively studied, often exhibit lower photocatalytic activity due to the high recombination rates of charge carriers. This limitation can, however, be alleviated by doping or coupling with other materials.

The various morphologies as well as structures of CdS-based photocatalysts are depicted in Fig. 3. The usage of functioning sites and photocatalytic performance can be remarkably increased by heterojunctions of lesser dimensions [131]. The superior photocatalytic functions can be achieved through utilizing NPs in the fabrication of 0D/0D heterojunction. H_2 production performance and simultaneously increasing of NPs crystallinity could be increased through varying molar proportion of Cd^{2+} and S^{2-} [132]. Billah et al. [132] prepared the CdS nanocomposite with 5.5 wt% Pt and 1 mmol of histidine. The optimal 5.5 wt% Pt/CdS exhibited a remarkable H_2 evolution efficacy of 21.35 mmol g^{-1} h^{-1} yielding rate. This production rate was one of the highest rates ever reported. Wet chemical and hydrothermal methods were combined to fabricate Au@CdS nanocomposites by Lin et al. [133] at lower temperatures during the reaction. The optimized Au@CdS nanocomposites exhibited an excellent H_2 yields of 1.041 mmol g^{-1} h^{-1} rate, which was 175.3-folds larger as compared to CdS NPs in pure water

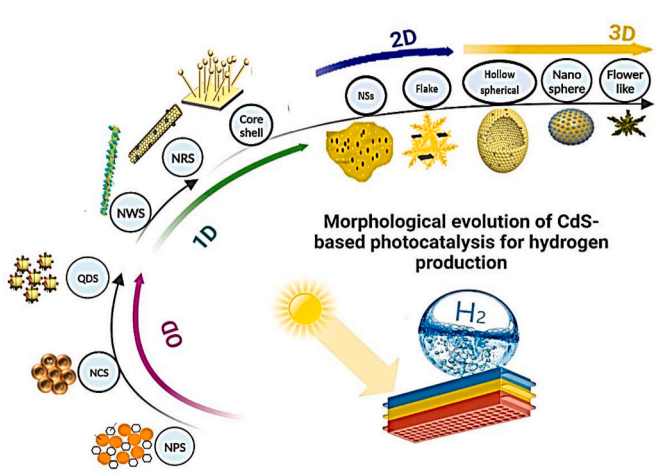

Fig. 3. Several morphologies and structures of CdS-based photocatalysts (NPs [141], NCs [142], QDs [134], NWs [135], NRs [136], Core-shell [137], NSs [138], Flake [139], Hollow spherical [140], Nano sphere [141], Flower-like [142]).

upon blue-LED light illumination. This activity benefited from the amplification of photo-induced charges-separation as well as the strong optical absorption ability by Au core. This considerable photocatalytic efficiency was larger than that of CdS NPs by a factor of 512.3. The Au@CdS nanocomposites exhibited an excellent long-term photo--stability. The decoration of Au NPs with CdS shell successfully achieved the highly conversion from photon to hydrogen energy. These reasons mainly benefitted from inclusion of Au NPs as well as the systematically combining of the reaction procedure. This inclusion of Au NPs enabled the synergy usage of photo-excited charges and promoted ability to absorb light in visible range by the effect of surface plasmon resonance. Xiang et al. [134] prepared the oil-soluble CdS QDs via solvothermal route. Subsequently, by employing mercaptopropionic acid at p^H 13, oil-soluble CdS QDs were transformed into water-soluble QDs through ligand swapping. The H_2 production performance was remarkably improved by water-soluble CdS QDs. The optimized sample exhibited H_2 production up to 1.61 mmol g^{-1} h^{-1} yielding rate. This efficiency was assigned to existence of Sn^{2+}, water-soluble CdS QDs and glycerol.

Effective transportation of electrons and stimulation by light are two distinctive benefits of 1D CdS. Li et al. [135] prepared the 1D CdS nanowires (NWs) with loading of NiS_2 NPs through a two step route. When lactic acid was employed as sacrefacial reagent, the optimized 40% NiS_2 loaded CdS NWs exhibited the enhanced H_2 production of 14.49 mmol g^{-1} h^{-1} yielding rate. CoP QDs anchored carbon skeleton was loaded as co-catalyst on CdS nanorods (NRs) by Sun et al. [136] to exhibit photocatalytic H_2 evolution. The as-prepared CoP/CdS photocatalyst showed outstanding H_2 production of 104.947 mmol g^{-1} h^{-1} yielding rate, which was 55.2-folds compared to pristine CdS. The obtained photocatalyst also demonstrated an extensively enhanced photo-durability. The highest AQY of 32.16 % was further obtained over the CoP/CdS composite. Upon illumination of light, metal nanostructures and its surrounding materials are interacted by Plasmon. Plasmon phenomena can be classified into two categories including localized surface plasmon resonance (LSPR) and surface plasmon polariton (SPP). Creation of excessive electric fields can be elucidated solely at nanoscale by the impact of plasmon. This impact has been disclosed with a novel insight to accomplishment of TiN in various fields, including electronic devices, photocatalysis, and solar energy harvesting. A wide range optical absorption range (500 nm–1200 nm) is provided by TiN. For conquering three predominant challenges of concerning CdS to generate H_2 simultaneously, Liu et al. [137] fabricated a core-shell structured CdS/TiN through coating of TiN layer with different thickness on CdS NWs. The optimized thickness (15 nm) of outer layer of TiN simultaneously provided outstanding protection, reduced probability of charge-carriers' recombination, and enhanced SPR effect. The optimal TiN/CdS core-shell NWs exhibited 3.62-fold enhancement in H_2 producing with 86.1 mmol g^{-1} h^{-1} yield rate in comparision to bare CdS NWs. This also displayed an outstanding QE of 62.4%. It exhibited superior reliability and chemical stability. This significant enhancement was due to plasmonic impacts of TiN layers. This effects lead to remarkable a significant dominance on optical absorption and superb H_2 evolution. A high conductive ohmic contract was built by TiN/CdS, which accelerated transportation of electrons to the surfaces.

The 2D semiconductors have garnered significant interest during photocatalysis owing to their plentiful reactive surface as well as outstanding contact charges-separation performance. The 2D ultrathin photocatalyst has a greater surface-to-volume ratio than their equivalents in other dimensions. These characteristics allow them to speed up the ability of charge-carriers separation and able to transport charge-carriers rapidly. Incorporating specialized coatalysts or boosters onto the surfaces of a feasible photocatalysts is frequently indispensable.By using CDs to reduce metal precursors in-situ, Qiu et al. [138] devised a straightforward and repeatable method to synthesis highly effective NSs CdS@CDs/Pt–SAs samples under solar-light. The optimal CdS@CDs/Pt–SAs with 1.15 wt%-loading of Pt significantly outperformed compared to pristine CdS and CdS/CDs/Pt-NPs during

production of H_2. It demonstrated a superior H_2 production efficiency of 45.5 mmol g^{-1} h^{-1} yielding rate. This rate was almost 133-folds more compared to CdS@CDs. 2D-2D Ni_2P/CdS NSs was constructed for H_2 production by Huang et al. [139]. The Ni_2P NSs were combined with snow-flake CdS. The optimum 5 wt% Ni_2P/CdS showed an outstanding H_2 production with 58.33 mmol g^{-1} h^{-1} by visible light illumination. The highest QE of 34.38% was further obtained under 420 nm. The formation of heterojunction between Ni_2P and CdS remarkably promoted charges-separation. Ni_2P provided a plentiful reactive sites for producing H_2.

In photocatalysis, the three-dimensional (3D) hollow structure exhibits a number of unique features. Hollow structured photocatalysts exhibit a higher photocatalytic efficiency because they provide an enlarged particular reactive surface. Moreover, enhanced photo-absorption capabilities are achieved through increasing the scattering of light inside the hollow structure. A faster charge transportation rate can be achieved by reducing the charge transportation length to the semiconductor surfaces by employing a thinner shell. The porous type hollow spherical Pd/CdS/NiS was constructed by Wang et al. [140]. The optimal 0.7% Pd/CdS/3% NiS photocatalyst exhibited a significant H_2 evolution efficiency of 3.8046 mmol g^{-1} h^{-1} yielding rate, which was higher compared to bare CdS by the factor of 33.4. An AQE of 0.24% was also obtained at 420 nm wavelength. This photocatalytic improvement was possible owing to load Pd and NiS as co-catalysts inside and outer surface of hollow structured CdS shell. The 3D S–Ta_2O_5/CdS nanosphere was prepared by Liu et al. [141]. The as-prepared S–Ta_2O_5/CdS sample exhibited a superior H_2 production efficiency of 54.51 mmol g^{-1} h^{-1} yielding rate upon irradiation in visible range, which was superior to CdS and Ta_2O_5. The S–Ta_2O_5/CdS nanosphere further showed high photo-durability. Zhang et al. [142] prepared the newly NiS/CdS NFs photocatalyst by modifying CdS nanaoflowers with β-NiS film via hydrothermal route. The NiS/CdS NFs presented an outstanding H_2 generation performance of 30.1 mmol g^{-1} h^{-1} yielding rate with AQE of almost 43% at 420 nm and high durability. This photocatalytic improvement was attributed to the boosted photo-excited electrons transportation capability and strong light absorption power of well-prepared NiS/CdS NFs nanocomposite.

The widespread application of CdS is restricted through its fast recombination of charges, intense photocorrosion, and inadequate surface area. To address these shortcomings, a lot of efforts has been conducted. Recently, a number of studies involving CdS QDs are being reported. Tiny dimensions of CdS QDs (2–10 nm), increased exposure of reactive sites, quantum confinement impact, minimal charge transit length, and unique interfacial impact make them as suitable photocatalysts for light responsive in visible range [143]. CdS QDs serve as a great alternative for photocatalytic H_2 generation due to their suitably negative flat-band potential. Nevertheless, the photocatalytic efficiency is reduced because facily CdS QDs aggregation produce bigger particles, which raises electron-hole recombination rate. Some strategies including integrating CdS QDs with different semiconductors have recently been proposed to overcome these shortcomings. The laborious process of developing CdS QDs is extremely complicated and challenging to handle. Aggregation of CdS QDs is still caused by the unfavorable anchoring capability of supporting materials. Developing a viable synthesis method and effective supplemental substances to fabricate CdS QD-based photocatalysts is particularly fascinating as well as difficult. A new class of conjugated polymer semiconductors termed covalent triazine-based frameworks (CTFs) have gained extensive application in photocatalysis. The CTFs with a substantial dispersion of metal-sulfide QDs provide an appropriate foundation for developing an effective photocatalyst via a one-pot route. For instance, Huang et al. [144] constructed CdS QD-loaded CTFs through a simple photo-reduction route. The optimal CdS QD/CTFs showed a significant H_2 evolution with 27.8 μmol h^{-1} yielding rate for 20 mg photocatalyst (equivalent to 1.39 mmol g^{-1} h^{-1} yielding rate), which was almost larger compared to bare CTFs and pristine CdS by the factors of 55 and 4, accordingly. The faster charge-separation capability caused by the synergistic interaction between CFTs and CdS QDs made this enhancement of photocatalytic efficiency.

The in-situ oil bath technique has been employed for decorating CdS QDs on P-doped hexagonal g-C_3N_4 tube (P-CNT) for developing a unique highly active CdS QDs/P-CNT photocatalyst [145]. An instance of 0D/1D heterojunction was produced by the homogenous implantation of the ultra-small CdS QDs onto the outer and interior surfaces of the hollow-structured P-CNT tube. The optimal CdS QDs/P-CNT-1 exhibited an excellent H_2 evolution of 1.579 mmol g^{-1} h^{-1} yielding rate utilizing visible light illumination. This rate of H_2 production was greater compared to P-CNT and CdS/CNT by the factors of 31.6 and 3.1, correspondingly. Enlarged surface, P doping, and the formation of 0D/1D heterojunction could boost optical absorption capability, reduce band gap, and encourage spatial separation of charges. These were the predominant causes of this enhanced photocatalytic performance. $CdCO_3$ nanoflakes/CdS QDs heterostructures for investigating its photocatalytic H_2 evolution activity were developed by Li et al. [146] via a hydrothermal route. The optimal $CdCO_3$/CdS QDs exhibited remarkable H_2 yields of 1.93 mmol g^{-1} h^{-1} upon visible light irradiation. A plentiful quantity of CdS QDs reactive sites generated by the cubic $CdCO_3$ was responsible for this improvement in photocatalytic performance.

The method of surface modification presents novel possibilities for developing novel kinds of QD-based photocatalysts. In addition to providing extremely active catalytic sites for H_2 evolution, the MoS_2 catalysts operate as a barrier for CdS to limit photocorrison. For instance, Zhuge et al. [147] devised a simple technique for MoS_2 photodeposition onto CdS QDs. The CdS QD surface was intimately decorated with thin-layered MoS_2 through the in-suit photodeposition technique. Close interaction encouraged charge separation in CdS/MoS_2 by facilitating the establishment of junctions between CdS and MoS_2. Exceptional photocatalytic performance was demonstrated by the resulting CdS/MoS_2 photocatalysts. The H_2 production rate reached to 13.129 mmol g^{-1} h^{-1} upon illumination in visible range. This rate of H_2 evolution was larger compared to pure CdS QDs by a factor of 7.2. Additionally, under visible light, the CdS/MoS_2 photocatalysts demonstrated better photocatalytic durability. One useful method for achieving successful energy conversion is the fabrication of QDs-linker-MOFs photocatalysts. Mao et al. [121] prepared the novel thiol-laced UiO-66 (UiO-66-$(SH)_2$)/CdS QDs to improve photocatalytic efficacy. The optimal UiOS-CdS presented highly H_2 generation efficiency of 15.32 mmol g^{-1} h^{-1} utilizing visible light. Under irradiation of light at 420 nm wavelength, this sample further showed an AQE of 11.9%. This improved performance was attributed to efficient charge carrier transportation bridge between CdS and UiO-66. Nevertheless, the strong photo-corrison limits applications of CdS QDs photocatalyst in photocatalysis.

Up to now, H_2 production efficiency of CdS/ZnO remains significantly lower than the acceptable limit of usage due to swift charges recombination in inner portions of bulk ZnO and bulk CdS. The photo-induced charge migration impedance decreased due to close interaction between the two semiconductors. The 0D-2D CdS QDs-ZnO NSs heterostructures was constructed by Ma et al. [148]. The optimal CdS/ZnO-12 showed a superior H_2 evolution efficiency with 22.12 mmol g^{-1} h^{-1} yielding with an excellent durability for 5-cycles. This rate was larger compared to pristine CdS ZnO by the factors of 13 and 138, respectively. Numerous favorable characteristics were identified as the cause of this increased photocatalytic performance, including development of Z-scheme, small dimensins of CdS QDs and ZnO NSs, and close interaction of ZnO NSs and CdS QDs. The potential for charges was efficiently mitigated by substantial impact of extremely small size. To alter the physicochemical characteristics of CdS QDs, element doping are being employed as a significant strategy. Shi et al. [149] constructed Se/CdS QDs by through a solvothermal route. The introduction of Se facilitated the creation of efficient trapping sites, enabling the accumulation of photo-induced electrons. This injection of Se resulted in an

upward shift of CdS's Fermi level position, significantly reducing charges recombination and extending life-time of charge-carriers. The enhanced charge-carrier density in CdS, made possible by the additional and substantially increased charge-carriers density from photo-induced electrons. The resulting $CdS_{0.9}Se_{0.1}$ QDs demonstrated an elevated H_2 production of 29.12 mmol g^{-1} h^{-1} upon illumination in 320–780 nm range. This H_2 yield rate was 23.5-folds higher than compared to bare CdS QDs. Furthermore, the $CdS_{0.9}Se_{0.1}$ QDs showed an AQE of 27.1% at 400 nm wavelength.

Considerable enhancement of electron interfacial transportation and acceleration of proton reduction are achieved by the co-catalysts Ru and Ru/NC, thereby reducing the recombination of photoinduced charges. For instance, Stavitskaya et al. [150] prepared Ru/CdS QDs to exhibit visible light driven efficient H_2 production activity. The optimized 15 wt % CdS QDs/0.2 wt% Ru exhibited excellent H_2 yields of 2.600 mmol g^{-1} h^{-1} with AQE of 15%. Recently, Xie et al. [151] prepared Ru/N-doped carbon (NC)/CdS QDs photocatalyst. The optimal 0.59 wt% Ru/NC/CdS-5 sample exhibited superb H_2 producgion efficiency of 73.6 mmol g^{-1} h^{-1} utilizing visible light irradiation, which was 21-folds larger to pristine CdS QDs. AQE of 3.6% was evaluated over Ru/NC/CdS-5 under irradiation at 420 nm. The Ru/NC/CdS-5 demonstrated excellent durability. Fig. 4 presents a comparison of the performances of several CdS QDs-based photocatalysts in H2 evolution. As depicted in Fig. 4, when covalent triazine-based frameworks (CTFs) [144], P-CNT [145], Sn^{2+} [134], $CdCO_3$ [146] were utilized as co-catalysts or additives with CdS QDs, the resulting CdS QDs-based photocatalysts exhibited a low-performance photocatalytic H2 evolution rate. Conversely, high-performance photocatalytic H_2 production rates were achieved over CdS QDs-based photocatalysts when MoS_2 [147], UiO-66-$(SH)_2$ (UIOS) [121], ZnO nanosheets (NSs) [148], Se [149], and Ru/NC [151]) were employed as co-catalysts/additives with CdS QDs.

3.4. Crystallinity of CdS heterostructure

The crystallinity of Cadmium Sulfide (CdS) has been recognized as a crucial factor influencing its photocatalytic performance, primarily due to its effects on the material's electronic properties, charge carrier dynamics, and surface characteristics. Higher crystallinity in CdS generally leads to improved charge carrier mobility, reduced recombination losses, and enhanced photocatalytic efficiency [152,153]. The influence of crystallinity on photocatalytic activity is attributed to several factors, including the availability of active sites, the structural stability under reaction conditions, and the optimization of electronic band structures. In materials with high crystallinity, the charge carriers generated upon light absorption can migrate more efficiently through the well-ordered crystal lattice. Crystalline CdS offers fewer defects and dislocations compared to its amorphous counterparts, which act as recombination centers for photogenerated electrons and holes. These recombination centers can significantly reduce the efficiency of photocatalytic processes by limiting the number of charge carriers available for redox reactions [154]. Additionally, the defects in poorly crystalline CdS materials serve as trap states that hinder the transfer of charge carriers to the surface, thereby reducing the material's overall photocatalytic activity [155,156]. Thus, crystalline CdS is expected to exhibit lower recombination rates, better electron-hole separation, and enhanced photocatalytic performance.

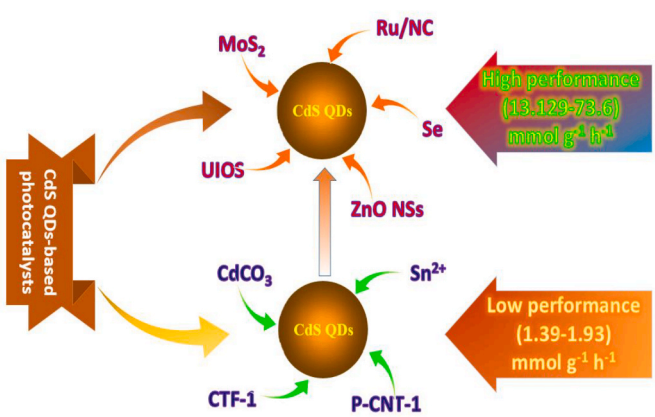

Fig. 4. Comparision of performances of CdS QDs-based photocatalysts in H_2 evolution (Low-performance CdS QDs-based photocatalysts: Covalent triazine-based frameworks (CTFs)/CdS QDs [144], Phosphorus-doped hexagonal g-C_3N_4 tube (P-CNT)/CdS QDs [145], W–CdS QDs with Sn^2/CdS QDs [134], $CdCO_3$/CdS QDs [146]; High-performance CdS QDs-based photocatalysts: MoS_2/CdS QDs [147], UiO-66-$(SH)_2$ (UIOS)/CdS QDs [121], ZnO NSs/CdS QDs [148], Se/CdS QDs [149], Ru/NC/CdS QDs [151]).

The surface properties of CdS are also critically influenced by its crystallinity. Crystalline CdS generally exhibits a more stable surface structure with fewer surface defects than amorphous CdS, which improves the material's ability to adsorb reactants and participate in photocatalytic reactions. Furthermore, the crystalline phase often provides more well-defined and active sites on the surface, which are essential for effective photocatalytic processes such as water splitting or pollutant degradation [157]. The higher surface area of crystalline materials, coupled with the ordered atomic arrangement, contributes to more efficient adsorption of reactants, a key factor in photocatalytic efficiency. Moreover, the optical properties of CdS, including its band gap and light absorption characteristics, are influenced by crystallinity. Crystalline CdS typically exhibits a more defined band gap compared to amorphous or poorly crystalline CdS, leading to better utilization of the visible light spectrum. The band gap in crystalline materials is more predictable and uniform, enhancing the material's ability to absorb light in the visible range, which is essential for photocatalytic processes driven by solar energy [158]. In contrast, the band gap of amorphous CdS is often broadened or distorted due to the lack of long-range order, limiting its photocatalytic activity under visible light.

The stability of CdS under photocatalytic reaction conditions is another important factor that is influenced by crystallinity. Crystalline CdS has been shown to exhibit better resistance to photocorrosion compared to amorphous CdS. The stability of the crystal lattice under photoreaction conditions prevents the material from breaking down or undergoing phase transitions, which is critical for long-term photocatalytic applications [159]. Amorphous materials, in contrast, are more prone to degradation due to their higher defect density and lower structural integrity. Several methods have been employed to improve the crystallinity of CdS, thereby enhancing its photocatalytic performance. Solvothermal and hydrothermal synthesis methods have been widely used to control the crystallinity of CdS. In these processes, Cd precursors are reacted with sulfur sources in a high-temperature solvent under controlled pressure. This process allows for the slow crystallization of CdS, which leads to larger and more uniform crystalline domains. By optimizing parameters such as temperature, pressure, and precursor concentration, the crystallinity of CdS can be significantly improved, leading to enhanced photocatalytic properties [160]. These methods have proven effective in obtaining CdS with well-defined crystal structures and improved surface characteristics, both of which contribute to better photocatalytic efficiency. Another strategy to improve crystallinity involves the use of template-assisted methods. Templates, such as mesoporous silica or carbon-based materials, have been employed to guide the growth of CdS nanocrystals. These templates provide a controlled environment for the nucleation and growth of CdS crystals, resulting in materials with higher crystallinity and more uniform sizes. After the crystallization process, the template is typically removed, leaving behind highly crystalline CdS with a controlled morphology [161].

This approach has been particularly useful for preparing CdS nanostructures with improved photocatalytic performance due to the

enhanced crystallinity and surface area. Post-synthesis thermal treatment, such as annealing in an inert or reducing atmosphere, has also been shown to improve the crystallinity of CdS. During thermal treatment, the disordered or amorphous regions of CdS undergo recrystallization, resulting in a more ordered lattice structure. The temperature and duration of the annealing process can be adjusted to optimize crystallinity and improve photocatalytic properties [162]. Thermal annealing has been particularly effective in enhancing the stability and photocatalytic activity of CdS under prolonged reaction conditions. Chemical vapor deposition (CVD) has been employed to grow high-quality CdS films with controlled crystallinity. In CVD, Cd and sulfur precursors are vaporized and allowed to react on a heated substrate, where CdS crystals form. The temperature and deposition rate are carefully controlled to promote the formation of large, well-aligned crystals with minimal defects. CVD-grown CdS films typically exhibit higher crystallinity and improved photocatalytic activity compared to those synthesized by other methods [163]. Additionally, the concentration of precursors used in the synthesis of CdS has been found to influence the crystallinity of the material. By optimizing the precursor concentration, the rate of nucleation and crystal growth can be controlled, leading to higher crystallinity. Lower precursor concentrations tend to favor the formation of larger, well-ordered crystals, while higher concentrations result in smaller, more uniform crystals. These changes in crystallinity can significantly impact the photocatalytic properties of the material, with optimized conditions leading to improved performance in photocatalytic applications [162].

The impact of crystallinity on the optoelectronic and photocatalytic properties of CdS materials has been extensively studied. Crystallinity was observed to significantly influence the energy bandgap, which plays a vital role in determining the efficacy of CdS as a semiconductor photocatalyst for hydrogen (H_2) production under solar irradiation [164, 165]. Efficient charge separation, essential for effective photocatalytic activity, required the development of CdS materials with appropriate crystallinity and band configurations [166]. Two primary crystalline phases of CdS, hexagonal (wurtzite, WZ) and cubic (zinc blende, ZB), were identified, each exhibiting distinct optoelectronic and photocatalytic characteristics. Hexagonal CdS was synthesized at higher temperatures, while cubic CdS was typically fabricated at lower temperatures [167]. The hexagonal phase demonstrated higher crystallinity, greater stability, and better durability under ambient conditions compared to the cubic phase. These attributes contributed to the superior photocatalytic H_2 evolution efficiency of hexagonal CdS [168].

The influence of crystallinity and phase on photocatalytic performance was systematically investigated. Bao et al. [169] demonstrated that monodisperse hexagonal CdS nanocrystals with high crystallinity outperformed cubic and mixed-phase CdS nanocrystals in H_2 evolution. The enhanced performance was attributed to optimized charge separation and reduced recombination. Lang et al. [50] further confirmed that CdS nanostructures with a higher proportion of the WZ phase achieved improved H_2 production rates. Using a solvothermal approach, nanocrystals with varying ZB and WZ phase ratios were synthesized, and the R-50 sample, with a majority WZ phase, achieved an H_2 production rate of 231.4 μmol h^{-1} for 50 mg of catalyst and a quantum efficiency (QE) of 28% at 420 nm. The enhanced performance was attributed to the synergistic effects of the multi-armed nanorod shape and high WZ-phase crystallinity. Despite the focus on hexagonal CdS, recent studies highlighted the potential of cubic CdS as a visible-light-driven photocatalyst. Yu et al. [170] synthesized cubic CdS nanocrystals (c-CdS-NC) using a precipitation approach in an S-rich Na_2S–Na_2SO_3 system. The optimized cubic CdS exhibited a higher H_2 production rate of 0.36 mmol h^{-1} for 50 mg of catalyst, surpassing traditional hexagonal CdS by a factor of 2.6. The superior performance was attributed to the nanocrystals' small size, enhanced surface area, and efficient charge carrier dynamics.

Qin et al. [165] prepared cubic and hexagonal CdS structures via a hydrothermal method and identified their respective crystal planes as (111) for cubic and (100) for hexagonal phases. The cubic CdS, characterized by a bandgap of 2.24 eV, exhibited a higher conduction band (CB) potential and lower electrochemical impedance than hexagonal CdS. These properties enabled the cubic phase to achieve a hydrogen yield rate of 680 μL in 180 min under visible light, exceeding the performance of the hexagonal phase. Advancements in the synthesis of highly crystalline CdS were also reported. Jin et al. [171] prepared single-crystalline hexagonal CdS nanowires using a solvothermal approach. The incorporation of 0.3 wt% Pt into the CdS nanowires resulted in a remarkable H_2 production rate of 1.49 mmol h^{-1} for 50 mg of photocatalyst, with a QE of 61.7%. Similarly, Nagakawa et al. [172] demonstrated that heat-treated ZB-phase CdS could be converted into highly crystalline WZ-phase CdS with reduced sulfur defects, resulting in a quantum yield of 19.2% at 420 nm. This activity was approximately 50 times greater than that of the ZB-phase precursor. These findings underscored the critical role of crystallinity in enhancing photocatalytic H_2 production. Both the phase and structural features of CdS materials were shown to influence their performance, and the development of highly crystalline, phase-controlled CdS materials remains an important focus for advancing photocatalytic technologies.

4. Classification of cadmium-sulfide (CdS)-based heterojunctions for hydrogen evolution

Photo-excited charge-carriers separation and transportation to destination reactive sites are indispensable in photo-catalysis. Recombination loses a larger portion of these couples [138]. The performance of CdS photocatalyst is diminished by charges recombination. A further predominant drawback is the limitations of the material's practical use for its photo-corrosion. To get efficient photocatalytic performance by preventing recombination, the pairs of electron-hole are required to be adequately separated. The photo-induced charges have to be rapidly transferred throughout the surface or interface. Generally, the photocatalytic performance is boosted by constructing heterojunction, leading to enhance H_2 generation. The technique of coupling CdS with a secondary substance is an efficient strategy for production of CdS-based heterojunctions, rather than a bare CdS photocatalyst [173]. This technique increases interfacial charges separation, prolongs visible-light absorbance, and extends area of surface. Each of these enhances photocatalytic efficiency for enhanced H_2 production. The quantum efficiency is further markedly improved by the crystalline structure of the CdS-based heterojunction photocatalyst. Additionally, the heterojunctions are found to display enhanced photo-stability and recyclability over bare CdS samples. To date, several CdS-based heterojunction photocatalysts for H_2 evolution were studied utilizing numerous co-catalysts including ions of metal, metal-oxides, metal-sulfide semiconductors, carbon substances, and so on. The mechanisms of charges transportation depends on heterojunction catagories. The CdS-based heterojunction photocatalysts are mainly classified into three categories, including: (1) CdS-metal heterojunction; (2) CdS-semiconductor heterojunction; and (3) CdS-carbon group heterojunction. The overall classification of CdS-based heterojunction is presented in Fig. 5. The design, principle and applications of the above-mentioned three categories of CdS based heterojunction photocatalysts are described in details below.

4.1. CdS-based Schottky heterojunction photocatalysts for H_2 evolution

In a Schottky heterojunction structure, the metal plays a crucial role in the photophysical processes, particularly in the context of light absorption and carrier separation. Metals, due to their unique electronic properties, can absorb incident light, leading to the excitation of electrons. When light interacts with the metal, electrons in the metal are excited from the Fermi level to higher energy states, creating electron-hole pairs. These photoexcited electrons and holes can subsequently be separated, especially when the metal is in contact with a semiconductor, forming a Schottky junction [174]. The metal's work

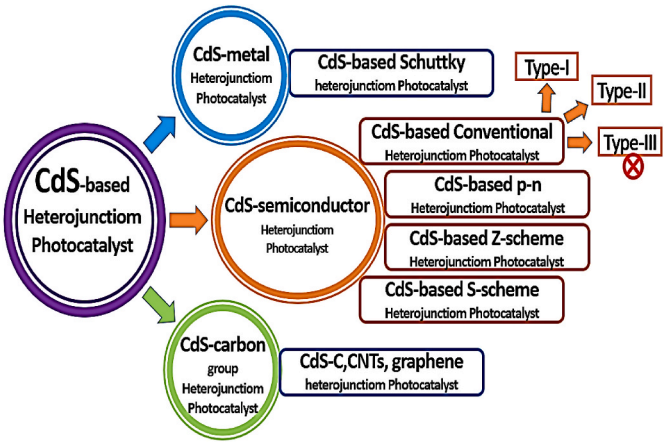

Fig. 5. Overall classifications of CdS-based heterojunction photocatalysts for H_2 evolution.

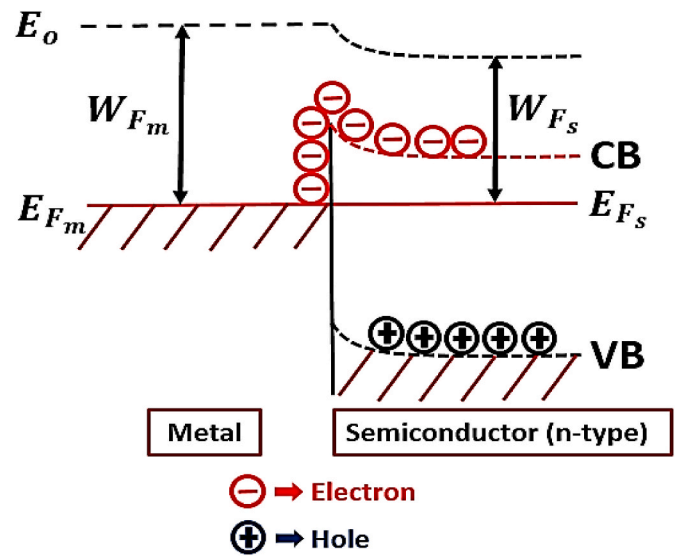

Fig. 6. Schematic of the Schottky barrier at Schottky heterojunction.

function and the properties of the semiconductor interface are critical factors in determining the efficiency of carrier separation. Although metals themselves do not typically exhibit significant light absorption in the visible range due to their high reflectivity and free electron density, they can still interact with electromagnetic waves, particularly in the ultraviolet or near-infrared regions. In many Schottky heterojunctions, the metal does not directly absorb light in the same manner as semiconductors, but its role in promoting carrier separation is often linked to its ability to create an electric field at the junction. This electric field can effectively separate the photogenerated charge carriers, preventing their recombination and enabling efficient charge transfer to external circuits [174].

The metal in such structures is not typically the primary material responsible for light absorption. Instead, it serves as a catalyst that enhances the efficiency of photocatalytic reactions. Metals, especially noble metals like platinum or gold, are known to act as co-catalysts in a variety of photocatalytic applications. They are believed to facilitate charge transfer processes by providing a pathway for the rapid movement of electrons, which can be critical for enhancing the overall photocatalytic performance [175]. By reducing the recombination of photogenerated carriers, metals can enhance the overall efficiency of photocatalytic processes, despite their limited role in direct light absorption. The Schottky barrier formed at the metal-semiconductor interface significantly influences the efficiency of carrier separation. The barrier height, determined by the metal's work function and the semiconductor's electron affinity, dictates how effectively the photogenerated electrons in the semiconductor can be injected into the metal. If the barrier is sufficiently low, electrons can move across the junction, while holes are left behind in the semiconductor, contributing to an efficient photocurrent generation [176]. This behavior is particularly useful in devices such as photodetectors, solar cells, and photocatalysts, where the separation and transport of charge carriers are key to performance. The distinction between E_F of semiconductor and metal is the factor that drives charge-carriers mobility across Schottky junctions. Separate fermi levels, E_{F_m} and E_{F_s} are located in the incoherent metal and n-type semiconductor, respectively. When the semiconductor of larger fermi state and metal of lesser fermi state are electrically attached, the electrons easily transfer to the metal of higher work-function (W_{F_m}) from the semiconductor CB of lower work-function (W_{F_s}), whilst their Fermi-levels are being aligned (Fig. 6). As a result, a significant negative charges accumulate onto surfaces of metals. Conversely, a great deal of positive charges accumulate into semiconductor owing to the migration of electrons away from the barrier's region. This procedure build a space-charge barrier at the contact of semiconductor and metal. An upward bend within energy band of semiconductor is displayed, thereby creating a Schottky barrier. This process also forms an intrinsic electric field towards metal from semiconductor. The following Eq. (8) provides barrier's height,

$$\varphi_b = W_{F_m} - X_s \tag{8}$$

Here, X_s indicates the electron affinity, which is determined from the semiconductor CB edge to the vacuum level. For photocatalysis, the Schottky barrier acts as an effective electron trap, providing an excessive partial electron density surrounding the co-catalysts, which stops unwanted electron migration from co-catalysts returning to the semiconductor [177]. This process largely inhibits recombination of charges and increases efficacy of spatial charges-separation.

The inclusion of precious metals onto CdS surface remarkably boosts its photocatalytic capability. The noble-metals deposition process which not only facilitates it easier to separate photo-excited charge-carriers but also lowers overpotential of reduction. Certain precious metals co-catalysts like Pd, Pt, Ru, Rh, Au, and Ag are utilized with CdS [178]. The improved CdS-based Schottky heterojunctions for H_2 evolution have been developed through incorporating a number of fascinating nanostructures. Palladium (Pd) has been considered as an advantageous cocatalyst owing to its higher availability and energy level which built it beneficial for producing H_2 [179]. Li et al. [180] found the dramatically enhanced photocatalytic H_2 evolution on the Pd-decorated CdS nanocatalyst. The optimal 3.83%Pd/CdS nanocatalyst achieved a highly AQE of 4.47% and 1.81% under illumination of light at 420 nm and 500 nm, respectively without scavenger. Further, in existence of scavenger, the 3.83%Pd/CdS nanocatalyst obtained a highly AQE of 1.81% and 27.49% under illumination of light at 420 nm and 500 nm correspondingly with considerable structural stability. The best H_2 generation rate on Pd-decorated CdS nanocatalyst was better than that of bare CdS by a factor of 110. The synergetic interaction between CdS and single Pd metal promoted the fast migration of electron from bulk-to-surface. Since Pd is more costly than other metals with low Pt content, researching approaches to boost the usage of Pd is still a crucial challenge.

The affordable approach to enhance H_2 productivity is the deposition of expensive noble metal NPs especially Pt NPs on CdS periphery. Dong et al. [181] reported the newly photo-reduction technique of Pt NPs depositing on CdS surface to significantly amplify photocatalytic performance for solar H_2 production. The optimized Pt–CdS with loading of 0.75 wt% Pt was constructed through photoreduction route, with existence of aprotective reagents. Pt NPs were properly distributed on CdS's surfaces by the help of NaI and PVP. The optimum 0.75 wt% Pt/CdS with 4:1 ratio of PVP and NaI presented a maximum H_2 yield of 1155.8 μmol

h^{-1} (for 5 mg samples equal to 231.16 mmol g^{-1} h^{-1}), corresponds to 1.8-folds compared to 0.75 wt% Pt–CdS under typical photo-reduction process and 17.3-folds compared to bare CdS. An excellent QE of 39.3% with a good stability was further observed over the obtained sample. The superior average H_2 evolution rate was achieved because of the charges transportation ability of Pt nanoparticles, the decreased dimension of Pt NPs on surfaces of CdS, and the expanded Pt–CdS surfaces. Pt nanoframes (NFs) have gained much interest for their enlarged exploitable surface and greater contact potential [182]. Coupling of Pt_3Pd NFs with CdS was employed to produce H_2. The Pt_3Pd NFs/CdS heterostructure was constructed by Gao et al. [183] through coupling CdS with Pt_3Pd nanoframes (NFs). The optimum photocatalyst presented an excellent production of H_2 up to 92.5 mmol g^{-1} h^{-1} yielding rate, with AQY of 65.9% under 420 nm wavelength. This outstanding performance of Pt_3Pd NFs/CdS was made possible by the amplification of separation and transportation efficiencies of charges because of co-catalyst's role as trapping centers for the electro-hole pairs.

The surface of CdS modifying by bi-metallic co-catalysts considerably promotes photo-activity. The Pt-based bi-metals including Pt–Ru, Pt–Mo and so on were significantly utilized in the oxidations of CH_3OH, CH_3CH_2OH, and $C_2H_6O_2$ [184]. Integration of additional metals to Pt, catalyst improves catalytic performance while simultaneously lowering Pt utilization. The evolution of H_2 in photocatalysis usually utilizes CdS NRs based multi-component photocatalysts. The Pt–Ru/CdS NRs was prepared through chemical-reduction following two steps [184]. The Pt–Ru/CdS exhibited an outstanding H_2 production of 18.35 mmol g^{-1} h^{-1} as a result of interaction of Pt and Ru. This production rate of H_2 was 2.9-folds larger compared to Ru–CdS. The inclusion of Pt and Ru NPs increased the lifetime of Pt–Ru NPs, facilitating separation of photo-excited charges. Adding Pt–Ru NPs on CdS NRs surfaces considerably increased the photo-activity. Doping of non-metals is also a potential approach for modulating electronic structures for developing effective photocatalysts. The usage of Mo increases the photocatalytic effectiveness of CdS. The H_2 production rate becomes greater when Pt is loaded onto Mo–CdS NRs surface and bare CdS NRs surface. The Pt–Mo–CdS displayed superb H_2 production of 35.23 mmol g^{-1} h^{-1} yielding rate. This production rate was almost 4.72-folds greater than that of CdS–Pt. This outperformed photo-activity of Mo–CdS indicated the excellent Mo-doping effect on CdS for increasing its performance in photocatalysis.

For prolonging photo-excited charge-carriers lifetime, the development of schottky heterojunction by modification of CdS with precious plasmonic metals [185] has demonstrated to be an effective strategy. Ag is more appealing than other noble metals due to its potent electrical and thermal conductivity, antimicrobial abilities, inexpensive price, and nontoxic. The 1D Ag NPs display the wide range of optical and photo-electrochemical features that are closely linked with their geometry-dependent plasmon surface resonances [186]. Reduced charges-recombination results from the Ag NWs in the photocatalysis acting as an expedited method for successfully transporting electrons. Xiong et al. [187] constructed the hierarchical1D Ag@CdS of core-shell structured NWs composed of CdS NSs/NPs on Ag NWs through wet-chemistry route. Due to their distinctive hybrid nano-architecture, the obtained hetero-NWs exhibited a significant H_2 yielding of 73.5 μmol h^{-1} (for 30 mg catalyst equivalent to 2.45 mmol g^{-1} h^{-1}) into water splitting process.

Effectiveness of cobalt-based oxides including CoO, Co_3O_4 as O_2 production cocatalysts on a variety of semiconductors has been thoroughly investigated. Kanan et al. [188] reported that Cobalt-phosphate (Co-Pi) exhibited an excellent O_2 evolution. Co-Pi takes part as hole accumulator for diminishing recombination of charges that have been stimulated by light. Di et al. [189] demonstrated superior H_2 evolution efficiency over Co-Pi/CdS NRs. Co-Pi-CdS NR was constructed through photo-deposition process. The ideal Co-Pi-CdS has an outstanding H_2 yields of 13.3 mmol g^{-1} h^{-1} upon illumination of visible light, which was superior compared to 1 wt% Pt/CdS. The optimal Co-Pi/CdS presented an AQE of 24.3% under 420 nm. The observed enhancement can be attributed to the Co-Pi co-catalyst's capability of trapping holes, efficient inhibition of photo-excited charges recombination and augmenting the electron density, leading to increased H_2 production.

Electric featured of MoS_2 are modified by inclusion of MoS_2 with transitional metals. Gopannagari et al. [190] constructed Fe–Co–MoS_2/CdS NRs through a facile process. The obtained Fe–Co–MoS_2/CdS nanocomposite presented the superior production activity. The maximum H_2 of 350 mmol g^{-1} h^{-1} was observed. This efficiency was 58-folds as compared to pristine CdS. This result was owing to the synergic relationship of MoS_2 with hetero-atom doped. This synergic effect facilitated separation sufficiency of photo-induced charges. This outstanding H_2 production rate also benefitted from the abundant edge sites, the improvement of charges transportation.

The morphologies of CdS-TMPS photocatalytic systems can obviously affect photocatalytic efficiency. Due to the benefits of having larger surfaces, active sites, and stronger heterojunction coupling with TMPS, 2D CdS NSs often display highly effective photocatalysis in contrast to 0D (or 1D) CdS. The catalytic efficacy of 2D CdS NSs depends on their thickness. Creating 2D-2D photocatalysts has emerged as a key strategy for achieving the best photocatalytic efficiency. Gai et al. [191] synthesized CoP–CdS heterojunction. An outstanding generation of H_2 was obtained 56.3 mmol g^{-1} h^{-1} over CoP–CdS by visible range illumination. This H_2 production rate was 11.3-folds more than puer CdS. This enhancement was benefitted from an excellent photocatalytic performance of CoP and the speed up charges separation and transportation. CoN NPs acts as a predator to trap photo-electrons. Chen et al. [192] constructed the CoN/CdS hollow nanosphere (CoN/CdS-HS) through in-situ adsorption deposition process by following nitrogenization treatment. The optimum CoN/CdS-HS photocatalyst with loaded 15% CoN featured an outstanding H_2 generation with 58.80 mmol g^{-1} h^{-1} with highly durability. This rate was 4.57-folds better as compared to bare CdS-HS upon illumination of light in visible range. This corresponds to an AQE of 23.53% was also observed under visible-light (405 nm). This increased activity was due to the strong optical absorption, the promoted charges-separation, the accelerated transportation of photo-induced charges, and the lowered interface resistance owing to the hollow spherical shape of CoN/CdS-HS photocatalyst.

Although, the noble metals including Pt on CdS could collect photo-excited electrons and function as reactive-sites for H_2 evolution. The exorbitant price and rarity of noble metals prevents their widespread use in the evolution of H_2 via splitting water. The cost-effective and efficient non-noble metals, sulphide and grapheme need to be soughted as alternatives. Ni is gaining popularity in photocatalytic processes for lower expensive. Ni is a fantastic ligand among a variety of transition metals. The H_2 production rate was significantly influenced by Ni NPs dimensions [193]. The optimization of Ni inclusion could accelerate separation of charges through generating shallower surface states for accumulating photo-induced electrons. Charges recombination, electro-chemical impedence, and band-gap of Ni–CdS are the vital factors for enhancing photocatalytic H_2 evolution efficiency. These factors are apparently lower to pure CdS. It also promotes optical absorption efficiency by reducing bandgap of CdS photocatalyst [194]. This further highlights the significance of Ni-composites including $Ni(OH)_2$, NiO and NiS, which are utilized as co-catalysts for H_2 production [195]. Employment of Ni-composites co-catalysts with CdS enhanced water splitting efficiency effectively when illuminated by visible light, providing excellent H_2 evolution rates. For instance, Ke et al. [196] prepared NiS-deposited CdS-DETA through a rapid and facile photochemical route. The maximum 230.6 μmol h^{-1} (7.49 mmol g^{-1} h^{-1}) H_2 yield rate was obtained on NiS/CdS-DETA photocatalyst, which was 8.42 and 1.72-folds better to bare CdS NPs and CdS-DETA. This improvement was because of the amplified charges-separation as a result of gwowing in situ of NiS NPs on CdS-DETA. Zheng et al. [197] fabricated the core-shell nanostructured Ni/(Au@CdS) photocatalyst via

the hydrothermal method following photodeposition. Ni/(Au@CdS) demonstrated remarkable H_2 generation of 3.882 mmol g^{-1} h^{-1} yielding rate. This also presented an AQE of 4.09% under 420 nm. This improvement of photocatalysis was due to synergy of plasmonics and co-catalyst.

Ni-doping and Ni NPs of controllable size were concurrently introduced on CdS NRs through employing a simple and adjustable ALD reduction process to enhance its photocatalytic efficiency [198]. The produced Ni NPs-Ni/CdS NRs showed 20.6 mmol g^{-1} h^{-1} rate of H_2 production. This H_2 production efficiency was larger compared to smaller size Ni NPs supported CdS NRs and bare CdS NRs by the factors of ~1.3 and 28.6, respectively. The outperformed AQE of 37.5% was also observed over this Ni NPs-Ni doped CdS NRs under 420 nm. The exceptional photocatalytic capability was because of a synergistic interaction between adding of Ni and evenly distributed. This synergistic effect facilitated charge-carriers separation. Nakibli et al. [199] successively studied the performance of Ni–CdSe@CdS NRs of numorous Ni NPs dimensions in photocatalysis. The combination of Schottky barrier and Electrostatic barrier charged energy connecting Ni and CdS could be the reason for the effect of Ni dimension on charge mobility. Chemical reduction was employed to develop the high-crystallization Ni NPs, and photo-reduction was employed for loading them onto the CdS surface [200]. The extended surface area of Ni–CdS was measured by BET procedure, which was larger compared to that of CdS NRs. The optimized 4%Ni–CdS sample presented outstanding H_2 production efficiency of 25.848 mmol g^{-1} h^{-1} yield rate, and QE of 26.8% with excellent stability even after 20 h at 420 nm in existence of $(NH_4)_2SO_3$ reagents. This enhancement was because of superior capability to absorb visible-light, the extended Ni/CdS surface area, and the photoinduced electron trapper feature of Ni owing to the introduction of Ni NPs.

Though nickel-cobalt bimetals sulfide is rarely reported by the photocatalysis, but it can still deliver a novel sight to design a photocatalyst. To further boost the photocatalytic HER efficiency, Ni–Co–S NPs with a 0D structure can increase particular surfaces, minimize the photo-generated electron transferring method and suppress photocorrosion to boost photo-stability [201]. Through a simple hydrothermal approach, Pan et al. [202] prepared the active-faceted Ni–Co bi-metals sulfide adapted CdS NRs. The hydrothermal approach was first used to construct the CdS NRs, after which Ni–Co–S NPs were deposited to their surfaces. The as-prepared Ni–Co–S/CdS presented a clearly H_2 evolution of almost 6.56 mmol g^{-1} h^{-1} yielding rate, which was almost 240-folds increased photocatalytic capability when compared to normal CdS. The functional facets prompted photo-excited electron aggregation at the surface to boost H_2 production process. Pt-like actions of Ni–Co–S encouraged photo-induced electrons to transfer/diffuse into water. CdS NRs and Ni–Co–S NPs' lower dimentions stipulated adequate H_2 production reactive-sites and decreased the transferring path, which was confirmed by electrochemical analyses. A stable PdNi alloy could be prepared utilizing Ni [203]. Compared to Pd, PdNi hollow structured catalysts greatly improved the electro-catalytic efficiency. It is infrequently employed as a co-catalyst on CdS. Ba et al. [76] used a solvo-thermal process to prepare 2D snowflake-shaped CdS. Using a galvanic substitution technique, Pd–Ni hollow alloys of various compositions were created and painted on CdS surfaces. The production of PdNi hollow NPs (HNPs) as well as PdNi HNPs decorated CdS (PdNi/CdS) were both shown by structural microscopic and spectroscopic investigation. The photocatalysis reaction for H_2 production was conducted while being exposed light of 420 nm wavelength. The maximum H_2 production with 54 mmol g^{-1} h^{-1} yield rate on Pd_1Ni_1/CdS was 1.7-folds greater to that of Pd/CdS and had a QE of 63.97% using light of 420 nm wavelength. The potent interaction of CdS and Pd_1Ni_1 HNPs, along with the development of the alloy's distinctive hollow structure and porous nature were increased quantities of functional sites for producing H_2. The interaction of Pd and Ni, and 2D CdS structure increased portability of photo-excited charges and reduced the rate of charges-recombination.

The establishment of a non-rectifying ohmic contact between TiN and CdS has been extensively studied as a fundamental aspect of CdS-metal heterojunctions. Ohmic junctions, unlike Schottky contacts, facilitate seamless charge transport without significant barrier formation, which is critical for photocatalytic and electronic applications. In the TiN/CdS system, the work function alignment between the metallic TiN and the CdS semiconductor was achieved, ensuring minimal energy barriers for electron transfer at the interface. This characteristic enabled efficient bidirectional current flow, a defining feature of non-rectifying ohmic contacts. The formation of the TiN/CdS heterojunction was typically achieved through deposition processes such as magnetron sputtering, pulsed laser deposition, or thermal evaporation. During the fabrication, TiN films were deposited as a conductive layer onto the CdS surface, ensuring uniform contact. The resulting ohmic junction exhibited low contact resistance, attributed to the favorable band alignment between the Fermi level of TiN and the conduction band of CdS. Such alignment minimized potential barriers and enhanced carrier injection efficiency [204,205]. Similar behavior was observed in other metal-semiconductor ohmic contacts, such as Ti/CdS and Au/CdS junctions, where low-resistance contacts were formed by careful control of deposition conditions and interfacial engineering [206]. In the Ti/CdS system, the Ti metal's work function closely matched the CdS conduction band, further enhancing electron transport. Similarly, Au/CdS ohmic contacts showed effective charge transfer due to interfacial modification with sulfur passivation, reducing defects and promoting bidirectional current flow.

The absence of rectification in the TiN/CdS junction was confirmed through current-voltage (I–V) measurements, which displayed linear characteristics over a wide voltage range. These measurements demonstrated that the TiN/CdS interface allowed for symmetrical electron flow, indicative of an ohmic behavior. Additionally, the interfacial properties were influenced by the surface states and defect levels in CdS, which were mitigated through annealing and surface passivation processes to improve contact quality [207]. In addition to TiN/CdS, heterojunctions such as Pt/CdS and MoS_2/CdS also demonstrated non-rectifying ohmic behavior. In the Pt/CdS system, the high conductivity of Pt enhanced electron transport across the interface, improving photocatalytic performance in hydrogen evolution [208]. Similarly, the MoS_2/CdS ohmic contact benefited from strong interfacial bonding and synergistic effects between the semiconductor and transition metal dichalcogenides, enabling efficient electron injection and separation of photo-generated carriers [209].

The non-rectifying nature of the TiN/CdS ohmic contact played a pivotal role in enhancing photocatalytic hydrogen evolution. The improved charge transport across the interface reduced recombination losses and promoted effective separation of photo-generated carriers. This enhancement was particularly beneficial in photocatalytic systems where rapid charge transfer is critical for sustaining redox reactions at the catalyst surface [210]. Moreover, the thermal and chemical stability of TiN ensured the durability of the junction under operational conditions, further establishing TiN/CdS heterojunctions as a promising architecture for advanced photocatalytic and optoelectronic applications. These findings paralleled observations in Ag/CdS ohmic contacts, where the Ag layer provided robust interfacial conductivity and oxidation resistance, enhancing long-term operational stability [211]. Future efforts should focus on optimizing deposition conditions, interfacial engineering, and exploring alternative metal-semiconductor combinations to further improve the performance and reliability of such ohmic contacts.

To date, among various non-noble metal co-catalysts, a number of practical substitutes for Pt-based co-catalysts have been shown to be transition metal phosphides (TMPs), which have undergone extensive research. Ni_2P is a suitable alternative to Pt noble metal. Ni and P sites positioned on the surface of Ni_2P (001) displaying a combined effect, which allowed proton-accepting and hydride-accepting sites to simultaneously speed up the process of H_2 production. Ni_2P acted as an

effective co-catalyst for recovering electrons from semiconductor with a lesser H^+ reduction overpotential for producing of H_2. Investigations and development have been conducted on several CdS–Ni_2P hybrids. For instance, Cai et al. [212] prepared the Ni_2P/CdS NRs photocatalyst by anchoring the surface of CdS NRs with Ni_2P NPs through solvo-thermal process. The resulting 2 wt% Ni_2P/CdS NRs showed H_2 production with 2.602 mmol g^{-1} h^{-1} rate. This rate was 20-folds more than pristine CdS NRs. The as-synthesized photocatalyst exhibited a highly stability, which was better as compared to Pt/CdS NRs. The significant efficiency was benefitted from effectively faster charges-separation and migration because of the constructed core-shell structured Schottky heterojunction contact. The 2D/2D Ni_2P/CdS NSs was constructed for H_2 production by Huang et al. [139]. The Ni_2P NSs were combined with snow-flake CdS. The optimum 5 wt% Ni_2P/CdS showed superb H_2 production with 58.33 mmol g^{-1} h^{-1} yielding rate along with QE of 34.38% under 420 nm. Ni_2P/CdS heterojunction construction remarkably promoted charges-separation. Ni_2P provided a plentiful reactive-sites for producing H_2.

Ni_3S_2 NS arrays anchored on nickel-foam (NF) were constructed by Feng et al. [213]. The obtained sample exhibited an effective and superb stable electro-catalytic performance for H_2 production. Ni_3S_2 is regarded as an exciting substance for usage in photocatalysis considering the outstanding qualities of the Ni_3S_2/NF. By combining the CdS and Ni_3S_2 NSs anchored on Ni foam (NF), Chao et al. [89] developed the film-like CdS–Ni_3S_2/NF for the initial time with multiple interfaces or junctions. With an exceptional H_2 production reaching 100.50 mmol g^{-1} h^{-1}, the resulting photocatalyst performed 6.8-folds better than 2 wt% Pt/NF–CdS. Abundant surfaces or interjunctions between CdS and Ni_3S_2 NSs and the remarkable kinetics of Ni_3S_2 NSs to convert to H_2 from water contributed to this remarkable photocatalytic efficiency. Solvo-thermal process was used to combine CdS and Ni_2P in the majority of experimental research. Ma et al. [214] prepared the Ni_2P/CdS/Ni photocatalyst by loading of Ni_2P on the Ni–CdS nanospheres. The optimized Ni_2P/CdS/Ni-3 with 3.7% Ni_2P loading exhibited superb photocatalytic H_2 production with 176.6 mmol g^{-1} h^{-1} yielding rate upon visible light irradiation, which was 63-folds of the pristine CdS. This rate is the largest H_2 production rate according to Fig. 7. This outstanding performance of the sample benefitted from the promoted charges-separation and the improved transportation of photoinduced charges, and efficient suppression of charges-recombination because of loading of Ni_2P. The bandgap was shortened as a result of the doping of Ni cations in the CdS lattice. Fig. 7 presents the performances of multi-structures Ni-based CdS heterojunction photocatalysts. The H_2 evolution performances of CdS-based schootky heterojunction photo-catalysts are shown in Table 3.

4.2. CdS-semiconductor heterojunction photocatalysts for H_2 evolution

A hybrid photocatalytic system made of two distinct semiconductors with uneven band structures is the semiconductor-semiconductor heterojunction [173]. Coupling semiconductors have been created as an effective design to produce heterojunctions with the improved contact charge separation and transportation, the longer visible-light absorbing capacity, and the enlarged photocatalyst surface area [220]. The photocatalytic quantum efficiency was also greatly improved by the heterojunction crystal structure. The CdS-semiconductor heterojunction photocatalysts can be mainly classified into four catagories (Fig. 8), e.g., i) CdS-based conventional heterojunction photocatalyst; ii) CdS-based p-n heterojunction photocatalyst; and iii) CdS-based Z-scheme heterojunction photocatalyst; iv) CdS-based S-scheme heterojunction photocatalyst, which are discussed below:

4.2.1. CdS-based convensional heterojunction photocatalyst

The CdS-based conventional heterojunction is a hybrid photocatalytic system containing CdS and other semiconductors of uneven band structures, leading to band alignments. Conventional heterojunction photocatalysts can be categorized according to their band alignment in three ways: type-I, II, and III. In type-I heterojunction, VB and CB levels of narrower bandgap are enclosed in those of the larger bandgap. According to Fig. 8a, semiconductor-I (SC–I) has a greater CB than semiconductor-II (SC-II), although Semiconductor-II has a lower VB [221]. When a light source is illuminated, semiconductor-II accumulates holes and electrons at VB and CB, correspondingly. These accrued electrons at semiconductor-II CB transmit to it surface and conduct reduction process. For instance, Ma et al. [224] observed the greatly enhanced H_2 yielding of 1.75 mmol g^{-1} h^{-1} over type-I CdS/MoS_2 core-shell.

Transition metal-based dichalcogenides have been studied as outstanding performance photocatalysts by Sumesh et al. [225] because of 2D architecture and distinct photo-electrons features. Advancement of photocatalytic H_2 production urgently needs inexpensive catalysts as well as earth-abundant. MoS_2 has the potential cheap, efficient and

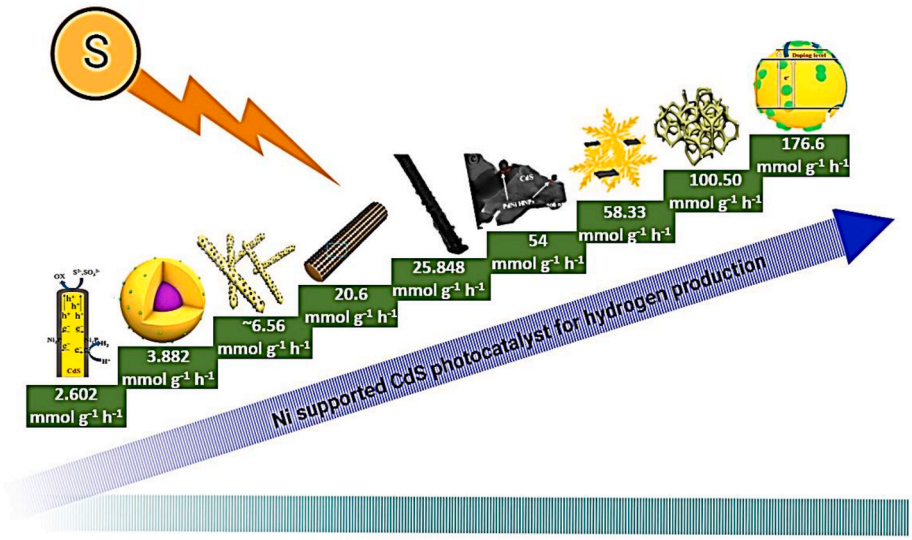

Fig. 7. Performances of multi-structures Ni-based CdS-based schootky heterojunction photocatalysts for photocatalytic H_2 evolution (Ni_2P/CdS NRs [212], core-shell nanostructured Ni/(Au@CdS) [197], Ni–Co–S/CdS NRs [202], Ni NPs-Ni doped CdS NRs [198], 4%Ni–CdS NRs [200], snowflake-shaped Pd_1Ni_1/CdS [76], snowflake-shaped 2D/2D Ni_2P/CdS [139], film-like CdS–Ni_3S_2/NF [89], 3.7% Ni_2P@CdS–Ni-3 nanosphere [214]).

Table 3
Performances of CdS-based schootky heterojunction photo-catalysts for H_2 evolution from water splitting.

Catalysts	Co-catalysts	Morphology	Synthetic methods	H2 evolution rate (mmol g^{-1} h^{-1})	Reference
Pt/CdS-histidine	Pt; histidine	0D	–	21.35	[141]
Au@CdS	Au	0D	wet chemical and hydrothermal	1.041	[142]
CdS/TiN	TiN	1D	–	86.1	[137]
Pt/CdS	Pt with PVP & NaI	0D	modified photoreduction	231.16	[181]
Pt3Pd NFs/CdS	Pt3Pd NFs	0D	–	92.5	[183]
Pt–Ru/CdS	Pt; Ru	1D	two-step chemical reduction	18.35	[184]
Ag@CdS core-shell HNWs	Ag	1D	wet-chemistry route	2.45	[192]
Co-Pi/CdS	Co; Pi	1D	photo-deposition	13.3	[189]
Fe–Co–MoS_2/CdS	Fe; Co; MoS_2	1D	Heteroatom deposition	350	[190]
Ni/(Au@CdS)	Ni; Au	1D	hydrothermal	3.882	[197]
Ni NPs/Ni doped CdS		1D	ALD-reduction	20.6	[198]
Ni/CdS	Ni	1D	chemical reduction	25.848	[200]
CdS/Ni–Co–S	Ni; Co; S	1D	hydrothermal	~6.56	[202]
Bi/Ni–CdS	Bi; Ni	0D	one-pot process	5.2944	[75]
Ni2P/CdS NRs	Ni2P	1D	in-situ solvothermal	2.602	[212]
NiS/CdS	NiS	0D	chemical precipitation	7.49	[215]
Pt/CdS	Pt	1D	–	4.87	[216]
Mo-doped CdS	Mo	1D	one-pot solvothermal	14.62	[217]
Mo–CdS/Pt	Mo; Pt	1D	–	35.23	[217]
5d1Ni1/CdS	Pd1; Ni1	2D	solvothermal; galvanic replacement	54	[76]
CdS–CoP	CoP	2D	hydrothermal	56.3	[191]
CdS@CDs/Pt–SAs	CDs; Pt; SAs	2D	–	45.5	[138]
Ni2P/CdS	Ni2P	2D	–	58.33	[139]
CoN/CdS-HS	Co; N	3D	CoN/CdS-HS	58.80	[192]
Ni_xCd_yS	Ni_x	3D	–	8.45	[198]
CdS–Ni_3S_2/NF	Ni_3S_2	2D	–	100.50	[89]
Ni2P@CdS–Ni-3	Ni2P; Ni	3D	two-step thermal treatment growth; chemical reduction	176.6	[214]
Pt–C@CdS-HS	Pt; C	3D	hydrotherma	20.9	[218]
Co@NC/CdS	Co; N; C	3D	–	8.2	[219]

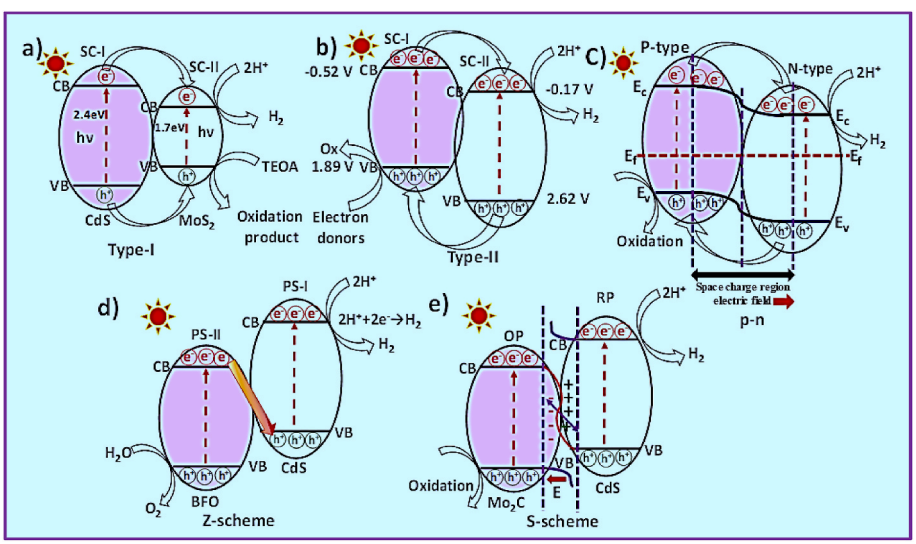

Fig. 8. The band alignment and the separation of electron-hole pairs in the CdS-semiconductor heterojunction photocatalysts: a-b) CdS-based conventional heterojunction photocatalysts; c) CdS-based p-n heterojunction photocatalyst; d) CdS-based direct Z-scheme heterojunction photocatalysts; e) CdS-based S-scheme heterojunction photocatalyst (type-I [221]; type-II [222]; direct Z-scheme [223]; and S-scheme [54]).

stable co-catalyst for substituting precious metal Pt as co-catalyst. MoS_2 has three atomic layers and an S–Mo–S structure. MoS_2 is considered to be a viable photocatalyst for photocatalytic H_2 production. A common field of study is adding MoS2 as a co-catalyst with CdS. Compared to CdS, lower CB of MoS_2 built it simply to travel photo-excited electrons to MoS_2 NSs. When exposed to light in visible range, majority of photo-induced charges recombined in clean CdS, only a tiny portion took part in the photocatalysis, leading to a slower rate of H_2 production. Electrons produced in CdS migrate to MoS_2 after the construction of MoS_2/CdS heterojunctions and thereafter absorb by H^+ to form H_2, because of compatible energy band potentials. Additionally, the intimate contact between MoS_2 and CdS develop through one-step approach can successfully facilitate the transport of electrons. Charge recombination is significantly decreased. The photocatalytic production of H_2 is greatly increased by forming of a heterojunction between CdS and MoS_2 NSs. The researchers have developed heterostructures employing a variety of structures, including MoS_2/CdS nanospheres [224], MoS_2/CdS core-shell [226], and MoS_2/CdS microboxes [227]. Fig. 9 compares the rate of photocatalytic H_2 production using different MoS_2/CdS type-I photocatalyst complexes.

In order to allow for the possibility of electron transport, MoS_2 was loaded on CdS surface. CdS NW and MoS_2 were generally joined together forming type-I heterostructure because of structural properties of the materials. In a two-step method, Zhao et al. [221] evenly distributed

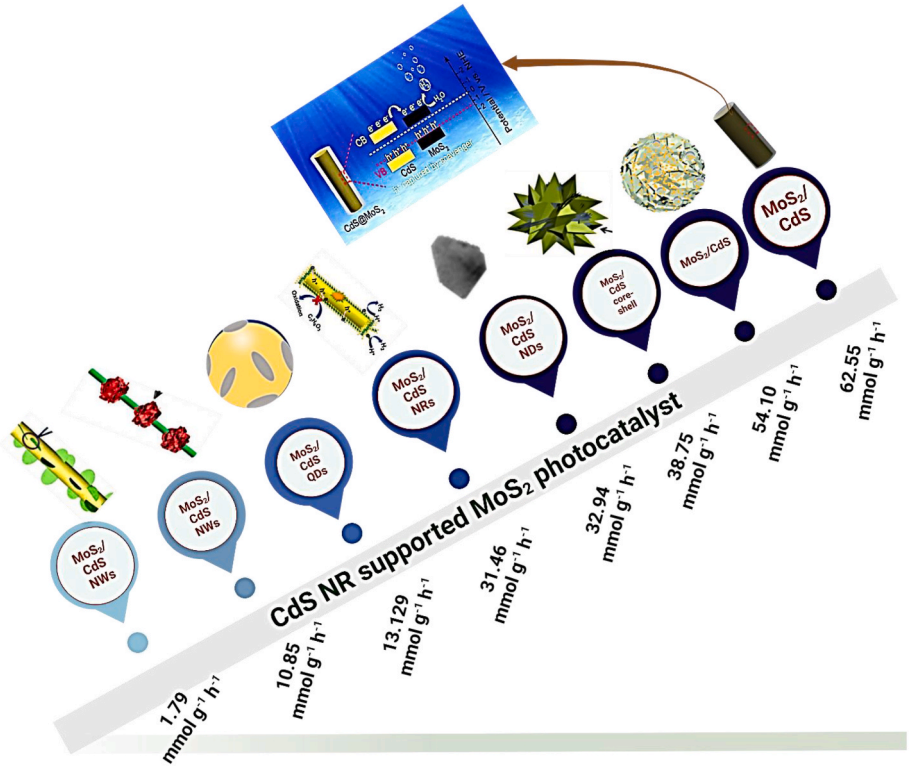

Fig. 9. The comparison of photocatalytic H_2 production rate over the different type of structures of MoS_2/CdS type-I photocatalysts and the schematic illustration of the mechanism of photocatalytic H_2 generation for the CdS@MoS_2 nanoheterostructures using potentials of water reduction and oxidation as a comparison (MoS_2/CdS NWs [221], MoS_2/CdS NWs [229], MoS_2/CdS QDs [230], MoS_2/CdS NRs [231], MoS_2/CdS NDs [225a], MoS_2/CdS core-shell [226], MoS_2/CdS [232], MoS_2/CdS [233]).

MoS_2 NSs over CdS NWs surface for constructing CdS/MoS_2 (CM) composites. The MoS_2/CdS NWs having a molar proportion of 1:0.3 (CM-0.3) produced H_2 with 1.79 mmol g^{-1} h^{-1} yielding rate. This was 35.8-folds more rapid than the rate of naked CdS NWs. This significant production of H_2 was attributed to strong optical absorbtion efficiency of MoS_2. Separation of charges was aided by the creation of heterojunction between CdS and MoS_2, which also prevented CdS photo-etching. Sparing and uniformly distribution of MoS_2 helped prevent the shadowing effect of CdS when light was directly exposed to it. As Fig. 9, this H_2 production rate over MoS_2/CdS NWs was the lowest rate among the other MoS_2/CdS photocatalysts. Excessive MoS_2 NSs impeded the capability of CM composite ability to produce H_2 and restricted the light adsorption of CdS. A straightforward hydrothermal process was used by Zhang et al. [228] for developing willow-branch structured MoS_2/CdS heterojunctions. Under illumination of visible range, with 250.8 μmol h^{-1} yielding rate for 80 mg photocatalyst (=3.135 mmol g^{-1} h^{-1} yielding rate), the optimized 5 wt% MoS_2/CdS (MC-5) demonstrated an increased photocatalytic H_2 evolution that was about 28-folds faster than that of pure CdS. The resulting MC-5 sample also exhibited a considerable AQE 3.66% at 420 nm. This photocatalytic efficiency of MC-5 was responsible for forming of type-I MoS_2/CdS heterojunction. Such type of heterojunction led to promote optical absorption ability in visible range, accelerate charges-separation and transportation, and suppress charge recombination. The directional transportation of electrons capabilities of 1D CdS NWs is outstanding. The 1D multinode MoS_2/CdS hetero-NWs were constructed by Lin et al. [229], and they produced H_2 with 10.85 mmol g^{-1} h^{-1} yielding rate. But during synthesis techniques, sulfur source was predominantly Thiourea [234] and thioacetamide [235] were predominantly utilized in fabrication process. Its reaction was speedy. Thus, for controlling its growth rate, PVP and glucose were employed as reagents [236]. 2D/2D type-I MoS_2/CdS heterojunction was febricated by Xiong et al. [237]. During visible light illumination, the 2D/2D 7 wt% MoS_2/CdS sample demonstrated highly H_2 production of 18.43 mmol g^{-1} h^{-1} within lactic acid, which was 6-folds greater to that of pristine 2D CdS sample. Charges separation and transportation were much enhanced. Further charges recombination was significantly reduced in MoS_2/CdS heterojunction.

An effective and simple approach has to be further developed. Primarily, combinations of MoS_2 and CdS are primarily centered on hydrothermal route. Fu et al. [225a] constructed the type-I MoS_2/CdS nanocomposites by decorating MoS_2 NSs on CdS nanodiamond surface via hydrothermal route. The optimum 6 wt% MoS_2/CdS demonstrated an enhanced H_2 generation of 32.94 mmol g^{-1} h^{-1} yielding rate. When compared to naked CdS nanodiamonds, this was three times larger. The ideal optical adsorption spectrum, the low rate of charges-recombination, the additional charges creation, outstanding charges transmission efficiency, and higher donor concentration were all credited with the improved photocatalytic effectiveness. Zhang et al. [238] developed the new MoS_2/CdS nanoheterojunction through a simple hydrothermal route, which showed an excellent H_2 production efficiency. The H_2 production rate on 15%MoS_2/CdS reached to 35.24 mmol g^{-1} h^{-1} and significant photo-durability for 4-cycles, which was 85.95-foldes better compared to CdS. The formation of type I heterojunction was credited with this superior improved photocatalytic efficiency. The active site of MoS_2 exists at the edge, but the basal plane is inactive in catalysis [239].

Production of MoS_2/CdS nanostructures with intriguing morphologies has experienced exciting advancements. The majority of the documented synthesis processes involve two or more challenging steps, which hinders the manufacture of photocatalysts on a broad scale. A very desirable objective is to create a straightforward, mild, and affordable method for creating MoS_2/CdS nanostructures with distinctive morphologies. MoS_2/CdS heterostructures have been fabricated by employing numerous techniques. Multi-step preparation, time

expending and lower production efficiency are the shortcomings of these techniques. The creation of a quick and efficient synthesis method for MoS_2/CdS is very important. Hydrothermal process are considered as a promising synthetic process for facile operation and cost-effective [240]. Wu et al. [226] utilized PVP, CH_4N_2S, $H_{24}Mo_7N_6O_{24}{\cdot}4H_2O$, and $C_4H_6O_4Cd{\cdot}2H_2O$ via hydrothermal process for constructing MoS_2/CdS. An outstanding H_2 evolution of 775 μmol h^{-1} yielding rate for 20 mg photocatalyst (equivalent to 38.750 mmol g^{-1} h^{-1} yielding rate) was obtained over MoS_2/CdS heterostructure. By wrapping an overlayer that performs energy conversion catalytic, safeguarding, core-shell structure could provide a photocatalyst enhanced performance and durability [241]. Through a straightforward hydrothermal process, Yin et al. [233] constructed CdS@MoS_2 core-shell nanostructures. The optimum CdS@MoS_2 heterostructures exhibited an outstanding H_2 production of 62.55 mmol g^{-1} h^{-1} yielding rate. This was 148-folds better to bare CdS sample. As Fig. 9, this H_2 production rate over MoS_2/CdS NWs was the highest rate among the other MoS_2/CdS photocatalysts. The construction of 2D/2D heterojunction photocatalysts has drawn increased interest because of its inherent advantages, including their extended contact interfaces, low charge-migration path, and abundance reactive sites, all of which are advantageous for improvement of photocatalytic efficacy.

Owing to their distinct physicochemical features, 2D transitional metal phosphorous chalcogenides (MPC_x) have gained attention in catalysis [242]. Wang et al. [243] reported that 2D $NiPS_3$ nanosheets under xenon light irradiation produced H_2 with 26.4 and 74.67 mmol g^{-1} h^{-1} yield rate into water and Na_2S/Na_2SO_3 aqueous solution, respectively. On numerous semiconductor photocatalysts, the use of the MPC_x family is a generic platform for significantly improving photon-excited H_2-production performance. The $NiPS_3$/CdS type-I heterojunction photocatalyst demonstrated 13.6 mmol g^{-1} h^{-1} H_2 yielding efficiency utilizing visible-light, which was 16.67-folds higher compared to bare CdS sample [244]. This improvement benefited from $NiPS_3$/CdS type-I heterojunction's highly correlated interface, faster separation and transportation of charges, quantity of atomic P/S facilities, and functional base S locations on $NiPS_3$ extremely thin NSs. In type-I heterojunction photocatalyst, effective separation of electron-hole are inhibited by accumulating both holes and electrons on same semiconductor. Consequently, redox process occurring on semiconductor having reduced redox potential value greatly reduces redox capacity. Further, in a type-I heterojunction, charges are pushed towards a narrower bandgap semiconductor, where they easily recombine.

Positions of VB and CB are distinguished between two semiconductors in type-II heterojunctions. This results in an accumulation of opposing charges at each site, preventing the charges from being recombined. As Fig. 8b, for type-II heterojunction, semiconductor-I (SC–I) possesses higher negative CB and less positive VB compared to semiconductor-II (SC-II). Photo-excited electrons and holes migrate to semiconductor-II and semiconductor-I, respectively, under the influence of light. Pairs of hole and electron become spatially separated [131]. Rapid mass transfer, a broad spectrum of optical absorbing capability, and excellent effective charges-separation are all characteristics of type-II photocatalysts [245]. Photocatalyst of type-II is the utmost effective conventional photocatalyst that improves photocatalytic efficacy amongst those mentioned heterojunctions. Several metal-oxides/metal-hydroxides such as ZnO, $Ni(OH)_2$, etc., have been successfully utilized as co-catalysts for enhancing H_2 production efficiency of CdS in photocatalysis due to their superior chemical and physical features, excellent photo-durability, significant oxidation productivity, and ecological friendliness. For instance, Qiu et al. [70], studied the impact of nature of surface-loaded nickel compounds on CdS in evolution of H_2. The CdS nanoflakes were embellished with $Ni(OH)_2$ NPs using a simple photo-deposition process. The optimaized Ni $(OH)_2$/CdS-3 photocatalyst produced H_2 with 20.14 mmol g^{-1} h^{-1} yielding rate and good photo-stability. The observed rate was almost 3-folds more compared to pristine CdS. An AQE of 8.7% at 420 nm and 2.4% at 500 nm were observed for the optimized sample. Sabstantial visible light absorption, enlarged particular area of surface, and triggered charges separation and transfer were benefited from type-II band-alignment. Zhang et al. [246] constructed CdS–$Ni(OH)_2$ photocatalyst of hexagonal pyramid architecture. The optimal CdS–$Ni(OH)_2$ sample delivered outstanding H_2 production with 29.51 mmol g^{-1} h^{-1} yielding rate. This rate was better than that of CdS–Pt and hexagonal pyramid CdS by factors of 1.9 and 5.6, respectively. This enhanced rate was because of forming type-II photocatalyst involving $Ni(OH)_2$ and CdS. Such a heterojunction provided enhanced effectively charge-separation. Owing to synergistic behavior of the bi-metals or tri-metals, the alloy co-catalyst can boost the photocatalytic function. For example, the amplification of photocatalytic performance of H_2 production by splitting of water was reported by Gao et al. [183] using the multi-heterostructured Pt NF–$Ni(OH)_2$–CdS whereas $(NH_4)_2SO_3$ acted as sacrifice was achieved. The obtained Pt NF–$Ni(OH)_2$–CdS exhibited an outstanding production of H_2 of 44.05 mmol g^{-1} h^{-1} yielding rate with QE of 58.89% (at 420 nm).

The type-II heterojunction involving ZnO and CdS is anticipated for showing close interaction and effective separation of charges because of its suitable lattice arrangement and appropriate band positioning. The type-II heterojunction CdS/ZnO core-shell nanofibers exhibited good photocatalytic activity for H_2 synthesis. A significant contact interface was present in CdS/ZnO core-shell structure, which further improve effectiveness of electron-hole pair separation. Consequently, compared to ZnO and CdS alone, ZnO/CdS displayed greater H_2 production rate in photocatalysis. An effective and durable photocatalyst requires careful consideration of its surface qualities, crystallinity, band structure, material selection, and geometry of a heterojunction photocatalyst. A feasible substance for the production of H_2 is CdS–ZnO core-shell NW. For instance, Tso et al. [247] constructed CdS–ZnO core-shell NWs. ZnO shells have the potential to both promote electron-hole separation and avoid photo-corrosion in CdS NWs. The as-prepared CdS–ZnO core-shell NWs exhibited an improved H_2 production performance of yielding rate of 9618 μmol g^{-1} at the 4-th hour with better stability in acid solution, which was 2-times greater compared to CdS NWs. More prolonged charge-carriers recombination duration along with proper band alignment were credited for the improved capability of H_2 production. H_2 generation efficiency was higher over CdS–ZnO with thinner ZnO layers, because of the reduced the possibility of change-carrier recombination and the amplified optical absorption ability. CdS–ZnO core-shell NWs with a ZnO layer that was 10 nm thick had the maximum efficiency. The type-II heterojunction involving ZnO and CdS is anticipated for showing close interaction and effective separation of charges because of its suitable lattice arrangement and appropriate band positioning. The photocatalytic capabilities could be effectively enhanced by ultra-small heterostructures. Guo et al. [248] constructed the ultra-small ZnO/CdS heterojunction through a two-step heteroepitaxial growth process. The development of core-shell heterostructures was significantly aided by anion exchange. In an existence of S^{2-} and SO_3^{2-}, the resultant ZnO/CdS demonstrated significant H_2 evolution of 6.696 mmol g^{-1} h^{-1} yielding rate and outstanding photo-stability for about 72 h. This enhanced activity of the as-prepared nanoscale photocatalyst was superior to bulk ZnO/CdS heterostructures. This improvement of photocatalytic activity and the excellent photo-stabilty was benefitted from the construction of the type-II band-alignment as well as its tiny shape. Such a type-II heterojunction played a vital role in promoting the effective charges-separation and reducing the charge-carriers' transfer length.

Owing to a discrepancy in the lattices of wurtzite ZnO and wurtzite CdS, ZnO shell adheres to CdS core as NPs instead of a overlay. The CdS@Al_2O_3@ZnO heterojunctions were prepared by Ma et al. [249] employing a straightforward ALD process through introducing extremely thin Al_2O_3 bridge interlayer into interface between CdS core and ZnO shell. A maximum H_2 evolution of 1190 mmol m^{-2} h^{-1} yielding rate was determined in optimal CdS@Al_2O_3@ZnO, which was 2.17-folds greater than that obtained for CdS@ZnO. An AQY of 31.14% was also

observed at 420 nm wavelength. In CdS/Al_2O_3/ZnO, photo-excited electrons were adequately diminished by H_2O in order to form H_2 after tunneling to ZnO shell from CdS core. Al_2O_3's fixed negative charges are effective at consuming the photogenerated holes. The wurtzite ZnO and wurtzite CdS lattice mismatch was successfully modified by Al_2O_3 interlayer. This facilitated it being easier for the ZnO layer to be deposited uniformly, which promoted close contact between interfaces and reduced charge carrier recombination. Charges separation and transportation benefited from dual functionalities of Al_2O_3 interlayer, which significantly boosted the photocatalytic H_2 production.

The sulfur clusters produced by photocorrosion have a deleterious impact on the CdS system's activity. For improved photocatalytic performance for producing H_2 using visible-light, small quantity of crystalline elementary -sulfur (-S) NPs were placed on CdS NRs surface. For example, Zhang et al. [250] febricated newly S/CdS heterostructure via simple solvent evaporation-deposition-precipitation route. Despite featuring a wider bandgap compared to CdS, lower surface loading amount of α-S maintained S/CdS's good optical-absorption capabilities in the visible region. The optimized 10% S/CdS photocatalyst exhibited much improved performance in photocatalysis. The corresponding H_2 production yield rate was 10.01 mmol g^{-1} h^{-1}. This rate was 5.92 and 1.99-folds compared to that of single CdS without and with K_2PtCl_6, respectively. The S/CdS compodite presented prolonged duration for photocatalytic stability more than 10 cycles. This highly improved performance was because of highly promoted separation of photo-induced charges through the tightly touched S/CdS type-II heterojunction interfacial contact between α-S NPs and CdS NRs. During photocatalysis of semiconductor heterostructure, the interfacial charge kinetics is essential. CdS–MoS_2 nano-composite was developed by Liu et al. [251] to study the interfacing charge kinetics for photocatalytic H_2 production by overlapping the hexagonal CdS on the exfoliated MoS_2 film through a typical chemical bath technique. The CdS–MoS_2 photocatalyst exhibited a surprising higher photo-current density together with an excellent production of H_2 with 2.3 mmol g^{-1} h^{-1} yielding rate. This improvement originated from the type-II interactions at the interface of CdS–MoS_2 forming an interfacing electric-field with faster charges-separation.

The photocatalytic abilities of CdS are impacted by its shape and crystal structure [83]. Zhang et al. [252] fabricated the 1D/2D CdS/ZnS heterojunctions by anchoring uniformly distributed ZnS on CdS NSs surface under atmosphere pressure and temperature. During visible light (>400 nm) illumination, the best CdS NSs/ZnS NPs-0.6 heterojunctions produced H_2 at a remarkable enhanced 14.02 mmol g^{-1} h^{-1} yielding rate, outperforming than pristine CdS NPs and CdS NSs by factors of almost 85 and 10, respectively. The obtained heterojunctions exhibited an excellent AQY of almost 2.76% at 400 nm with long-term superior photo-stability over 58 h. The development of type-II and Z-scheme was blamed for improvement of photocatalysis efficiency. Along with providing abundant exposed reactive sites, the subsequently formed 1D/2D heterojunctions provided a more rapid path to photoinduced charge-carrier production for incredibly effective separation and transport across the structure of single-crystalline CdS NSs. Several studies have centered to 1D CdS NRs. Multi-arm CdS NRs have drawn a bit of interest [253]. Large proportions and excellent crystal structure are two benefits of 1D CdS NRs that can be retained by multi-arm CdS nanorods, each of which has a unique geometric relation. This helps to successfully alleviate the accumulation issue with simpler ultrasonic dispersing. The core-shell structured CdS/ZnS NRs were febricated by Sun et al. [254] via decorating triarm CdS NRs with dodecylamine (DDA) and wrapping them in an interstitial ZnS shell using a straightforward chemical depositing procedure. The optimized CdS/ZnS with 1:0.5 M proportion (CZS-0.5) exhibited an outstanding H_2 yield of 242.0 mmol g^{-1} h^{-1} without co-catalysts, exceeding those of single CdS and ZnS by 4.2 and 38.4 folds, respectively. The obtained CZS-0.5 photocatalyst achieved the maximum AQE of 50.61% at 380 nm. The comparable type-II system produced in CdS/ZnS and the H^+ adsorption brought on by DDA may have worked in harmony to provide the noticeably improved photocatalytic performance. The type-II heterojunction was created that allowed the increased charge separation and migration as well as the reduced recombination of charges. An analogous type-II operation transported photo-excited electrons to the CdS NR from the ZnS shell. Numerous H^+ ions are adsorbed on CdS as a result of the decorating of DDA. The adsorbed proton H^+ swiftly and efficiently caught photo-excited electrons that had accumulated in CdS to generate H_2, which efficiently prevented recombination of charge-carriers. Through a simple hydrothermal process, Lin et al. [255] constructed the core-shell structured CdS/ZnS photocatalyst. With good photo-stability and the optimized CdS–ZnS showed the greatest H_2 generation with 24.1 mmol g^{-1} h^{-1} yielding rate. Utilizing 420 nm irradiation for 9 h, the average AQY reached up to 9.3%. The existence of plenty Zn-defects in ZnS shell prompted the typical type-I CdS–ZnS to transform into a syngenetic form of quasi-Z-scheme and quasi-type-II heterojunctions, which effectively separated photo-induced holes and electrons.

The usefulness and capabilities unique semiconductor can be harvested through careful engineering and construction of 1D/2D multi-dimensional heterojunctions. For intance, Li et al. [256] used the simple two-step solvo-thermal technique to directly develop 2D $ZnIn_2S_4$ NSs on 1D defected CdS NRs surface for preparing the atomic 1D CdS/2D $ZnIn_2S_4$ heterojunctions. The obtained $ZnIn_2S_4$/CdS (ZIS/CdS) heterojunctions exhibited a higher solar-driven H_2 evolution performance. After 4.5 h illumination of light, the optimal ZIS-CdS-0.3 photocatalyst had a significantly increased H_2 production efficiency of 5.80 mmol g^{-1} yielding rate, which was significantly greater to bare CdS and ZIS. For boosting H_2 evolution efficiency of CdS, The NPs of CdS were deposited onto WN NSs surface to prepare WN/CdS composite through one-pot solvothermal approach [257]. The optimized WN/CdS photocatalyst exhibited a superior H_2 production of 24.13 mmol g^{-1} h^{-1} yielding rate, which was better to that of pristine CdS NPs by a factor of 9.28 utilizing visible light irradiation. This enhanced photocatalytic efficiency was ascribed to strong optical absorbing power in visible region, and establishment of interfacial interaction at the Schottky junction involving WN and CdS NPs. Like semiconductors, metal organic framework (MOF) is a novel kind of porous substance. Because of its features including extended reactive sites, enlarged particular surface, and inherent porosity, it is extensively utilized H_2 production during photocatalysis [258]. Liang et al. [259] prepared the UIO-66/CdS composite. Recombination of charge-carriers was efficiently suppressed by utilizing UIO-66. Xia et al. [260] reported a hydrothermal synthesis of Pt–CdS NPs-Zn-TCPP NSs (C-Z-T) type-II heterojunction by growing in situ Pt-loaded CdS NPs on 2D Zn-porphyrin NSs (Zn-TCPP NSs) surface. Zn-TCPP NSs and CdS NPs formed type-II heterojunction reducing recombination of charges. The Pt–CdS NPs-Zn-TCPP photocatalyst exhibited excellent photoctatlytic H_2 production of almost 15.3 mmol g^{-1} h^{-1} yielding rate. This rate was 11-folds for Pt–CdS NPs upon visible light. This efficiency was attributed to existence of Zn-TCPP NSs, which increased optical-absorption efficacy as well as effectively inhibited the photoinduced charges recombinations. In a Type-II heterojunction, although the spatial separation of charge carriers (electrons and holes) occurs, the efficiency of charge separation can be limited by rapid recombination, which hinders the overall photocatalytic performance. The Type-II heterojunction effectively separates the electrons and holes into different components (one on the conduction band of one material and the other on the valence band of the second material), promoting charge migration. However, the relatively low oxidation and reduction potentials in these heterojunctions often lead to insufficient driving force for the desired oxidation-reduction reactions, thus limiting their overall catalytic activity. This limitation stems from the alignment of the energy bands in Type-II heterojunctions, which can result in inadequate potential differences for efficient photocatalytic reactions. Performances of CdS-based type-I and type-II heterojunction photo-catalysts for H_2 evolution from water splitting are shown in

Table 4
H_2 evolution through water splitting using type-I heterojunction photo-catalysts based on CdS.

Catalysts	co-catalysts	Synthetic methods	H_2 evolution rate (mmol g^{-1} h^{-1})	Reference
MoS_2/CdS	MoS_2	hydrothermal	32.94	[225a]
MoS_2/CdS	MoS_2	two-step hydrothermal	38.750	[226]
CdS/MoS_2	MoS_2	–	1.79	[221]
MoS_2/CdS	MoS_2	–	10.85	[229]
CdS@MoS_2	MoS_2	hydrothermal	62.55	[233]
MoS_2/CdS	MoS_2	one-pot hydrothermal	3.135	[228]
MoS_2/CdS	MoS_2	post-sintering	18.43	[237]
MoS_2/CdS	MoS_2	one-pot hydrothermal	3.14	[238]
MoS_2/CdS	MoS_2	two-step hydrothermal	35.24	[238]
NiPS3/CdS	NiPS3	–	13.6	[244]
MoS2/ Ti3C2/CdS	MoS2/ Ti3C2	–	14.1	[261]
MoS2/CdS	MoS2	ultrasonic mixing	27.72	[262]
C/MoS2/CdS	C, MoS2	–	36.7	[263]
CdS–MoS2/C	MoS2, C	liquid phase precipitation	8.796	[264]
$MnCo_2S_4$/ CdS	$MnCo_2S_4$	–	12	[265]
CoP/CdS	CoP	–	4.43	[266]

Table 4 and Table 5, accordingly.

4.2.2. CdS-based p-n heterojunction photocatalysts for H_2 evolution

The idea of p-n heterostructure has been proposed, which might enhance photocatalytic efficiency by quickening charges transportation across heterojunction. Semiconductors of p-type and n-type are coupled to build a potent p-n heterostructure. Electrons in n-type located close to p-n interfaces possess a tendency for diffusing into p-type semiconductor prior to light irradiation, releasing species with a positive charge. Holes in p-type located nearer to p-n contact possess a tendency for diffusing into n-type semiconductor, releasing behind negative charged elements. Diffusion of electron holes proceeds unless the system attain its equilibrium Fermi state. Cao et al. [271] claimed that this results in the creation of internal charged space to build up closer to the p-n contact. Each semiconductor of p-type and n-type undergoes activation and induced pairs of electron and hole when contacted with incoming light having energy equal to or greater compared to bandgaps of semiconducors. Under the influence of the intrinsic electric field, photogenerated electron-hole pairs are separated, with electrons migrating toward the conduction band (CB) of the n-type region and holes toward the valence band of the p-type region, as illustrated in Fig. 8c. Under the influence of the intrinsic electric field, photogenerated electron-hole pairs are separated, with electrons migrating toward the conduction band (CB) of the n-type region and holes toward the valence band of the p-type region, as illustrated in Fig. 8c. Electrons and holes are separated spatially as an outcome. This separation process is thermodynamically feasible. Within a p-n heterostructure, it was observed that the conduction band (CB) and valence band (VB) of p-type semiconductors were frequently positioned beyond those of n-type semiconductors. This alignment was attributed to differences in the Fermi level positions and intrinsic electronic properties of the materials involved. Specifically, the CB of the p-type semiconductor was found at a higher energy level relative to the n-type counterpart, while its VB was observed at a lower energy level. These band alignments facilitated the movement of electrons from the n-type to the p-type region and holes in the opposite direction, contributing to effective charge carrier separation and transfer [272,273]. The band offset created at the heterojunction interface was identified as a critical factor in determining the charge dynamics. This offset was controlled by the electron affinities and ionization potentials of the constituent semiconductors. It was reported that the relative positions of the CB and VB contributed to the formation of a built-in electric field, which promoted directional charge transfer, suppressed recombination, and enhanced the overall performance of optoelectronic and catalytic devices [274,275]. The alignment of the CB and VB in p-type and n-type semiconductors was particularly advantageous for photocatalytic and photovoltaic applications, where efficient separation of photogenerated carriers was essential. Studies further confirmed that these band alignments played a significant role in determining the heterostructure's activity, stability, and efficiency under operational conditions [276,277].

Table 5
Efficiency assessment of H_2 evolution from water splitting utilizing type-II heterojunction photo-catalysts with CdS.

Catalysts	Co-catalysts	Synthetic methods	H_2 evolution rate (mmol g^{-1} h^{-1})	Reference
Pt NF@Ni$(OH)_2$/ CdS	Pt NF/Ni $(OH)_2$	solvothermal	44.05	[183]
Ni$(OH)_2$/CdS-3	Ni$(OH)_2$	photo-deposition	20.14	[70]
CdS–Ni$(OH)_2$	Ni$(OH)_2$	–	29.51	[246]
CdS–ZnO	ZnO	–	9.618	[247]
ZnO/CdS	ZnO	heteroepitaxial growth	6.696	[248]
α-S/CdS	α-S	solvent evaporation-deposition-precipitation	10.01	[250]
CdS–MoS_2	MoS_2	chemical bath	2.3	[251]
CdS NSs/ZnS NPs-0.6	ZnS NPs-0.6	–	14.02	[252]
CdS/ZnS	ZnS	chemical deposition	242.0	[254]
CdS/ZnS	ZnS	hydrothermal	24.1	[255]
1D CdS/2D $ZnIn_2S_4$	$ZnIn_2S_4$	two-steps solvothermal	5.80	[256]
WN/CdS	WN	one-pot solvothermal	24.13	[257]
Pt@CdS NPs/Zn-TCPP NSs(C-Z-T)	Pt/Zn-TCPP NSs (C-Z-T)	–	15.3	[260]
CdS@TiO_2@Au	TiO_2/Au	hard core template	1.720	[267]
$LaFeO_3$/CdS/ CQDs	$LaFeO_3$; CQDs	hydrothermal	25,302	[268]
PdS/CdS/MoS_2	PdS; MoS_2	microwave-assisted	6.610	[269]
MnO_x/g-C_3N_4/ CdS/Pt	MnO_x/g-C_3N_4/Pt	chemical annealing photoreduction	1.30339	[270]

Zhang et al. [278] constructed NiS NP-CdS NR p-n heterostructurevia hydrothermal process. The as-prepared NiS NPs-CdS NRs sample with 5 wt% NiS loading content exhibited a considerable H_2 production with 1.131 mmol g^{-1} h^{-1} in existence of Na_2S/Na_2SO_3 reagents. In comparision to pristine CdS and CdS with a 1 wt% Pt loading, this H_2 generation rate was significantly higher. For at least 9 h, no noticeable deactivation was seen during the photocatalytic reaction, indicating strong durability of composite. The development of p-n heterojunctions was blamed for the improved photocatalytic efficiency. The p-n heterojunction that was created made it easier for charges to move from NiS to CdS and it also prevented charge-carrier recombination. He et al. [279] fabricated CdS/Ag_2S/NiS NR through hydrothermal and photo-deposition process. The optimal CdS/Ag_2S/NiS reached a superb evolution of H_2 with 48.3 mmol g^{-1} h^{-1} upon irradiation in visible range, which was 6.7 and 7.5 folds compared to CdS/Ag_2S or CdS/NiS, respectively. Formation of Schottky junction and p-n heterojunction were both responsible for this better photoatalytic performance by accelerating charge transport and greatly lowering electron-hole pair recombination, Both the oxidation and reduction cocatalysts NiS and Ag_2S acted as photo-generated electron-hole traps.

The MoS_2/CdS p-n heterostructure [279] was prepared through easily solvo-thermal process to demonstrate the improved H_2 evolution

efficiency in photocatalysis. An efficient separation of charges was demonstrated by MoS_2/CdS because of its wider contact surface of the built p-n heterostructure. A maximal H_2 generation rate was 137 μmol h^{-1} over 2D MoS_2/CdS, which was 10-folds better to pristine CdS. The shape of p-n heterostructure photocatalyst was adjusted to provide a plentiful reactive surface and a big specific surface. The 2D MoS_2–CdS–Cu_2O composite of cauliflower-shaped was designed by Kumar et al. [280]. In the existence of lactic acid, the as-prepared novel metal-free 2D MoS_2–CdS–Cu_2O tertiary heterostructure exhibited the maximum water splitting rate of 11.53 mmol g^{-1} h^{-1} along with excellent repeatability. This rate was larger compared to that of MoS_2–CdS upon visible light illumination. Compared to pure CdS, this H_2 production efficiency was 20.96-folds better. The 2D MoS_2–CdS–Cu_2O heterostructure showed the significant AQE of 8.75%. The significant enhancement was because of wide-range optical-harvesting capability up to 900 nm, the promoted interfacial charge-separation, and the suppression of charges recombination, due to build of dual p-n junctions. Zhang et al. [93] synthesized Cu_2S/CdS p-n by integrating CdS QDs and Cu_2S NSs through a versatile template and one-pot sulfdation technique. The resulting 3D hollow octahedral Cu_2S/CdS heterostructure exhibited a maximum H_2 production of 4.76 mmol g^{-1} h^{-1} yielding rate. This H_2 production rate was almost 8.5 and 476-folds better to pure CdS and Cu_2S, respectively. This remarkable performance of Cu_2S/CdS p-n heterostructure was because of powerful light-harvesting efficiency, acceleration of separation of charges, amplification of charges transportation, and abundant reaction sites as a result of the development of hollow architectures. Li et al. [281] synthesized the hollow dodecahedron structured CoS/CdS/CuS composite. The as-prepared CoS/CdS/CuS sequential structure showed a superb production of H_2 with 123.2 mmol g^{-1} h^{-1} yielding rate, and an AQE of 45.6%. This greatly H_2 production performance was because of efficient directional separation of charges owing to electron accumulating effect of CoS, and establishment of internal electric-field at p-n junctions.

MXenes serve a crucial function in lowering the dose of precious metal co-catalysts in photocatalysis. In order to create 2D CdS/2D MXene Schottky heterojunctions, Ding et al. [105] used a solvothermal technique and an electro-static self-assembly approach. The optimal photocatalysts exhibited a highly performance for H_2 production, which was superior to the bare CdS NSs. DFT calculations indicated that the primary cause of the increased photocatalytic H_2 yield rate.was the close Schottky contact between CdS and Mxene, which assisted direct flow of charges development, speeded up charges transportation to MXene from CdS, and suppressed charges recombination. The 2D CdS NSs was anchored on the 2D Nb_2CTX NSs to febricated a new 2D/2D Nb_2CTX/CdS through an electrostatic self-assembly and hydrothermal routes [105]. The optimal CdS/Nb_2CTX-40 showed a comparable H_2 generation of 5.040 mmol g^{-1} h^{-1} yielding rate. This rate was almost 4.3-folds larger compared to that observed on pure CdS NSs. This significant improvement was benefitted from Schottky heterojunction construction. Charges separation and migration were made easier by the Schottky effect, which also improved the redistribution of charges on the CdS/Nb_2CTX. This successfully averted charge-carriers recombination. Li et al. [87] developed CdS@Au/MXene composite via easy in situ self-assembly technique. The optimized CdS@Au/MXene ternary composite with loading of 1 wt% MXene and 0.1 wt% Au obtained a maximum H_2 production with 5.371 mmol g^{-1} h^{-1} yielding rate utilizing illumination in visible region. This H_2 production rate was 26.6-folds better than that obtained on bare CdS. This enhancement was mainly ascribed to the formation of dual Schottky barriers. The charges separation and transfer rate of CdS was improved by the combined efforts of Au and MXene, both of which have strong electro-conductivity, allowing more electrons to take part in photocatalysis.

Deng et al. [282] prepared the hierarchy CdS/NiO hollow p-n heterostructue utilizing simple microwave-assisted moist chemical approach. The optimized CdS/NiO-3 composite (mass ratio of 1:3) had an evolution rate of H_2 that was 16.2-times faster than bare CdS at 1.77 mmol g^{-1} h^{-1}. Strong optical absorption, increased charge carrier separation, and exceptional photo-stability caused by the p-n heterojunctured unique hierarchical hollow and porous architecture were all attributed to the increased H_2 production rate. By coupling CdS with Co_3O_4 through an ultrasonication process, Chen et al. [92] constructed Co_3O_4/CdS photocatalyst for the efficient H_2 production with an excellent stability. The optimized Co_3O_4 (10%)/CdS composites allowed for a steady H_2 evolution with 142.62 μmol h^{-1} yielding rate. This rate was larger compared to CdS by a factor of 20. This higher effiiency was accounted to be facilitated charges transfer because of Co–S chemical bind formation at contact of CdS and Co_3O_4. This performance was also benefitted from the promoted separation of charges, and suppression of recombination of photoinduced charges-carriers by forming of Co_3O_4/CdS p-n heterounction. $Zn_{0.5}Cd_{0.5}S$ (ZnCdS) coupled with 4 wt% MCo_2O_4 was applied in H_2 production in aqueous solution using 420 nm by Chen et al. [92]. It exhibited evolution of H_2 with 0.551 mmol g^{-1} h^{-1} yielding rate without any sacrifices. With existence of Na_2S/Na_2SO_3, the largest H_2 evolution of 78.2 mmol g^{-1} h^{-1} yielding rate was achieved. This rate was better compared to that of Zn–CdS. This improvement was because of efficient separation of charges, and amplification of charges transportation rate between MCoO and ZnCdS, owing to p-n junction forming. Magnetic field of MCoO inhibited charges migration from MCo2O4 to ZnCdS.

Zou et al. [107] fabricated the CdS/CoP hollow composite of CoP-modified CdS NRs. Benefiting from the construction of hollow p-n heterostructure, the as-prepared composite exhibited abounded light active sites, strong light-absorption activity, and excellent charges-separation and transportation. This unexpected photocatalytic efficiency was observed the largest production of H_2 with 15.74 mmol g^{-1} h^{-1} yielding rate. This rate was almost 9-folds compared to bare CdS. Deng et al. [112] fabricated core-shell H–CdS@NiCoP nanospheres through hydrothermal approach. The optimized 7 wt% NiCoP@H–CdS presented an excellent H_2 yielding of 13.47 mmol g^{-1} h^{-1} and high stability for 20 h, which was almost 4 and 2.5-folds superior to bare H–CdS and Pt@H–CdS, respectively. This dramatic improvement was assigned to the amplification of charges transportation rate owing to p-n heterostructure forming. Chen et al. [283] constructed Ni_2P/CdS photocatalyst to exhibit an excellent photocatalytic H_2 generation. The obtained Ni_2P/CdS photocatalyst presented an outstanding photocatalytic H_2 production effciency with 483.25 mmol g^{-1} h^{-1} yielding rate. This rate was found to be almost 525 and 1.92-folds superior to bare CdS and Pt/CdS, respectively with a high AQY up to 70% upon visible light illumination. The development of Schottky heterojunction at Ni_2P/CdS contact facilitated the boosted charges separation and transportation, increasing photocatalytic H_2 generation efficiency. Table 6 shows the results of CdS-based p-n heterojunction photocatalysts for generation of H_2.

4.2.3. CdS-based Z-scheme heterojunction photocatalysts for H_2 evolution

In a conventional Z-scheme heterostructure, semiconductor photocatalysts pair (PS–I and PS-II) act as suppliers and recipients. These two different semiconductors do not establish direct contact. Throughout photocatalysis, photo-excited electrons undergo migration from CB of PS-II to VB of PS-I via a supplier-recipient couple. Photo-excited electrons in CB of PS-II interact with an acceptor, facilitating its reduction to a donor. Simultaneously, photoinduced holes in VB oxidize donor into an acceptor. To achieve spatial charge separation and enhance redox capability, electrons and holes are accumulated on PS-I and PS-II. Traditional Z-scheme photocatalysts are typically limited to construction in liquid phase, constraining their potential photocatalysis applications.

A solid electron intermediary joined two distinct semiconductors (PS–I and PS-II) in the development of an all-solid-state Z-scheme heterostructure by Tada et al. [295]. Upon illumination, electrons were initially promoted to CB while holes emerged in VB of PS-II. Subsequently, Photo-excited electrons were migrated from CB of PS-II to VB of

Table 6
Evaluation of H_2 evolution from water splitting employing p-n heterojunction photo-catalysts with CdS.

Catalysts	co-catalysts	Synthetic methods	H_2 evolution rate (mmol g^{-1} h^{-1})	Reference
NiS NPs/CdS	NiS NPs	two-step hydrothermal	1.131	[278]
CdS/Ag_2S/NiS	Ag_2S/NiS	hydrothermal and photodeposition	48.3	[110]
MoS_2–CdS–Cu_2O	MoS_2/Cu_2O	–	11.53	[280]
Cu_2S/CdS	Cu_2S	a versatile template and one-pot sulfdation	4.76	[93]
CoS/CdS/CuS	CoS/CuS	sequential Ksp-based cation substitution	123.2	[281]
CdS/Nb_2CTX-40	Nb_2CTX	electrostatic self-assembly and hydrothermal	5.040	[105])
CdS@Au/MXene	Au/MXene	in situ self-assembly	5.371	[87]
CdS/NiO-3	NiO	microwave-assisted wet chemical	1.77	[282]
MCo_2O_4/ZnCdS	MCo_2O/Zn	–	78.2	[92]
CdS/CoP	CoP	–	15.74	[107]
NiCoP@H–CdS	Ni/CoP	hydrothermal	13.47	[112]
Ni_2P/CdS	Ni_2P	–	483.25	[283]
MnS/$Mn_{0.2}Cd_{0.8}S$	MnS/Mn	one-pot solvothermal	3.31	[284]
CdS/BCNNTs	BCNNTs	–	0.52602	[285]
NiO/CdS	NiO	–	1.3	[286]
CdS–$Cu_{1.81}S$	$Cu_{1.81}S$	in situ integration	2.714	[287]
$SrTiO_3$/CdS-5%	$SrTiO_3$	chemical bath deposition	4.5379	[288]
BP/CdS	BP	–	5.72	[289]
MnS/CdS	MnS	hydrothermal	5.92	[290]
CdS@$Cu_{2-x}S$	$Cu_{2-x}S$	cation exchange	8.1765	[291]
α-NiS/CdS	α-NiS	in situ grown	9.8	[292]
Cu_2ZnSnS_4/CdS	Cu_2ZnSnS_4	–	11	[293]
H–CdS@NiCoP	NiCoP-7 wt%	hydrothermal	13.47	[112]
TiO_2/CdS	TiO_2	–	21.4	[95]
β-$Ni(OH)_2$/CdS	β-$Ni(OH)_2$	–	~35	[294]
CN–CoO/CdS	15% CN–CoO	–	64.36	[111]
CdS/NiO (CSN0.5)	NiO	*in-situ* chemically depositing	243.9	[83]

PS-I, wherein they were subsequently excited to CB of PS-I, via electron intermediaries (including Pt, Ag, or Au). Consequently, both PS-II possessing upper oxidation potential level, and PS-I having upper reduction potential level, accumulated photo-excited holes and electrons. Spatial separation of holes and electrons induced a distinct spatial effect. MoS_2 quantum dots (QDs) acts as a crucial factor in controlling charge transportation route and minimizing charge recombination in MoS_2. For instance, Chen et al. [296] meticulously regulated the interactions among 1D CdS NRs, 0D MoS_2 QDs, and 2D $ZnIn_2S_4$ NSs to construct an all-solid-state Z-scheme CdS-QDs-$ZnIn_2S_4$ heterostructure, where MoS_2 QDs acted as solid-state electron mediators. The H_2 evolution over CdS-QDs-$ZnIn_2S_4$ composite reached to 2.1075 mmol g^{-1} h^{-1} yielding rate, surpassing that of pristine $ZnIn_2S_4$ NSs and pure CdS NRs by factors of 26 and 62, respectively. The remarkable charge separation and efficient electron mediation by MoS_2 QDs contributed to the exceptional photocatalytic efficiency. The prepared CdS/QDs/$ZnIn_2S_4$ exhibited high durability for H_2 production, attributed to the successful Z-scheme separation of charges facilitated by MoS_2 QDs. This enabled efficient charges-separation and retained higher redox efficiency. The utilization of all-solid-state Z-scheme in liquid, gaseous, and solid media could enhance their photocatalytic efficacy. Nevertheless, the high cost and limited availability of electron intermediators needed to improve electrons transportation channel in all-solid-state Z-scheme constrain their widespread use in industrial applications.

A direct Z-scheme was presented by Yu et al. [297] for heterojunction building. Without using electron intermediators, two distinct semiconductors were combined to develop direct Z-scheme (Fig. 8d) [223]. The preparation process of this heterojunction is similar to that of a usual all-solid-state Z-scheme, having the exception that this system does not require expensive and scarce electron intermediaries. With the inclusion of semiconductors with greater oxidation and reduction potentials, the developed Z-scheme was able to spatially separate electron and hole. Compared to type-II systems, construction expenditure of direct Z-scheme is lower. To facilitate particular photocatalytic activities, its redox potential can be tailored. The migration of charge upon this Z-scheme is substantially much beneficial compared to type-II, owing to electro-static attraction connecting electron and hole. The transportation of photo-excited electrons from CB of PS-II to photo-excited hole-rich VB of PS-I is facilitated by forming of direct Z-scheme. Electrostatic repulsion between electrons is believed to make it harder for type-II systems to facilitate photo-induced elecgrons transportation to the photo-excited electron-affluent CB of Semiconductor-I from CB of semiconductor-II. Photo-excited electrons contains in greater CB's semiconductor whilst holes remains in lower VB's semiconductor, owing to more efficiently charges separation and products in direct Z-scheme, and prevention of reverse reactions. The performance of H_2 evolution is enhanced by building a direct Z-scheme. The bandgap reduction of CdS and the corresponding photocatalytic efficiency for direct Z-scheme CdS-based photocatalysts is presented in Fig. 10. As Fig. 10, the performances of H_2 production on direct Z-scheme CdS-based photocatalysts does not follow the reduction sequence of bandgap of CdS. For $W_{18}O_{49}$ QDs/CdS and $ZnIn_2S_4$/CdS direct Z-scheme photocatalysts, it was exceptional. Because the photocatalytic efficiency of a photocatalysts does not only depends on its bandgap. It also depends on other many factors including its interfacial and structural properties. For instance, The CdS@$ZnIn_2S_4$ hierarchy composites having chemically linked interface by growing $ZnIn_2S_4$ NSs on CdS hollow cubic surfaces was constructed by Zhang et al. [298]. The as-prepared photocatalyst was potentially effective due to direct Z-scheme formation. A maximum H_2 generation of 0.5403 mmol g^{-1} h^{-1} yield rate was observed from pure water on the CdS@$ZnIn_2S_4$ hierarchical hollow cubes by visible light, which was better to physical

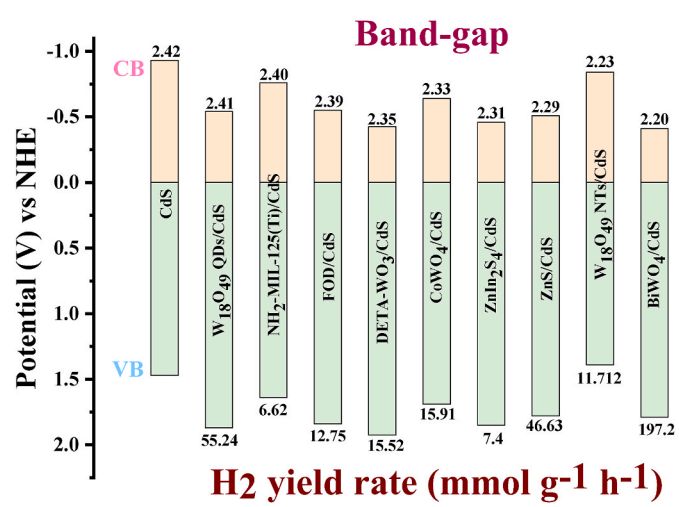

Fig. 10. Schematic illustration of bandgap reduction of CdS and photocatalytic performance for direct CdS-based Z-scheme (Pristine CdS [299], $W_{18}O_{49}$/CdS [67], NH_2-MIL-125(Ti)/CdS [101], FOD/CdS [300], WO_3/CdS-DETA [301], $CoWO_4$/CdS [302], $ZnIn_2S_4$/CdS [303], CdS/ZnS (CSZS-VZn) [94], $W_{18}O_{49}$ NTs/CdS [73], $BiVO_4$/CdS [84]).

mixing of CdS hollow cubes and $ZnIn_2S_4$ NSs. The as-prepared CdS@$ZnIn_2S_4$ exhibited an AQE of 1.63 % at 400 nm with good stability during four consecutive cycles. This improvement was attributed to efficient separation and transportation of charges in the formed direct Z-scheme.

The narrow bandgap and proper band-structure of α-Fe_2O_3 has been made it outstanding contender to built direct Z-scheme with CdS for H_2 evolution by visible light illumination. The α-Fe_2O_3/CdS Z-scheme suppressed rapid recombination of charges as well as photo-corrosion of CdS photocatalyst. Construction of 0D-2D Z-scheme heterostructure can facilitate extended interfacial surface to increase charge-mobility at the interface. Guo et al. [304] fabricated the 0D/2D CdS/α-Fe_2O_3 (CF) heterostructure by decorating CdS NPs on the hexagonal Fe_2O_3 NSs through a facile solvothermal route. The optimized CdS/α-Fe_2O_3 (CF-15) photocatalyst resulted in a higher production of H_2 with 1.806 mmol g^{-1} h^{-1} yielding rate. The largest AQE of 13.7% at 420 nm was also observed. This enhancement was attributed to an intimate contact of 0D/2D interfaces and the synergistic effect of Z-scheme. The capability of affordable blue $W_{18}O_9$ for optical-harvesting in the UV to NIR range originated from SPR, making it exceptional photocatalysts for solar energy conversion. An abundance of photons of low energy can accumulate for creating hot electrons of higher energy through utilizing plasma photocatalyst. The photocatalytic efficiency of a semiconductor can be improved by inducing charge injection of LSPR through combining a plasma photocatalyst. Yang et al. [73] utilized a hydrothermal route for constructing CdS@$W_{18}O_{49}$ nanotubes (NTs) direct Z-scheme heterostructure by wrapping CdS NPs into the hollow $W_{18}O_{49}$ NTs. High evolution of H_2 upon irradiation of light in UV to NIR range was obtained, reaching 11.732 mmol g^{-1} h^{-1} and outstanding stability on the as-prepared CdS@$W_{18}O_{49}$ NTs in absence of sacrificial reagents. An excellent AQY up to 18.3% at 420 nm was also observed. This improved photocatalytic H_2 production rate of CdS@$W_{18}O_{49}$ NTs were significantly greater to pure CdS. These improved efficiencies was attributed to the increased optical absorption ability in wide range of UV to NIR, the acceleration of charges-transportation, the extremely loned life-time of photo-excited charges. The self-guarding function of $W_{18}O_{49}$ NTs was responsible for its extremely high stability of H_2 production. Further, Yin et al. [305] constructed the new $NiWO_4$/CdS heterostructure by growing $NiWO_4$ NSs on surface of CdS NRs. Compared to pristine CdS, the resultant $NiWO_4$/CdS exhibited 75-folds enhancement in the evolution of H_2. This outstanding $NiWO_4$/CdS direct Z-scheme photocatalytic performance was attributed to abundant reactive sites, close contact, and strong ability to separate photoinduced charges.

The porous-type C–ZnO/CdS NRs was constructed by Liang et al. [306] via self-template route utilizing ZIF-L. The Pt–C–ZnO/CdS NRs showed an efficient H_2 production performance of 20.25 mmol g^{-1} h^{-1} yield rate by illumination of visible light. This H_2 yielding rate was much larger greater than bare CdS, and ZnO, accordingly. AQY of 24.7% was observed under 365 nm wavelength of light on Pt–C–ZnO/CdS heterostructure. This greatly increment of photocatalytic performance was because of the remarkable amplified separation of charges and the promoted photo-induced charges-transportation due to direct Z-scheme heterojunction. Doping of C with ZnO not only narrowed the bandgap of ZnO but also widened the range of its spectral response. Recombination of charges was effectively restricted by orderly arrangement of porous NRs. The ZnS–CdS composite presented higher photocatalytic evolution of H_2. Yu et al. [94] constructed the Zn-vacancy defected CdS–ZnS (CSZS-VZn) direct Z-scheme heterostructure through a hydrothermal route. A maximum evolution of H_2 amounted to 46.63 mmol g^{-1} h^{-1} and AQY of about 9.5% under visible light illumination on CSZS-VZn heterostructures in existence of Na_2S/Na_2SO_3 reahents. This rate was almost 1727-folds better compared to ZnS–VZn. This photocatalytic improvement was owing to built of direct Z-scheme heterostructure. The formed CSZS-VZn Z-scheme led to promote optical-absorbing capability, accelerate charges separation and transportation. The photo-induced holes interact with photo-excited electrons from the Zn-vacancy defective layer in the CdS's VB, preventing photo-corrosion successfully. The established electric-fields transported electrons to the surface faster by coating of ZnS. It provide electrons to ZnS from CdS. Song et al. [307] fabricated the ternary MoS_2/ReS_2@CdS hybrids by growing ReS_2@CdS on MoS_2. Dual co-catalysts formed the heterojunction with CdS. Owing to the co-presence of both ReS_2 and MoS_2, the MoS_2/ReS_2@CdS photocatalyst exhibited the outstanding performance for evolution of H_2 during photocatalysis. The obtained sample presented the superb H_2 production of 171.9 mmol g^{-1} h^{-1} yield rate. This superb photocatalysis efficiency was because of acceleration of photo-generated charges mobility, and strong light-absorption ability of MoS_2/ReS_2@CdS. These improvements were benefitted from the dual Z-scheme paths in heterojunctions. Photocatalytic functions of MoS_2/ReS_2@CdS varied with loading content of rhenium. The remarkable improvement was brought through introducing a small amount of rhenium.

The construction of direct Z-scheme efficiently sped up separation of charges and promote transportation of photo-excited charge-carriers. The redox performance of $BiVO_4$ during photocatalysis might be greatly improved by decorating CdS. Recent years have seen some impressive research on Z-scheme CdS/$BiVO_4$ composites in photocatalysis. For example, Zhou et al. [308] created 1D CdS/$BiVO_4$ NWs via hydrothermal process. These nanowires, which included 33.3 wt% CdS, demonstrated a favorable H_2 evolution up to 1.153 mmolh^{-1} in existence of Platinum. H_2 evolution efficiency on $BiVO_4$ NS decorated with CdS was reached to 0.57 mmol h^{-1} by visible light illumination, which was approximately 5.18-folds greater to pristine CdS nanoparticle. It is important for logical design, development, and application of materials to examine charge-transportation routes as well as photocatalytic performance of CdS/$BiVO_4$ in photocatalysis. This photocatalytic performances of m-$BiVO_4$ and CdS/$BiVO_4$ must be sufficiently explored. Lin et al. [84] utilized hydrothermal process for constructing the hollow CdS/$BiVO_4$ photocatalyst by adjusting the CdS percentage. They discovered that the optimized CdS/$BiVO_4$ photocatalyst with a 25 wt% CdS concentration under UV–vis light produced H_2 at an unusually 197.2 mmol g^{-1} h^{-1} yielding rate. This rate was 5.7-folds better compared to pristine CdS. As Fig. 10, this H_2 evolution rate was the highest rate among other CdS based direct Z-scheme heterojunctions. The built of internal electric-field in CdS/$BiVO_4$ direct Z-scheme composite led to efficient transfer of charges, the restricted recombination of charges, and extension of life-time of e^-/h^+ pairs. $BiVO_4$ and CdS were in close contact, which facilitated effective charge carrier transfer. $BiVO_4$ and CdS have appropriate band-gaps and their bande-edge positions. The performances of CdS-based direct Z-scheme photo-catalysts for H_2 evolution from water splitting are given in Table 7.

4.2.4. CdS-based S-scheme heterojunction photocatalysts for H_2 evolution

Although the photo-excited charge-carriers are successfully separated and their life-times are prolonged for surface catalysis by formation of type-II heterostructure. From perspective of thermodynamics, charges transportation mechanism in type-II system unquestionably reduces electrons' reduction capability and holes' oxidation capability during photocatalysis. The shortcomings of all-solid-state and conventional Z-scheme photocatalysts have an adverse effect on direct Z-scheme photocatalysts. In these cases, eliminating type-II and Z-scheme is preferable in order to adopt a fresh idea that more accurately and consciously depicts photocatalysis. The improved photocatalytic performance of heterojunction photocatalysts has been explained using a unique step-scheme (S-scheme) heterojunction. The S-scheme effectively separates electrons from holes while maintaining possible photoiexcited charge-carriers' redox abilities. In accordance with band diagram, photocatalysts can be categorized as reduction (RP) or oxidation (OP) as depicted in Fig. 8e [57]. S-scheme heterojunction comprises a combination of RP and OP having staggered band geometries and is identical to type-II yet having an entirely distinct charge transit mechanism. In the case of RP systems, photogenerated holes are relatively ineffective and require scavenging by sacrificial agents to prevent

Table 7
Assessment of H_2 evolution from water splitting using direct Z-scheme heterojunction photo-catalysts with CdS.

Catalysts	co-catalysts	Synthetic methods	H_2 evolution rate (mmol g^{-1} h^{-1})	Reference
$W_{18}O_{49}$/CdS	$W_{18}O_{49}$	–	55.24	[95]
CdS@$ZnIn_2S_4$	$ZnIn_2S_4$	–	0.5403	[298]
NH_2-MIL-125 (Ti)/CdS	NH_2-MIL-125 (Ti)		6.62	[101]
FOD/CdS	FOD	–	12.75	[300]
WO_3/CdS-DETA	WO_3/CdS-DETA	–	15.522	[301]
$CoWO_4$/CdS	$CoWO_4$	–	15.91	[302]
$ZnIn_2S_4$/CdS	$ZnIn_2S_4$	–	7.4	[303]
CdS/ZnS (CSZS-VZn)	ZnS/VZn	hydrothermal	46.63	[94]
$BiVO_4$/CdS	BiVO4	–	197.2	[84]
CdS/α-Fe_2O_3	α-Fe_2O_3	solvothermal	1.806	[304]
CdS@$W_{18}O_{49}$	$W_{18}O_{49}$	hydrothrmal	11.732	[73]
$NiWO_4$/CdS	$NiWO_4$	–	26.43	[305]
Pt/C–ZnO/CdS	Pt' C; ZnO	self-template	20.25	[306]
MoS_2/ReS_2@CdS	MoS_2/ReS_2	–	171.9	[307]
g-C_3N_4/CdS	g-C_3N_4/CdS	–	1.80907	[309]
CdS/CoS_x	CoS_x	–	9.47	[310]
CdS/Co_9S_8	Co_9S_8	–	11.6	[311]
CdS/$W_{18}O_{49}$/g-C_3N_4	$W_{18}O_{49}$/g-C_3N_4	–	11.658	[99]
WO_3/CdS/WS_2	WO_3/WS_2	synthetic	14.34	[312]
CdS-NiPc	CdS-NiPc	solvothermal	17.74	[313]
Pt–C_3N_4/CdS	Pt–C_3N_4	Ionic layer absorption	35.3	[102]
CoS/CdS	CoS	self-template & solvothermal	39.29	[314]
Pt–CdS/Fe_2O_3	Pt/Fe_2O_3	–	39.4	[315]
PdO_x@HCdS@ZIS@Pt	PdO_x@ZIS@Pt	template	86.38	[316]
Co_2RuS_6/CdS	Co_2RuS_6	–	110.66	[317]
CdS/MIL-53(Fe)	MIL-53(Fe)	–	2.01	[318]
CdS@TTI–COF–60	TTI–COF–60	–	2.8517	[319]

undesired recombination, whereas photoexcited electrons play a functional role in the desired processes. Conversely, in OP systems, photogenerated holes, rather than electrons, serve as the primary active species, significantly contributing to environmental degradation. Photo-excited electron and hole are accumulated into the usual type-II system by CB of OP and VB of RP, correspondingly, which results in a poor redox capaability. On the other hand, CB of RP and VB of OP accumulate rich electrons and holes, respectively, into S-scheme heterojunction, which results potent redox abilities due to lower charges recombination. In comparison to OP, a low work-function was possessed by RP with greater VB and CB positions. If both these semiconductors exist in immediate contact, the electrons of RP spontaneously diffuse to the OP, forming a depletion and accumulating layers of electrons, respectively, close to contact that connects RP and OP. OP and RP possess negative and positive charges, respectively. As seen in Fig. 8e, an interior electric-field is built that simultaneously directs towards OP from RP. This interior electric-field promoted photo-induced electrons transmission from OP to RP instead of the reverse. Compared to OP, CB and VB positions are greater in RP. Interior electric-field, electro-static attractive force, and band-bending drive recombination of CB electrons of OP and VB holes of RP, but potent photo-induced CB electrons of RP and VB holes of OP retain for participating the photocatalysis. Notably, since no additional sacrificial agents are required, photocatalytic total water splitting is the best method for achieving solar-to-chemical conversion. The potent redox capabilities provide it a thermodynamic edge in the entire water splitting process in S-scheme system. Because photocatalysis is intricate, dynamics as well as thermodynamics play a role in them. Some techniques, including appropriate adding of co-catalyst, tuned morphology, and optimal interface can be used for reducing activation barrier of photocatalysis, speed up separation of charges, and diffusion for creating S-scheme photocatalysts having better efficiency.

The 1D nanofibers (NFs) are considered to be one of the most appropriate substances for energy-associated applications due to their distinctive structure. They may boost a particular surface area, minimize the transportation of ions length, and make it simpler for electrons to travel lengthwise throughout their 1D route. Ge et al. [57] synthesized a new 1D TiO_2–CdS nanofibers through electro-spinning route. This as-synthesized nanofibers exhibited a considerable production of H2 with 2.32 mmol g^{-1} h^{-1} yield rate by illumination in UV–visible range, and an AQE of 10.14%. This H_2 production rate was 35-folds more compared to bare CdS NFs. This enhancement was because of 1D well-distributed structure, plentiful active sites, and the accelerated separation and transportation of charges by forming TiO_2–CdS NFs S-scheme. Employing in-situ growth, a S-scheme heterojunction photocatalyst was prepared by growing inorganic semiconductor firmly onto organic semiconductor [58] using a substrate on which for anchoring CdS nanocrystals, pyrene-alttriphenylamine (PT), a novel pyrene-based conjugated polymer. The optimized CdS-PT composite with 2 wt% PT loading content demonstrated a strong H_2 production of 9.28 mmol g^{-1} h^{-1} and an excellent AQE of 24.3%. This rate was nearly 8-folds compared to pristine CdS sample. The efficient separation and transportation of charges as well as higher redox ability, is primarily responsible for dramatically improvement of photocatalytic efficacy. Ni et al. [86] built the new binary CdS/ZnTHPP nanosystem via a facile sintering process. The obtained CdS/ZnTHPP photocatalyst exhibited outstanding H_2 evolution of 50 mmol g^{-1} h^{-1} yielding rate by irradiation of sun-light for 128 h, which was better compared to pristine CdS NRs by a factor of 10. The improvement of photocatalytic performance was because of fast transportation of charges, inhibition of charges recombination, and plentiful reactive sites owing to build of S-scheme in CdS/ZnTHPP binary hetero-structure.

By employing molecular assembly strategy, Ran et al. [320] developed the nanostructured g-C_3N_4/CdS through a simple hydrolyzing and reassembling route. The optimized g-C_3N_4/CdS heterostructure displayed a considerable H_2 production of 3.37 mmol g^{-1} h^{-1} by illumination in visible range, which was greater compared to hydrolyzed g-C_3N_4 by a factor of 3.5. This efficient activity was benefitted from the S-scheme charges separation and transportation. The novel ternary Ti_3C_2/ZIS/CdS photocatalyst was constructed by modifying via two-step solvo-thermal route [247]. The maximum H_2 generation rate with 8.93 mmol g^{-1} h^{-1} using visible light was observed on Ti_3C_2/ZIS/CdS photocatalyst. The Ti_3C_2/ZIS/CdS composite also exhibited the significant AQE of 3.42% at 450 nm. This remarkable enhancement of photocatalytic efficiency was benefitted from synergistic impact involving ohmic junction and Van Der Waals S-scheme heterojunction. Charges-separation efficiency was improved by the formation of this

S-scheme. The intimate 2D/2D van der Waals form not only provided the strong interaction force but also extended the contact area for promoting transportation of charges. Charges recombination was suppressed through the formation of accumulation layer by adding 2D Ti_3C_2. CdS NSs was grown on metallic Ti_3C_2 MXene (MX) and WO_3 NSs to fabricate the 2D MX-CdS-WO_3 S-scheme heterostructure [60]. A maximum H_2 production with 27.5 mmol g^{-1} h^{-1} yielding rate on the optimum 2D MX-CdS/WO_3 was determined by visible light illumination. This rate was 11-folds higher than pristine CdS NSs sample. The obtained 2D MX-CdS/WO_3 sample further showed the highest AQE of 12.0% at 450 nm. This highly photocatalytic efficiency was because of the faster directional charges-separation and transportation. The NiS–Mo_2C–CdS ternary photocatalyst was fabricated by Shen et al. [54] for H_2 production. The as-prepared NiS–Mo_2C–CdS presented outstanding H_2 production of 24.03 mmol g^{-1} h^{-1} yielding rate. This rate was 3.83 and 7.83-folds better compared to that of CdS–NIS and pristine CdS. This improvement was because of ternary S-scheme building. The ternary CdS–MoS_2–In_2O_3 NRs was fabricated by Zhang et al. [321]. The as-prepared composite not only exhibited a notably production of H_2 upon stimulated light illumination but also produced a large number of visible bubbles under natural light. Comparing to bare CdS NRs, the outstanding production of H_2 of 198.58 mmol g^{-1} h^{-1} yielding rate was obtained after conjunctions of MoS_2, and MOF-derived In_2O_3 hollow hexagonal prism under simulated light of 300W. The significant improvement was primarily due to development of S-scheme heterojunctions, directionally transfer of photoinduced charges, and feasibility of separating redox active sites in space. Significant photocatalytic hydrogen evolution was facilitated by MoS_2 in CdS–In_2O_3 S-scheme. Table 8 lists the abilities of CdS-based direct S-scheme heterojunction photo-catalysts for generation of H_2.

4.3. CdS-carbon group (C,CNTs, graphene) heterojunction photocatalysts for H_2 evolution

Because nano-C substances have a stronger capability to transport electrons, such as C-NTs, C-QDs, G, and rGO, the separation and transportation of charges can be greatly facilitated by their employment. To boost the photocatalytic efficiency of CdS, carbon has been recognized as an effective doping agent. The impact of C-doping on CdS films led to better photo-electrochemical characteristics [332]. Because of its greater density of carriers and effective charges-separation, doping of C in CdS has a beneficial impact on photocatalytic H_2 production. Because of its superb optical qualities, potent confinement impact, and superior electrical conductivity, and photo-luminescent, CQDs have attracted a great deal of interest. It is extremely desirable to combine CdS with metal-free, affordable, and environmentally friendly substances like CQD in a straightforward manner. CQD is an emerging photo-luminescent nanomaterial which has gained significant attention in research because of its new photoluminance intensity, lower harmful effects, and remarkable photo-durability with 0D nanoscale elements [333]. The integration of CQD onto semiconductor products was performed to maintain photodurability. For instance, Gogoi et al. [82] constructed the CQDs substance from peels of oranges and integrated it into the 1-D CdS NWs. Utilizing optimized 0.4CQD/CdS upon illumination of visible light, an exceptional H_2 yielding of 309 mmol g^{-1} h^{-1} was achieved. At 420 nm, this further exhibited an AQY of 32.6%. The addition of CQD greatly increased the photo-stability of CdS. This exceptional charges-separation and transportation capabilities of the CdS within CQD/CdS, the inhibited recombination of charges, and the application of optimal conditions were primarily responsible for boosting H_2 generation efficiency. Carbon nanotubes (CNTs) offer a wide range of possible applications for their exceptional hydrophobicity, CNT can operate as electron transporter by exciting electrons to move from CdS CB to the TiO_2–$Ni(OH)_2$–CdS heterojunctions if these materials are connected. Wang et al. [71] developed a TiO_2–$Ni(OH)_2$-CNT/CdS composite utilizing an ordinary fluid chemistry synthesizing approach at ambient temperature. The as-prepared sample presented a remarkable H_2 production of 12 mmol g^{-1} h^{-1} yielding rate with highly durability. This improvement was mainly attributed to effective separation of charges and charges mobility.

Graphene is a single-layer carbon nanomaterial of 2D honeycomb structured substance. As an excellent transporter of photocatalysts and recipients to photoinduced charge, graphene (G) features a large effective area of surface, rapid electron transportation, variable bandgap, and remarkable optical, thermal, and mechanical capabilities [334]. For instance, Jia et al. [335] constructed the N-G/CdS photocatalyst to produce H_2. The optimum N-G/CdS sample with 2 wt % N-graphene loading content presented a significant production of H_2 with 210 μmol h^{-1} yield rate upon illumination in visible range. This H_2 evolution rate was better compared to that of graphene-CdS and GO-CdS. This enhancement was owing to the promote separation and transportation of charges. Upon illumination of light, photo-corrosion of CdS was prevented by utilizing N-G as co-catalyst. Pure graphene could be substituted with reduced graphene oxide (rGO), a superior substance. Along with exhibiting numerous of the identical physical and chemical features as pure graphene, rGO is economically viable and considerably

Table 8
Performances of CdS-based direct S-scheme heterojunction photo-catalysts for H_2 evolution from water splitting.

Catalysts	Co-catalysts	Synthetic methods	H_2 evolution rate (mmol g^{-1} h^{-1})	Reference
TiO_2/CdS	TiO_2	In situ electrospinning	2.32	[57]
CdS/PT	PT	–	9.28	[58]
g-C_3N_4/CdS	g-C_3N_4	Hydrolyzing and reassembling	3.37	[320]
Ti_3C_2/$ZnIn_2S_4$/CdS	Ti_3C_2/$ZnIn_2S_4$	Two-step solvothermal	8.93	[60]
2D MX-CdS/WO_3	2D MX-CdS/WO_3	–	27.5	[61]
NiS/Mo_2C/CdS	NiS/Mo_2C	–	24.03	[54]
CdS–MoS_2–In_2O_3	MoS_2/In_2O_3	–	198.58	[321]
ZnO–CdS/Pt	ZnO–CdS/Pt	Template-free	32.15	[322]
CdS–ZnO	CdS–ZnO	–	14.36	[323]
WO_3/CdS/g-C_3N_4 QDs	WO_3/CdS/g-C_3N_4 QDs	Hydrothermal-chemical-annealing	~1.91212	[324]
MnO_2/CdS	MnO_2	Chemical co-precipitation	3.94	[72]
CuO/CdS/$CoWO_4$	CuO/$CoWO_4$	Hydrothermal & microwave	4.579	[325]
FI/CdS	FI	Luminescent quenching	5.28	[326]
ZnO/CdS	ZnO/CdS	Hydrothermal	7.669	[327]
COF/CdS	COF	–	8.67	[328]
ZnO/CdS/MoS_2	ZnO/MoS_2	–	10.2474	[103]
Porous g-C_3N_4/CdS-diethylenetriamine	Porous g-C_3N_4/diethylenetriamine	Microwave	12 0.547	[329]
$W_{18}O_{49}$/CdS	$W_{18}O_{49}$	–	15.4	[56]
$H_3PW_{12}O_{40}$/CdS	$H_3PW_{12}O_{40}$	Hydrothermal	18.7	[330]
MXene/CdS/WO_3	MXene/WO_3	–	27.5	[61]
Mn–CdS/Cu_2O	Mn/Cu_2O	Hydrothermal	66.3	[331]

producible [336]. Increased AQE of 10.4% was reported by Zeng et al. [337] for CdS when rGO was used as a co-catalyst to collect the electrons from the photoexcited CdS. Catalyst particles are challenging of adsorption for graphene or rGO sheets because of lacking functional groups. Though a number of investigations have focused on developing high activity rGO-based photocatalysts, the methodology by which photocatalysts are added onto rGO sheets, receiving very little attention. Hong et al. [338] prepared the CdS/GO composites through in situ of CdS on GO utilizing a facile solvo-thermal route. Then, rGO was prepared by photoreducing the GO present in the produced powders. Upon visible light irradiation (>420 nm), the optimal 5 wt% rGO/CdS showed much more efficiency for H_2 production up to 1.470 mmol h^{-1} than CdS or CdS mechanically loaded with GO. The enhanced interaction between CdS and rGO sheets speeded up separation of photo-induced electron and hole by transferring the photoinduced electron to RGO sheets. This was credited to the increased photocatalyst effectiveness of CdS/rGO.

The charges transportation and photocatalytic performance were increased by coupling GO with MoS_2. GO features excellent charges monility, enlarged area of active surface, and strong optical absorption ability in visible range. A new CdS/MoS_2/rGO composite was constructed by Tan et al. [113] rGO via hydrothermal and in situ growth approaches. The optimum 0.35 wt% CdS/MoS_2/rGO exhibited an excellent H_2 production performance with 11.33165 mmol g^{-1} h^{-1} yielding rate. This was 4-folds larger to that of pure CdS. An AQY of 10.4% was also determined at 420 nm with excellent durability. This improved performance was because of rapid tramsportation of charges, and suppression of recombination of charges owing to MoS_2/rGO co-catalysts loading. The CuS NPs played a pivotal role in enhancing visible-light responses and demonstrated CuS NPs displayed strong optical responses and an excellent photocatalytic functions. The optimal CuS–ZnO/rGO/CdS sample presented a considerable H_2 evolution of 1.073 mmol g^{-1} h^{-1} yielding rate. This improvement was attributed to prolonging life-time of photo-excited electrons, amplification of charges transportation abilities. An improved H_2 production performance was presented by porous-type carbon substance. The photocatalytic efficiency was boosted by porous-type grapheme or its ramification through extending reactive surface and promoting charges transportation capability. For example, the multi-walled carbon nanotubes (MWCNTs) were synthesized by Dai et al. [114] and exfoliated into PRGO-supported inorganic-organic CdS-diethylenetriamine (DETA) hybrids. This new PRGO/CdS-DETA system demonstrated excellent H_2 yield of 10.5 mmol g^{-1} h^{-1} and AQE of 29.5% with better photo-stability when exposed to visible light (>400 nm). The distinctive relationship involving PRGO and CdS-DETA built it easier for charge-carriers to separate, and the high photocataly H_2 production of CdS-DETA was increased by the extended BET particular area. A novel perspective on the structure of photocatalytic compounds might be offered by PRGO/CdS-DETA with excellent photocatalytic H_2 production ability. The performances of CdS-carbon group heterojunction photo-catalysts for production of H_2 is presented in the Table 9.

5. Photo-corrosion of CdS in the photocatalytic H_2 evolution

Cadmium sulfide (CdS) photocatalysts, although widely studied for their ability to drive water splitting and hydrogen production under visible light, suffer from a significant limitation: photocorrosion. Photocorrosion refers to the degradation of the photocatalyst material under light irradiation, leading to a decrease in photocatalytic activity and potential environmental concerns due to the release of toxic cadmium ions. This issue is primarily due to the instability of CdS under photocatalytic conditions, where the photogenerated electrons and holes can promote the dissolution of CdS into Cd^{2+} and S^{2-} ions. Several strategies have been proposed to mitigate photocorrosion in CdS photocatalysts, which include material modification, co-catalyst deposition, and the use of protective coatings or sacrificial agents.

One approach to address photocorrosion has been the modification of CdS through doping with other metals or non-metals. Doping has been shown to enhance the stability and photocatalytic activity of CdS by modifying its electronic structure and improving its charge carrier dynamics. For instance, noble metal doping, such as with platinum (Pt) or gold (Au), has been reported to significantly reduce the rate of photocorrosion in CdS by acting as electron sinks, which prevents the accumulation of photogenerated electrons on the surface of CdS. This reduces the likelihood of electron-induced dissolution of the material. Pt, in particular, has been shown to stabilize CdS by promoting charge separation and enhancing the efficiency of the photocatalytic reaction [129]. Transition metal doping with elements like nickel (Ni), cobalt (Co), and copper (Cu) has also been explored to improve the charge carrier separation and reduce photocorrosion, by acting as electron traps and providing additional pathways for charge recombination [354]. Another strategy to mitigate photocorrosion in CdS photocatalysts is the deposition of protective metal layers or co-catalysts. The deposition of metals such as platinum (Pt) or silver (Ag) onto the surface of CdS can act as protective layers that help prevent direct exposure of CdS to the photocatalytic reaction environment, thereby reducing the dissolution of CdS into its ionic form. These metal co-catalysts can also improve charge separation and transfer, which increases the efficiency of photocatalytic reactions. For instance, Pt-deposited CdS has been shown to

Table 9
Evaluation of H_2 evolution from water splitting using CdS-carbon group heterojunction photo-catalysts with CdS.

Catalysts	Co-catalysts	Synthetic methods	H_2 evolution rate (mmol g^{-1} h^{-1})	Reference
CQD/CdS	CQD	Chemical adsorption	309	[82]
TiO_2–$Ni(OH)_2$/CNT/CdS	TiO_2/CNT/$Ni(OH)_2$	Liquid chemistry synthetic	12	[71]
CdS/MoS_2/rGO	MoS_2/rGO	Hydrothermal and in situ growth	11.33165	[113]
PRGO/CdS-DETA	PRGO/DETA	–	10.5	[114]
C-doped CdS@G	C/G	–	3.12	[339]
CdS/CA/rGO	CA/rGO	Self-assembly	3.3	[340]
C@CdS-HS	C	Hydrothermal	20.9	[341]
CDs/CdS–S	CDs/S	–	4.64	[342]
CdS@CA	CA	–	~27.3	[343]
GO/CdS/ZnO	GO/ZnO	Microwave-assisted co-precipitation	6.511	[344]
CoP/CdS/rGO	CoP/rGO		1.4	[345]
CdS/rGO	rGO	–	0.5	[340]
CdS-rGO-MoS_2	rGO-MoS_2	Hydrothermal	7.1	[346]
$(RGO)_2$-CdS-Ni_xS	$(RGO)_2$-CdS-Ni_xS	–	17.5	[347]
rGO-CdS-Alginate	rGO-Alginate	–	79.68	[348]
CdS–MoS_2/RGO-E	MoS_2/RGO-E	Solvothermal	36.7	[349]
CdS-rGO-Sodium Alginate	rGO-SodiumAlginate	–	6	[350]
$Ni(OH)_2$–CdS/rGO	$Ni(OH)_2$/rGO	–	4.371	[351]
g-C_3N_4/CdS/rGO	g-C_3N_4/rGO		4.8	[352]
CdS/NiS/RGO	CdS/NiS/RGO	–	14.96	[353]

exhibit enhanced photocatalytic stability and efficiency in water splitting due to the synergy between the metal and the CdS surface [125]. Graphene and graphene oxide have also been used as stabilizing materials for CdS by forming hybrid composites, which not only reduce the rate of photocorrosion but also enhance the overall photocatalytic performance (Pal et al., 2015).

Surface modification and passivation techniques have also been employed to reduce photocorrosion. The introduction of a thin protective shell made of more stable materials, such as TiO_2 or ZnS, onto CdS can protect the core material from direct exposure to harsh reaction environments, preventing its degradation. A ZnS shell, in particular, has been shown to effectively inhibit the photocorrosion of CdS by passivating the surface and preventing the release of Cd^{2+} ions during photocatalytic reactions [355]. The shell also helps in improving the light absorption properties and charge carrier separation efficiency of the composite photocatalyst. In addition to material-based strategies, the use of sacrificial agents has been proposed as a means of mitigating photocorrosion during photocatalytic water splitting reactions. Sacrificial agents, such as sulfur (S) or thiol compounds, can be added to the reaction medium to scavenge photogenerated holes, thus reducing the oxidative attack on the CdS surface. By effectively trapping the holes, sacrificial agents minimize the potential for CdS to undergo dissolution. This approach has been widely employed to enhance the stability of CdS during photocatalytic hydrogen evolution [356]. Furthermore, anion doping has been explored as another method for improving the stability of CdS under photocatalytic conditions. Doping with elements like nitrogen (N), chlorine (Cl), or phosphorus (P) has been shown to modify the electronic structure of CdS, reducing its tendency for photocorrosion by altering its surface reactivity. Nitrogen-doped CdS has demonstrated enhanced photocatalytic stability, likely due to the suppression of charge recombination and increased protection of the surface against oxidative degradation [357].

Photo-corrosion mechanisms of CdS photocatalysts should therefore be studied in depth for attaining extremely efficient H_2 production capability. Two principal routes for CdS photo-corrosion are as following. Main cause of CdS photocorrosion is the fact that CdS photocatalysts generate pairs of electrons and holes when exposed to visible light. These holes easily oxidize the sulphide ions on CdS surfaces, producing solid sulfur (Eqs. (9) and (10)) (Fig. 11a) [358], which leads to extensive photo-corrosion of the CdS surface. Simultaneously, photo-generated electrons reduce Cd^{2+} to metallic Cd (Eq. (14)) (Fig. 11d). This led to significant damage the CdS nanostructure, which significantly reduced the photocatalytic life-time as well as performance. Consequently, the photocatalytic features of CdS photocatalysts become highly unstable, leading to a reduction in their photocatalytic efficiency [359]. In the existence of O_2, CdS photocorrosion further proceeds (Eq. (11)–(13)).

$$CdS \xrightarrow{h\nu} e^- + h^+ \tag{9}$$

$$CdS + 2h^+ \rightarrow Cd^{2+} + S \tag{10}$$

$$CdS + 4h^+ + 2H_2O + O_2 \rightarrow Cd^{2+} + SO_4^{2-} + 4H^+ \tag{11}$$

$$O_2 + 4e^- + 2H^+ \rightarrow 2OH^- \tag{12}$$

$$CdS + 2O_2 \rightarrow Cd^{2+} + SO_4^{2-} \tag{13}$$

$$Cd^{2+} + 2e^- \rightarrow Cd \tag{14}$$

One widely utilized and useful approach for minimizing CdS photocorrosion and enhancing photo-induced durability is to add Na_2S–Na_2SO_3 mixed solution (S_{2-}/SO_3^{2-}). Utilizing this strategy, photo-generated holes on the CdS surface is expected to rapidly remove through capturing surface holes with S^{2-}/SO_3^{2-} (Fig. 11b). Nevertheless, in the S^{2-}/SO_3^{2-} solution, complete suppression of CdS photocorrosion is not achievable (Fig. 11c). This is predominantly owing to extremely miniscule quantity of adsorbed sulfur ions on surface of CdS. As well plentifull sulfur ions still remain within solution, which unable to efficiently collect photo-excited holes on surface of CdS.It is necessary to denoide CdS surface and to facilitate the separation of charges [180]. Fig. 12 presents stability of CdS-based compounds by inhibiting photocorrosion of CdS in photocatalytic H_2 evolution. Several studies have shown that it is feasible to effectively impede the photo-corrosion of CdS. The researchs on CdS photocorrosion have been mostly concentrated on surface oxidation caused by photo-generated holes, whereas potential reduction of lattice Cd^{2+} by photo-generated electrons has typically been neglected.

Chen et al. [359] conducted a thorough investigation into lattice Cd^{2+} reduction by photo-induced electrons during photo-corrosion of CdS to demonstrate its possible impact on the change in microstructure. They utilized two common Na_2S–Na_2SO_3 and lactic acid in H_2 prodution process. Their findings also demonstrated the potential impact of CdS

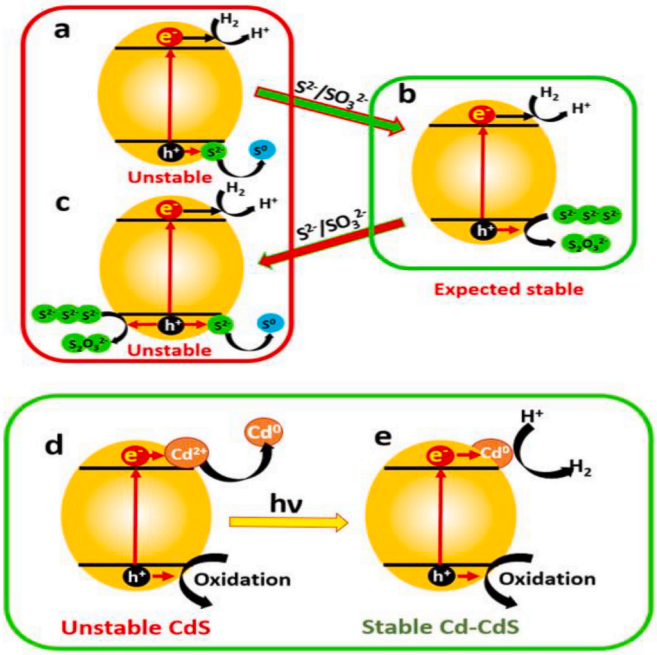

Fig. 11. Photo-corrosion of CdS and photo-induced self-stability strategy of CdS during photocatalysis [359].

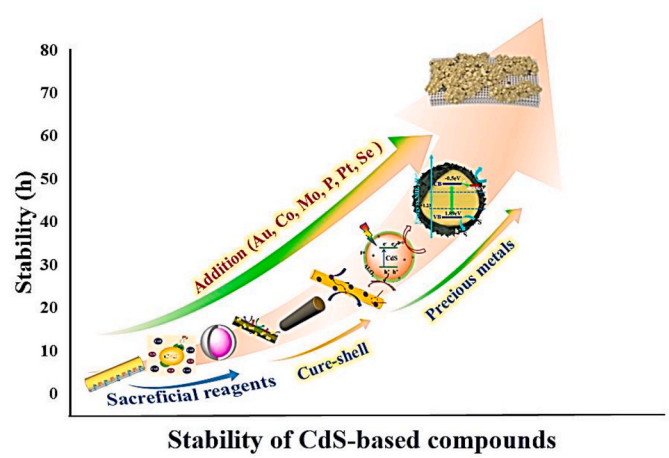

Fig. 12. Stability of CdS-based compounds by inhibiting photo corrosion of CdS in photocatalytic H_2 evolution (ZnO/CdS NWs [247], Au–Co/CdS [117], Ni_2P@CdS [52], $Co_{0.2}Cd_{0.8}S$/g-C_3N_4 [363], ZnO/CdS NRs [361], $MoSe_2$/CdS [367], Pt–Al_2O_3/CdS [362], Zn–C/CdS [90], MoS_2/Ti_3C_2/CdS [366]).

photo-corrosion on the photocatalytic H_2 production efficiency. The produced abundant discrete metallic Cd NPs into Na_2S–Na_2SO_3 system sreiously destroyed the CdS surface and the photocatalytic activity was decreased gradually. As for the lactic acid system, a metallic Cd layer (2–3 nm) is homogeneously covered on CdS particle surface to form the core-shell structure of CdS@Cd, leading to an increased H_2-evolution rate [360].

A mechanism for photo-induced self-durability of CdS photocatalyst are being suggested. According to this process, in addition to realization of the ultimate stable H_2 production performance simultaneously, the unstable CdS was converted into the stable CdS–Cd structure by the spontaneously produced metallic Cd. (Fig. 11e). Several heterojunction, loading of co-catalyst, and core-shell structure have been extensively constructed to successfully increase photocorrosion impedence of CdS [34]. However, it is yet unclear how the CdS photocatalyst occur photocorrosion. To generate CdS photocatalytic materials with high efficiency and stability, more research must be conducted to completely comprehend the photocorrosion mechanisms of CdS in various H_2 production processes. The stability and efficiency of CdS photocatalysts are the two vital factors. The core-shell structure retains durability of CdS. Photo-corrosion of CdS can be suppressed efficiently by growing ZnO shell homogeneously on the core of CdS. Tso et al. [247] prepared the core-shell structured CdS/ZnO NWs photocatalyst. The core-shell CdS/ZnO NWs exhibited significant durability for 4 h in acid solution and improvement in H_2 production performance, which was longer compared to CdS NWs by a factor of 2. As Fig. 12, the core-shell CdS–ZnO NWs showed the lowest stabilty among the photocatalysts. Compared to CdS NWs, the core-shell CdS–ZnO NRs exhibited better durabilty. Recently, Sun et al. [361] prepared the core-shell CdS–ZnO NRs through a facile chemical deposition route. The optimum $CSZ_{0.5}$ heterostructure showed an exceptional highly efficient H_2 yields of 805.5 μmol h^{-1} yielding rate for 3 mg catalyst (equal to 268.5 mmol g^{-1} h^{-1} yielding rate). This H_2 production rate was superior to bare ZnO and pristine CdS by the factors of 895 and 12 correspondingly. The homogeneous grown of ZnO shell on the core of CdS suppressed photo-corrosion of CdS, exhibiting outstanding photo-stability of CdS/ZnO over 18 h. The CdS NPs are efficiently shielded from photocorrosion by the Al2O3 shell on the CdS core surface through swiftly transferring the interfacial photogenerated holes which generate oxygen quickly. Ning et al. [362] prepared the highly active Pt/CdS@Al_2O_3 nanocomposite. The as-prepared Pt/CdS@Al_2O_3 exhibited the average H_2 evolution reached to 0.0621 mmol g^{-1} h^{-1} yielding rate. This rate was almost 126-times larger compared to CdS NPs. Pt NP co-catalyst was capable of effectively separate photo-induced charge-carriers and acted as a reactive site for H_2 production. Artificial gills were utilized in photocatalytic overall water splitting to remove freshly produced O_2 from water for suppressing O_2 driving photo-corrosion as well as obstructing recombination of H_2 and O_2 back to water. It was found that the Pt/CdS@Al_2O_3 still demonstrated a remarkable photocatalytic performance for H_2 evolution with better stability even after 30 h.

The performance and durability of CdS in photocatalytic H_2 generation were significantly increased by covering it with a Zn-anchored carbon layer [90]. The CdS@Zn–C exhibited a maximum H_2 yields of 6.6 mmol g^{-1} h^{-1} rate. This was 4.7-folds larger to that of pristine CdS under irradiation of visible light. AQE of CdS@ZnC was also obtained up tp 13.1% at 420 nm. Furthermore, the as-prepared CdS@Zn–C showed exceptional stability even over 44 h. This boosted photocatalytic performance was ascribed to the utilized carbon layer, which functioned as electron acceptor and prevented recombination of charges. Thorugh anchoring Zn in the carbon layer. The charge-transportation was facilitated and a reactive site was provided for H_2 evolution. Fang et al. [363] fabricated the newly $Co_{0.2}Cd_{0.8}S$/g-C_3N_4 photocatalyst through hydrothermal route. The optimized $Co_{0.2}Cd_{0.8}S$/g-C_3N_4 photocatalyst showed outstanding H_2 yielding with 35.5 mmol g^{-1} h^{-1} upon irradiation in visible range. This rate was 1.85 and 7.85-folds larger compared to pristine $Co_{0.2}Cd_{0.8}S$ and CdS, respectively. This remarkable photocatalytic efficiency was predominantly due to rapid separation of charges owing to formation of $Co_{0.2}Cd_{0.8}S$/g-C_3N_4 heterostructure and raduction of photocorrosion. The optimal $Co_{0.2}Cd_{0.8}S$/g-C_3N_4 exhibited highly durability for 15 h and reusibility for 5-cycles in the H_2 evolution process. This sample showed more photo-corrosion impedence than $Co_{0.2}Cd_{0.8}S$. This efficiency was owing to distinctive structure of $Co_{0.2}Cd_{0.8}S$/g-C_3N_4 having rapid photo-induced electrons transportation feature.

The directly incorporation of cobalt ions in lactic acid to prevent photo-corrosion of CdS photocatalyst during photocatalytic H_2 evolution is a new strategy. The CdS–Co photocatalyst exhibited a remarkable enhancement of photo-corrosion impedence than pristine CdS. Cobalt ions and lactic acid performed a chemical process forming cobalt lactate complex (CoL). Instead of appearing on the surface of CdS, it was exclusively exist in the lactic acid solution [117]. This increased photo-corrosion impedence and H_2 evolution efficiency of CdS were owing to the photo-induced holes of CdS rapidly consuming through reversible redox reactions of cobalt lactate complexes. Metallic Au was added to CdS to produce CdS/Au by employing a photo-deposition technique for facilitating the photocatalytic H_2 production performance. The excellent photo-corrosion impedence with good stability for 8 h was maintained by CdS–Au into CoL system. The CdS/Au–Co sample showed a significant H_2 generation of 86.46 μmol h^{-1} yielding rate. This rate was 10.16 and 2.29-folds greater compared to bare CdS and CdS–Co. accordingly. Separation of charges and inhibition of photo-corrosion was improved by the interfacial engineering as well as utilizing lactic acid. In order to enhance photocatalytic H_2 evolution along with enhance photo-corrosion resistance, intimate CdS/Cd ohmic-junction was developed by sulfur confinement and high content [364]. The optimized CdS/Cd showed a highly H_2 evolution of 95.40 μmol h^{-1}, which was almost 32.3-folds larger to pristine CdS. Further, this obtained photocatalyst showed an outstanding photo-stability, which was much longer compared to the majority CdS photocatalysts. The interfacial ohmic junction facilitated the transportation of photo-induced electrons and developing sulfur-confined architecture for inhibiting oxidation of CdS caused by positive holes.

Inhibiting photocorrosion could boost efficiency and durability of photocatalyst, which can be achieved by regulating defect engineering and developing core-shell architecture. The CdS@$ZnIn_2S_4$-SV (CdS@ZIS-SV) core-shell was developed by Liu et al. [365] by wrapping CdS NRs with ultra thin ZIS NSs bearing plenty of S-vacancies via a hydrothermal route. The highest H_2 production of 18.06 mmol g^{-1} h^{-1} was obtained over this as-prepared CdS@ZIS-SV photocatalysts. This rate was greater than that of bare CdS and ZIS by the factors of 16.9 and 19.6, respectively. Photo-corrosion was prevented by core-shell architecture, which restricted Cd^{2+} and S^{2-} locally around CdS rather than allowing them to quickly diffuse into the solution. The particular surfaces of material was expanded and abundant reactive sites were exposed by employing ultra-thin ZIS NSs, which also improved the capability of materials to trap electrons due to the abundance of S vacancies on the surface. This promoted charges separation, which suppressed the holes from oxidizing S2-. Effective electron-hole pair separation was facilitated by Z-Scheme heterojunction. Wu et al. [366] constructed the CdS@MoS_2/Ti_3C_2 photocatalysts with intimate binding interface through in situ growth process for improving the capability of photo-corrosion impedence. The photo-induced electrons from CdS successfully transferred to the surface of MoS_2 and photo-eccited holes from CdS successfully transferred to Ti_3C_2 surface. The optimized photocatalyst showed the highly H_2 production of 14.88 mmol g^{-1} h^{-1} yielding rate with highly durability. As Fig. 12, CdS@MoS_2/Ti_3C_2 photocatalysts demonstrated the highest stability among other photocatalysts. This enhancement of effiiency and durability of CdS was attributed to the usage of redox dual co-catalysts Ti_3C_2 MXene and MoS_2. During photocatalysis, components and structure of composite remained undamaged. The stabilities and performances of CdS-based heterojunction photo-catalysts during H_2 production by water splitting

are presented in the Table 10.

6. Photoreactor design for H2 production

The architecture and configuration of photoreactors are just as important as the photocatalyst's performance in determining H_2 yield rate. The layout and configuration of irradiation devices, as well as the choice and distribution of light sources should all be considered while developing new photoreactor technologies. The designing approach utilized for integrating photocatalyst into a photo-reactor is an additional aspect that could affect the entire efficiency of photocatalytic reactions.

Solid-phase metal reactor design is crucial for the synthesis of efficient photocatalysts due to its ability to create precisely controlled environments that are essential for producing high-quality photocatalytic materials. The Fig. 13 shows the design of the solid phase reactor for photocatalyst synthesis. The design of the reactor allows for controlled temperature profiles, uniform mixing, and optimal reactant contact, ensuring that the photocatalyst's properties, such as crystal structure, composition, and morphology, are tailored to maximize its photocatalytic efficiency. Furthermore, solid-phase reactors provide a contamination-free environment, preventing impurities from external sources, which is vital for achieving high photocatalytic performance. The ability to scale up these reactors also makes them valuable for large-scale manufacturing, paving the way for the commercialization of efficient photocatalysts used in applications such as solar hydrogen production, pollutant degradation, and renewable energy generation.

Several types of photoreactor designs have been reported for the photocatalytic production of hydrogen, including Liquid-phase flow reactors, Quartz micro-reactors, Water-splitting panel reactors, Flow-mass reactors [212,247,361], as shown in Fig. 14. Each type of photoreactor has its own advantages and disadvantages. For example, liquid-phase flow reactors are simple to design and operate, but they can suffer from low light penetration and poor mixing of the photocatalyst suspension. Quartz micro-reactors can achieve high light utilization and efficient mixing, but they can be difficult to scale up. Water-splitting panel reactors are designed to overcome the challenges of scaling up, but they can be expensive to build. Flow-mass reactors are a relatively new type of photoreactor that has the potential to combine the advantages of the other types of reactors. The optimal design of a photoreactor for photocatalytic hydrogen production will depend on the specific photocatalyst and reaction conditions. However, some general principles can be applied to the design of all types of photoreactors. An elevated proportion of adaptable catalyst's surface area to the reactor's volume is required for an optimal photo-reactor.

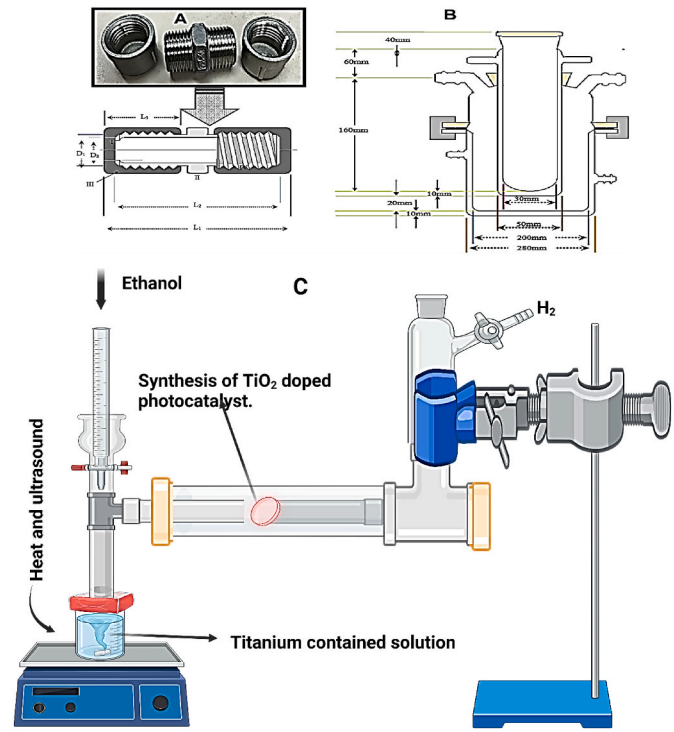

Fig. 13. The design of the solid phase reactor for photocatalyst synthesis.

The critical challenge of achieving high activity of water-splitting photocatalysts under sunlight impedes large-scale deployment. While a panel-type reactor, as introduced by Schro der et al. [379] demonstrated scalable photocatalytic hydrogen evolution, its utilization relied on sacrificial electron donors, leaving the accomplishment of industrial-scale solar light powered photocatalytic water splitting without such reactants an ongoing quest. To bridge this gap, comprehensive research on pilot-scale, genuine solar-leading water splitting systems is imperative. High photonic efficiency is used across the photoreactor, with uniform light distribution, to boost photocatalytic efficiency. In addition to the above principles, other factors to consider in the design of photoreactors for photocatalytic hydrogen production include: the type and intensity of light source, the flow regime of the reactants and products, the temperature and pressure of the reaction, the materials used to construct the reactor. The development of more efficient and scalable photoreactors is a key challenge in the commercialization of photocatalytic hydrogen production. Researchers are actively developing new photoreactor designs and materials to address this challenge.

Table 10
The durability and efficiency of heterojunction photo-catalysts based on CdS in the process of H_2 evolution through water splitting.

Catalysts	Co-catalysts	H_2 evolution rate (mmol g^{-1} h^{-1})	Sabilities (h)	Reference
ZnO/CdS NWs	ZnO	9.618	4	[247]
Au–Co/CdS	Au–Co	1.7292	8	[117]
Ni_2P@CdS	Ni_2P	0.83794	12	[52]
$Co_{0.2}Cd_{0.8}S$/g-C_3N_4	Co/g-C_3N_4	35.5	15	[363]
ZnO/CdS NRs	ZnO	268.5	18	[361]
$MoSe_2$/CdS	$MoSe_2$	11.24	25	[367]
Pt–Al_2O_3/CdS	Pt–Al_2O_3	0.0621	30	[362]
Zn–C/CdS	Zn–C	6.6	44	[90]
MoS_2/Ti_3C_2/CdS	MoS_2/Ti_3C_2	14.88	78	[366]
PANI@CdS	PANI	0.31	30	[368]
CdS/WS_2	WS_2	0.3741	200	[369]
CdS@$W_{18}O_{49}$	$W_{18}O_{49}$	11.732	40	[73]
CdS/MoS_2	MoS_2	14.4	20	[370]
Fe3C/CdS	Fe3C	97.5	22	[371]
CdS/m-TiO_2/G	m-TiO_2/G	9.5	80	[372]
CdS@PDA@SnO_{2-x}	PDA@SnO_{2-x}	82.27	50	[373]
CdS@TiO_2/Ni_2P	TiO_2/Ni_2P	16.81	750	[374]
CdS/$W_{18}O_{49}$	$W_{18}O_{49}$	15.4	24	[56]
WS_2/CdS@ZnCdS	WS_2/ZnCdS	34.86	20	[375]
NiCo-LDH/P–CdS	NiCo-LDH/P	8.665	1\\6	[376]
CdS/Mo-VC	Mo-VC	2.267	24	[377]
Bi–Bi2MoO_6/CdS-DETA	Bi–Bi2MoO_6/DETA	7.37	16	[378]

7. Future perspectives

To address the current challenges in photocatalytic hydrogen (H_2) production, several research directions should be prioritized for the advancement of CdS-based photocatalysts. Fig. 15 illustrates the advancements in the development of CdS-based photocatalysts for H_2 evolution. The low selectivity and efficiency of CdS under solar light should be mitigated by enhancing interfacial interactions between co-catalysts and CdS. Such enhancements should be achieved through strategies including size optimization of photocatalysts, formation of

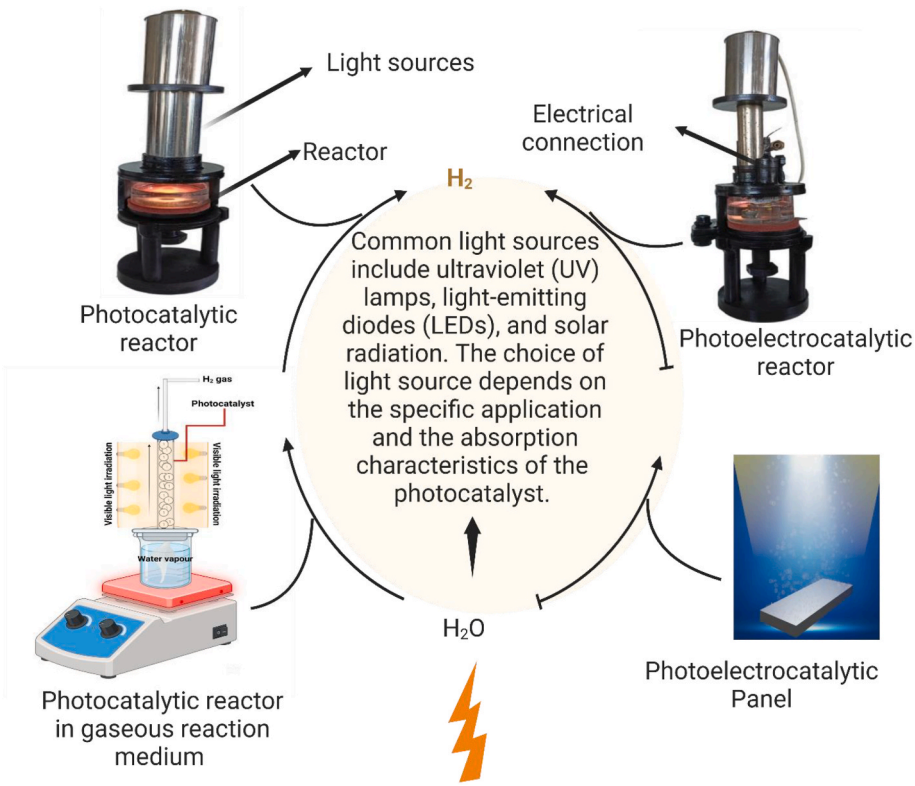

Fig. 14. The different rector designs of the photocatalytic hydrogen production.

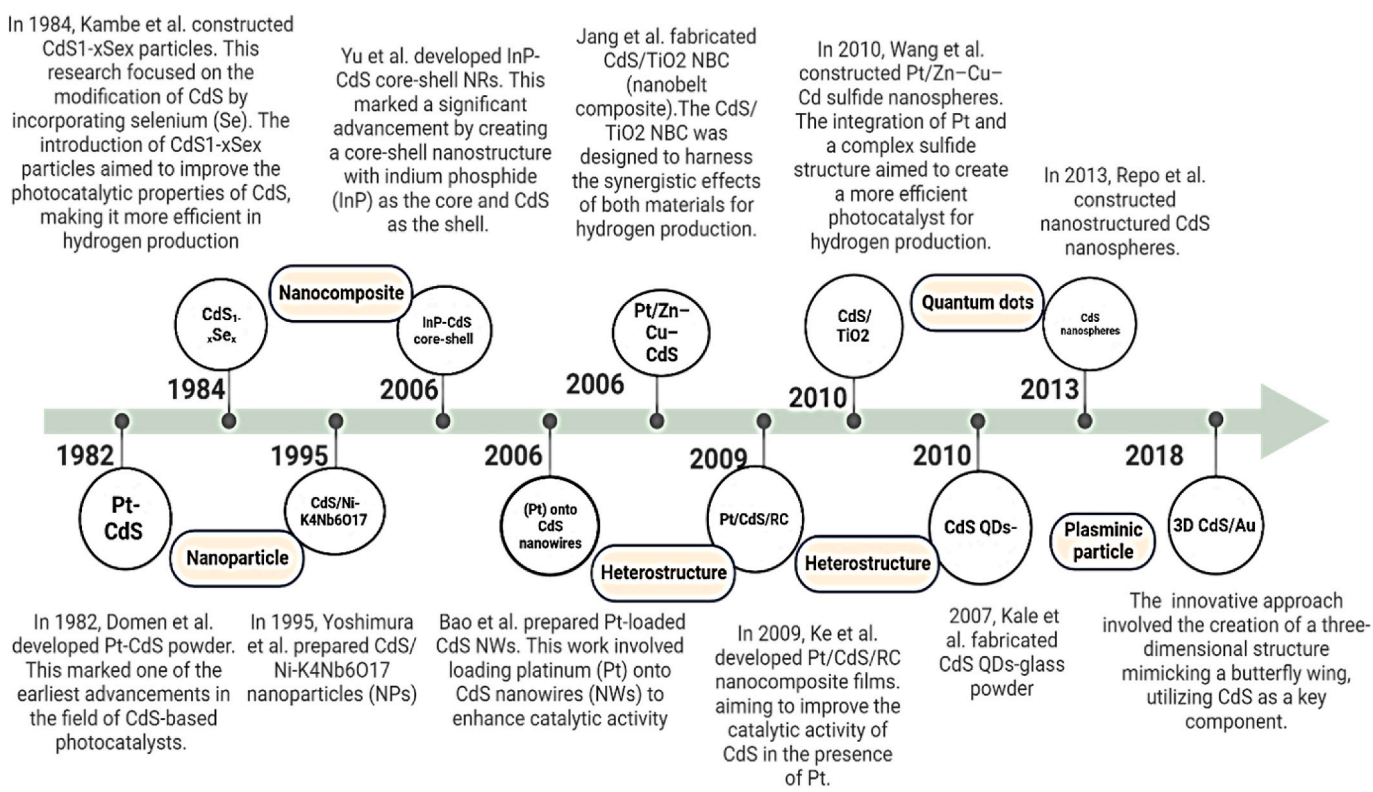

Fig. 15. Schematic diagram of the development of CdS-based photocatalysts for H_2 production (Pt–CdS [380], $CdS_{1-x}Se_x$ [381], $CdS/NiK_4Nb_6O_{17}$ [382], InP/CdS core-shell [383], Pt onto CdS nanowires [384], Pt/Zn–Cu/CdS [385], CdS/TiO_2 NBC [386], Pt/CdS/RC [387], CdS QDs-sensitized $Zn_{1-x}Cd_xS$ solid solution [388], CdS QDs-glass powder [389], CdS nanospheres [390], 3D CdS/Au [391]).

chemical bonds, heat treatments, π-interactions, crystal facet exposure, and the creation of CdS-based heterojunctions. These approaches should be designed to effectively suppress the fast recombination of photo-excited pairs and minimize CdS photocorrosion, both of which currently hinder H_2 evolution performance.

Efforts should also focus on amplifying light scattering and multiple reflections in CdS-based heterojunctions to improve light harvesting and enhance photocatalytic efficiency. Future studies should explore innovative designs of photoreactors and optimize their configurations to ensure financial sustainability and suitability for industrial-scale H_2 production. Overcoming these engineering and economic barriers should be a critical area of focus to transition photocatalysis from laboratory-scale research to industrial application. Achieving sacrificial-agent-free H_2 evolution through overall water splitting should remain a key goal. To realize this, strategies to address the moderately oxidizable nature of CdS and the sluggish oxygen (O_2) evolution process should be developed. Effective separation of gaseous H_2 and O_2 products should also be ensured to improve system stability and safety. Benzaldehyde has shown promise as an alternative to conventional sacrificial agents by facilitating faster H_2 evolution while simultaneously enabling the co-production of industrially valuable products. This dual-functional approach should be further explored for its potential to revolutionize the economic viability of photocatalytic systems.

The fabrication of advanced S-scheme heterojunctions should be emphasized, as they are expected to maintain excellent redox capabilities and enable efficient H_2 production through water splitting. To enhance the performance of these heterostructures, research should focus on optimizing their shape, composition, and co-catalyst loading. A thorough investigation of the thermodynamic and kinetic aspects of H_2 evolution should be conducted to identify pathways for accelerating charge transfer and lowering the activation barrier in photocatalytic reactions.

Incorporation of organic substances such as conductive polymers (e.g., PANI) and biomolecules (e.g., histidine) should be utilized to enhance the overall efficiency of H_2 evolution while simultaneously mitigating CdS photocorrosion. Organic-CdS hybrid systems should be systematically studied to better understand their synergistic effects and optimize their performance for long-term stability and activity. Addressing the multifaceted challenges associated with CdS-based photocatalysts requires a multidisciplinary approach. Future advancements should combine material innovation, reactor design, and economic optimization to pave the way for practical and sustainable photocatalytic H_2 production technologies.

8. Conclusions

Various strategies, including morphology control, doping, co-catalyst loading, and heterojunction formation, have been employed to develop CdS-based heterojunctions for efficient photocatalytic H_2 production. Pt NPs loaded CdS exhibited outstanding H_2 evolution efficiency and high stability. Incorporating organic compounds, such as histidine, with Pt–CdS compounds enhanced overall hydrogen production rates and suppressed photo-corrosion. The inclusion of heteroatoms efficiently enhances photocatalytic activity. CdS nanorods with the deposition of Fe–Co/MoS_2 nanosheets demonstrated superb H_2 production efficiency, primarily due to the synergistic effects of MoS_2 and heteroatom doping. The core-shell CdS/TiN nanowires exhibited excellent H_2 production efficiency, reliability, and chemical stability during photocatalysis. The core-shell nanostructured CdS@MoS_2 displayed excellent H_2 production capability during photocatalysis without the need for precious metals. Other notable heterojunctions include Binary core-shell structured CdS–ZnS nanorods, Ni_2P@CdS–Ni_3 heterojunction, Film-like 2D/2D CdS–Ni_3S_2/NF photocatalyst, $BiVO_4$–CdS photocatalyst, MoS_2/ReS_2@CdS Z-scheme heterojunctions, Organic-inorganic heterojunctions, such as pyrene-alt-triphenylamine (PT) layered on CdS nanocrystals. The strategies discussed above have demonstrated the potential of CdS-based heterojunctions for practical applications in the solar-driven splitting of water. Significant progress has been made in developing CdS-based heterojunctions for efficient photocatalytic H_2 production.

CRediT authorship contribution statement

Aminul Islam: Writing – review & editing, Writing – original draft, Supervision, Project administration, Investigation, Conceptualization. **Abdul Malek:** Writing – original draft, Methodology, Formal analysis. **Md. Tarekul Islam:** Writing – original draft, Software, Resources, Investigation. **Farzana Yeasmin Nipa:** Writing – original draft, Validation, Methodology. **Obayed Raihan:** Writing – original draft, Resources, Investigation. **Hasan Mahmud:** Software, Investigation, Data curation. **Md Elias Uddin:** Resources, Investigation, Conceptualization. **Mohd Lokman Ibrahim:** Resources, Investigation, Conceptualization. **G. Abdulkareem-Alsultan:** Resources, Methodology, Data curation. **Alam Hossain Mondal:** Validation, Formal analysis, Conceptualization. **Md. Munjur Hasan:** Writing – original draft, Validation, Methodology, Formal analysis. **Md. Shad Salman:** Writing – original draft, Software, Resources, Data curation. **Khadiza Tul Kubra:** Writing – original draft, Resources, Investigation, Conceptualization. **Md. Nazmul Hasan:** Writing – original draft, Supervision, Resources, Methodology, Investigation. **Md. Chanmiya Sheikh:** Writing – original draft, Validation, Data curation. **Tetsuya Uchida:** Writing – original draft, Supervision, Resources. **Adiba Islam Rasee:** Writing – original draft, Resources, Investigation. **Ariyan Islam Rehan:** Writing – original draft, Software, Investigation, Data curation. **Eti Awual:** Writing – original draft, Resources, Investigation, Conceptualization. **Mohammed Sohrab Hossain:** Writing – original draft, Software, Resources, Methodology, Data curation. **R.M. Waliullah:** Writing – original draft, Validation, Formal analysis, Conceptualization. **Md. Rabiul Awual:** Writing – review & editing, Writing – original draft, Supervision, Funding acquisition, Conceptualization.

Declaration of competing interest

The authors declare that they have no known competing financial interests or personal relationships that could have appeared to influence the work reported in this paper.

Acknowledgment

The work was supported by the Bangladesh Energy and Power Research Council (BEPRC). This work was conducted at the Hydrogen Energy and CO_2 Conversion Lab, Department of Petroleum and Mining Engineering, Jashore University of Science and Technology, Jashore-7408, Bangladesh.

References

[1] Le TT, Sharma P, Bora BJ, Tran VD, Truong TH, Le HC, Nguyen PQ. Fueling the future: a comprehensive review of hydrogen energy systems and their challenges. Int J Hydrogen Energy 2024;54:791–816.
[2] Dincer I, Acar C. Review and evaluation of hydrogen production methods for better sustainability. Int J Hydrogen Energy 2015;40(34):11094–111.
[3] Wang B, Mi Z, Nistor I, Yuan XC. How does hydrogen-based renewable energy change with economic development? Empirical evidence from 32 countries. Int J Hydrogen Energy 2018;43(25):11629–38.
[4] Ren J, Manzardo A, Toniolo S, Scipioni A. Sustainability of hydrogen supply chain. Part I: identification of critical criteria and cause–effect analysis for enhancing the sustainability using DEMATEL. Int J Hydrogen Energy 2013;38(33):14159–71.
[5] Xu X, Feng X, Wang W, Song K, Ma D, Zhou Y, Shi JW. Construction of II-type and Z-scheme binding structure in P-doped graphitic carbon nitride loaded with ZnO and ZnTCPP boosting photocatalytic hydrogen evolution. J Colloid Interface Sci 2023;651:669–77.
[6] Kumar R, Kumar A, Pal A. Overview of hydrogen production from biogas reforming: Technological advancement. Int J Hydrogen Energy 2022;47(82):34831–55.

[7] Steinberg M, Cheng HC. Modern and prospective technologies for hydrogen production from fossil fuels. Int J Hydrogen Energy 1989;14(11):797–820.
[8] Abas N, Kalair E, Kalair A, ul Hasan Q, Khan N. Nature inspired artificial photosynthesis technologies for hydrogen production: barriers and challenges. Int J Hydrogen Energy 2020;45(41):20787–99.
[9] Shanmughan B, Nighojkar A, Kandasubramanian B. Exploring the future of 2D catalysts for clean and sustainable hydrogen production. Int J Hydrogen Energy 2023;48(74):28679–93.
[10] Shan Z, Yang Y, Shi H, Zhu J, Tan X, Luan Y, Jiang Z, Wang P, Qin J. Hollow dodecahedra graphene oxide-cuprous oxide nanocomposites with effective photocatalytic and bactericidal activity. Front Chem 2021;9:755836.
[11] Bakbolat B, Daulbayev C, Sultanov F, Beissenov R, Umirzakov A, Mereke A, Bekbaev A, Chuprakov I. Recent developments of TiO2-based photocatalysis in the hydrogen evolution and photodegradation: a review. Nanomaterials 2020;10(9):1790.
[12] Burton NA, Padilla RV, Rose A, Habibullah H. Increasing the efficiency of hydrogen production from solar powered water electrolysis. Renewable Sustainable Energy Rev 2021;135:110255.
[13] Liu W, Huang F, Liao Y, Zhang J, Ren G, Zhuang Z, Zhen J, Lin Z, Wang C. Treatment of CrVI-containing Mg (OH) 2 nanowaste. Angew Chem 2008;120(30):5701–4.
[14] Khedr TM, Wang K, Kowalski D, El-Sheikh SM, Abdeldayem HM, Ohtani B, Kowalska E. Bi2WO6-based Z-scheme photocatalysts: principles, mechanisms and photocatalytic applications. J Environ Chem Eng 2022;10(3):107838.
[15] Hunge YM, Yadav AA, Kang SW, Lim SJ, Kim H. Visible light activated MoS2/ZnO composites for photocatalytic degradation of ciprofloxacin antibiotic and hydrogen production. J Photochem Photobiol 2023;434:114250.
[16] Xu F, Hu C, Zhu D, Wang D, Zhong Y, Tang C, Zhou H. One-step hydrothermal synthesis of nanostructured MgBi2O6/TiO2 composites for enhanced hydrogen production. Nanomaterials 2022;12(8):1302.
[17] Muscetta M, Al Jitan S, Palmisano G, Andreozzi R, Marotta R, Cimino S, Di Somma I. Visible light–driven photocatalytic hydrogen production using Cu2O/TiO2 composites prepared by facile mechanochemical synthesis. J Environ Chem Eng 2022;10(3):107735.
[18] Xie Z, Chen J, Chen Y, Wang T, Jiang X, Xie Y, Lu CZ. A Z-scheme Pd modified ZnIn2S4/P25 heterojunction for enhanced photocatalytic hydrogen evolution. Appl Surf Sci 2022;579:152003.
[19] Liu Y, Zheng X, Yang Y, Li J, Liu W, Shen Y, Tian X. Photocatalytic hydrogen evolution using ternary-metal-sulfide/TiO2 heterojunction photocatalysts. ChemCatChem 2022;14(5):e202101439.
[20] Liu Y, Zheng X, Yang Y, Song Y, Yang Y, Li J, Shim CM, Shen Y, Tian X. Recent advances in the hydrogen evolution reaction of ZnxCd1− xS-based photocatalysts. Sol RRL 2022;6(4):2101061.
[21] Wang X, Wu K, Cao W, Rui K, Wang W, Zhu R, Zhu J, Yan Z. Z-Scheme strategy in polymeric graphitic C3N5/CdS core–shell heterojunction drives long-lived carriers separation for robust visible-light hydrogen production. Adv Mater Interfac 2023;10(5):2201627.
[22] Shahid MU, Najam T, Helal MH, Hossain I, El-Bahy SM, El-Bahy ZM, ur Rehman A, Shah SS, Nazir MA. Transition metal chalcogenides and phosphides for photocatalytic H2 generation via water splitting: a critical review. Int J Hydrogen Energy 2024;62:1113–38.
[23] Tahir M, Tasleem S, Tahir B. Recent development in band engineering of binary semiconductor materials for solar driven photocatalytic hydrogen production. Int J Hydrogen Energy 2020;45(32):15985–6038.
[24] Shen S, Chu Y, Xu Y, Liu X, Xiu H, Li J, Tang Z, Xu J, Xiao S. Cu doping induced synergistic effect of S-vacancies and S-scheme Cu: Mn0. 5Cd0. 5S@ CuS heterojunction for enhanced H2 evolution from photocatalytic seawater splitting. Int J Hydrogen Energy 2024;61:734–42.
[25] Khan H. Graphene based semiconductor oxide photocatalysts for photocatalytic hydrogen (H2) production, a review. Int J Hydrogen Energy 2024;84:356–71.
[26] Liu M, Wang L, Lu GM, Yao X, Guo L. Twins in Cd 1− x Zn x S solid solution: highly efficient photocatalyst for hydrogen generation from water. Energy Environ Sci 2011;4:1372–8.
[27] Alhebshi A, Sharaf Aldeen E, Mim RS, Tahir B, Tahir M. Recent advances in constructing heterojunctions of binary semiconductor photocatalysts for visible light responsive CO2 reduction to energy efficient fuels: a review. Int J Energy Res 2022;46(5):5523–84.
[28] Kafadi AD, Hafeez HY, Mohammed J, Ndikilar CE, Suleiman AB, Isah AT. A recent prospective and progress on MXene-based photocatalysts for efficient solar fuel (hydrogen) generation via photocatalytic water-splitting. Int J Hydrogen Energy 2024;53:1242–58.
[29] Huang L, Ai L, Wang M, Jiang J, Wang S. Hierarchical MoS2 nanosheets integrated Ti3C2 MXenes for electrocatalytic hydrogen evolution. Int J Hydrogen Energy 2019;44(2):965–76.
[30] Fattah-alhosseini A, Sangarimotlagh Z, Karbasi M. Latest progress in photocatalytic hydrogen production using MXene (Ti3C2)/MOFs composite: a review. Int J Hydrogen Energy 2024;79:771–90.
[31] Sharma K, Hasija V, Malhotra M, Verma PK, Khan AA, Thakur S, Van Le Q, Quang HH, Nguyen VH, Singh P, Raizada P. A review of CdS-based S-scheme for photocatalytic water splitting: synthetic strategy and identification techniques. Int J Hydrogen Energy 2024;52:804–18.
[32] Li X, Gao Y, Li N, Ge L. In-situ constructing cobalt incorporated nitrogen-doped carbon/CdS heterojunction with efficient interfacial charge transfer for photocatalytic hydrogen evolution. Int J Hydrogen Energy 2022;47(65):27961–72.
[33] Shi N, Li X, Fan T, Zhou H, Zhang D, Zhu H. Artificial chloroplast: Au/chloroplast-morph-TiO2 with fast electron transfer and enhanced photocatalytic activity. Int J Hydrogen Energy 2014;39(11):5617–24.
[34] Clarizia L, Spasiano D, Di Somma I, Marotta R, Andreozzi R, Dionysiou DD. Copper modified-TiO2 catalysts for hydrogen generation through photoreforming of organics. A short review. Int J Hydrogen Energy 2014;39(30):16812–31.
[35] Abe R. Recent progress on photocatalytic and photoelectrochemical water splitting under visible light irradiation. J Photochem Photobiol, C 2010;11(4):179–209.
[36] Tahir M, Amin NS. Advances in visible light responsive titanium oxide-based photocatalysts for CO2 conversion to hydrocarbon fuels. Energy Convers Manag 2013;76:194–214.
[37] Grewe T, Meggouh M, Tueysuez H. Nanocatalysts for solar water splitting and a perspective on hydrogen economy. Chem Asian J 2016;11(1):22–42.
[38] Du C, Yan B, Yang G. Self-integrated effects of 2D ZnIn2S4 and amorphous Mo2C nanoparticles composite for promoting solar hydrogen generation. Nano Energy 2020;76:105031.
[39] Gupta NM. Factors affecting the efficiency of a water splitting photocatalyst: a perspective. Renewable Sustainable Energy Rev 2017;71:585–601.
[40] Acar C, Dincer I, Zamfirescu C. A review on selected heterogeneous photocatalysts for hydrogen production. Int J Energy Res 2014;38(15):1903–20.
[41] Colón G. Towards the hydrogen production by photocatalysis. Appl Catal, A 2016;518:48–59.
[42] Navarro Yerga RM, Álvarez Galván MC, Del Valle F, Villoria de la Mano JA, Fierro JL. Water splitting on semiconductor catalysts under visible-light irradiation. ChemSusChem: Chem Sustain Energy Mater 2009;2(6):471–85.
[43] Su T, Shao Q, Qin Z, Guo Z, Wu Z. Role of interfaces in two-dimensional photocatalyst for water splitting. ACS Catal 2018;8(3):2253–76.
[44] Li X, Yu J, Low J, Fang Y, Xiao J, Chen X. Engineering heterogeneous semiconductors for solar water splitting. J Mater Chem A 2015;3(6):2485–534.
[45] Low J, Yu J, Jaroniec M, Wageh S, Al-Ghamdi AA. Heterojunction photocatalysts. Adv Mater 2017;29(20):1601694.
[46] Yuan YJ, Chen D, Yu ZT, Zou ZG. Cadmium sulfide-based nanomaterials for photocatalytic hydrogen production. J Mater Chem A 2018;6(25):11606–30.
[47] Liu X, Fan B, Wang Z, Guo Z, Tang B, Lv S, Xing A, Zhang J, Cheng X, Xie H. Dynamic internal field engineering in BaTiO3-TiO2 nanostructures for photocatalytic dye degradation. ACS Appl Nano Mater 2021;4(4):3742–9.
[48] Tong H, Umezawa N, Ye J, Ohno T. Electronic coupling assembly of semiconductor nanocrystals: self-narrowed band gap to promise solar energy utilization. Energy Environ Sci 2011;4(5):1684–9.
[49] Zhang G, Monllor-Satoca D, Choi W. Band energy levels and compositions of CdS-based solid solution and their relation with photocatalytic activities. Catal Sci Technol 2013;3(7):1790.
[50] Lang D, Xiang Q, Qiu G, Feng X, Liu F. Effects of crystalline phase and morphology on the visible light photocatalytic H 2-production activity of CdS nanocrystals. Dalton Trans 2014;43(19):7245–53.
[51] Zhang X, Liu T, Zhao F, Zhang N, Wang Y. In-situ-formed Cd and Ag2S decorated CdS photocatalyst with boosted charge carrier spatial separation for enhancing UV-vis-NIR photocatalytic hydrogen evolution. Appl Catal, B 2021;298:120620.
[52] Zhen W, Ning X, Yang B, Wu Y, Li Z, Lu G. The enhancement of CdS photocatalytic activity for water splitting via anti-photocorrosion by coating Ni2P shell and removing nascent formed oxygen with artificial gill. Appl Catal, B 2018;221:243–57.
[53] Mao L, Ba Q, Jia X, Liu S, Liu H, Zhang J, Li X, Chen W. Ultrathin Ni (OH) 2 nanosheets: a new strategy for cocatalyst design on CdS surfaces for photocatalytic hydrogen generation. RSC Adv 2019;9(3):1260–9.
[54] Shen R, Lu X, Zheng Q, Chen Q, Ng YH, Zhang P, Li X. Tracking S-scheme charge transfer pathways in Mo2C/CdS H2-evolution photocatalysts. Sol RRL 2021;5(7):2100177.
[55] Quan Y, Wang G, Jin Z. Tactfully assembled CuMOF/CdS S-scheme heterojunction for high-performance photocatalytic H2 evolution under visible light. ACS Appl Energy Mater 2021;4(8):8550–62.
[56] Xiong Y, Liu T, Wang X, Liu W, Xue Y, Zhang X, Xiong C, Tian J. S-scheme heterostructure based on ultrathin 2D CdS coated W18O49 nanosheets-assembled network for highly-efficient photocatalytic H2 evolution. J Alloys Compd 2022;918:165652.
[57] Ge H, Xu F, Cheng B, Yu J, Ho W. S-scheme heterojunction TiO2/CdS nanocomposite nanofiber as H2-production photocatalyst. ChemCatChem 2019;11(24):6301–9.
[58] Cheng C, Wang X, Lin Y, He L, Jiang JX, Xu Y, Wang F. The effect of molecular structure and fluorination on the properties of pyrene-benzothiadiazole-based conjugated polymers for visible-light-driven hydrogen evolution. Polym Chem 2018;9(35):4468–75.
[59] Ren D, Zhang W, Ding Y, Shen R, Jiang Z, Lu X, Li X. In situ fabrication of robust cocatalyst-free CdS/g-C3N4 2D–2D step-scheme heterojunctions for highly active H2 evolution. Sol RRL 2020;4(8):1900423.
[60] Bai J, Chen W, Shen R, Jiang Z, Zhang P, Liu W, Li X. Regulating interfacial morphology and charge-carrier utilization of Ti3C2 modified all-sulfide CdS/ZnIn2S4 S-scheme heterojunctions for effective photocatalytic H2 evolution. J Mater Sci Technol 2022;112:85–95.
[61] Bai J, Shen R, Jiang Z, Zhang P, Li Y, Li X. Integration of 2D layered CdS/WO3 S-scheme heterojunctions and metallic Ti3C2 MXene-based Ohmic junctions for effective photocatalytic H2 generation. Chin J Catal 2022;43(2):359–69.
[62] Chen Y, Wang Z, Zhang Y, Wei P, Xu W, Wang H, Yu H, Jia J, Zhang K, Peng C. S-scheme and Schottky junction synchronous regulation boost hierarchical CdS@

Nb2O5/Nb2C T x (MXene) heterojunction for photocatalytic H2 production. ACS Appl Mater Interfaces 2023;15(16):20027–39.
[63] Wu J, Sun B, Wang H, Li Y, Zuo Y, Wang W, Lin H, Li S, Wang L. Efficient spatial charge separation in unique 2D tandem heterojunction Cd x Zn 1− x in 2 S 4–CdS–MoS 2 rendering highly-promoted visible-light-induced H 2 generation. J Mater Chem A 2021;9(1):482–91.
[64] Hu T, Dai K, Zhang J, Chen S. Noble-metal-free Ni2P modified step-scheme SnNb2O6/CdS-diethylenetriamine for photocatalytic hydrogen production under broadband light irradiation. Appl Catal, B 2020;269:118844.
[65] Yang M, Wang K, Jin Z. Pyramidal CdS polyhedron modified with NiAl LDH to form S-scheme heterojunction for efficient photocatalytic hydrogen evolution. ChemCatChem 2021;13(15):3525–35.
[66] Ma W, Zheng D, Xian Y, Hu X, Zhang Q, Wang S, Cheng C, Liu J, Wang P. Efficient hydrogen evolution under visible light by bimetallic phosphide NiCoP combined with g-C3N4/CdS S-scheme heterojunction. ChemCatChem 2021;13(20): 4403–10.
[67] Wang B, Chen C, Jiang Y, Ni P, Zhang C, Yang Y, Lu Y, Liu P. Rational designing 0D/1D Z-scheme heterojunction on CdS nanorods for efficient visible-light-driven photocatalytic H2 evolution. Chem Eng J 2021;412:128690.
[68] Wang S, Zhu B, Liu M, Zhang L, Yu J, Zhou M. Direct Z-scheme ZnO/CdS hierarchical photocatalyst for enhanced photocatalytic H2-production activity. Appl Catal, B 2019;243:19–26.
[69] Zhang Y, Jin Z, Yan X, Wang H, Wang G. Effect of Ni (OH) 2 on CdS@ gC 3 N 4 composite for efficient photocatalytic hydrogen production. Catal Lett 2019;149: 1174–85.
[70] Qiu S, Guo R, Wang Q, Yang F, Han Y, Peng X, Yuan H, Wang X. CdS nanoflakes decorated by Ni (OH) 2 nanoparticles for enhanced photocatalytic hydrogen production. Int J Energy Res 2021;45(10):14985–94.
[71] Wang J, Wang Z, Zhu Z. Synergetic effect of Ni (OH) 2 cocatalyst and CNT for high hydrogen generation on CdS quantum dot sensitized TiO2 photocatalyst. Appl Catal, B 2017;204:577–83.
[72] Zulfiqar S, Liu S, Rahman N, Tang H, Shah S, Yu XH, Liu QQ. Construction of S-scheme MnO 2@ CdS heterojunction with core–shell structure as H 2-production photocatalyst. Rare Met 2021;40:2381–91.
[73] Yang Y, Qiu M, Chen F, Qi Q, Yan G, Liu L, Liu Y. Charge-transfer-mediated photocatalysis of W18O49@ CdS nanotubes to boost photocatalytic hydrogen production. Appl Surf Sci 2021;541:148415.
[74] Zhang H, Dong Y, Li D, Wang G, Leng Y, Zhang P, Miao H, Wu X, Jiang P, Zhu Y. Photochemical synthesis of Ni-Ni (OH) 2 synergistic cocatalysts hybridized with CdS nanorods for efficient photocatalytic hydrogen evolution. FlatChem 2021;26: 100232.
[75] Lv Z, Li W, Cheng X, Liu B, Guo Z, Zhuang T, Zhang C. Constructing internal electric field in CdS via Bi, Ni co-doping strategy for enhanced visible-light H2 production. Appl Surf Sci 2021;556:149758.
[76] Ba Q, Jia X, Huang L, Li X, Chen W, Mao L. Alloyed PdNi hollow nanoparticles as cocatalyst of CdS for improved photocatalytic activity toward hydrogen production. Int J Hydrogen Energy 2019;44(12):5872–80.
[77] Banerjee R, Pal A, Ghosh D, Ghosh AB, Nandi M, Biswas P. Improved photocurrent response, photostability and photocatalytic hydrogen generation ability of CdS nanoparticles in presence of mesoporous carbon. Mater Res Bull 2021;134:111085.
[78] Yang F, Liu D, Li Y, Ning S, Cheng L, Ye J. Solid-state synthesis of ultra-small freestanding amorphous MoP quantum dots for highly efficient photocatalytic H2 production. Chem Eng J 2021;406:126838.
[79] Liang Z, Yang C, Lu J, Dong X. Ultrathin Fe2P nanosheet co-catalyst CdS nanorod: the promising photocatalyst with ultrahigh photocatalytic H2 production activity. Appl Surf Sci 2021;566:150732.
[80] Wei RB, Huang ZL, Gu GH, Wang Z, Zeng L, Chen Y, Liu ZQ. Dual-cocatalysts decorated rimous CdS spheres advancing highly-efficient visible-light photocatalytic hydrogen production. Appl Catal, B 2018;231:101–7.
[81] Zhao Y, Lu Y, Chen L, Wei X, Zhu J, Zheng Y. Redox dual-cocatalyst-modified CdS double-heterojunction photocatalysts for efficient hydrogen production. ACS Appl Mater Interfaces 2020;12(41):46073–83.
[82] Gogoi D, Koyani R, Golder AK, Peela NR. Enhanced photocatalytic hydrogen evolution using green carbon quantum dots modified 1-D CdS nanowires under visible light irradiation. Sol Energy 2020;208:966–77.
[83] Sun G, Xiao B, Shi JW, Mao S, He C, Ma D, Cheng Y. Hydrogen spillover effect induced by ascorbic cid in CdS/NiO core-shell pn heterojunction for significantly enhanced photocatalytic H2 evolution. J Colloid Interface Sci 2021;596:215–24.
[84] Lin Y, Pan D, Luo H. Hollow direct Z−Scheme CdS/BiVO4 composite with boosted photocatalytic performance for RhB degradation and hydrogen production. Mater Sci Semicond Process 2021;121:105453.
[85] Yue Q, Wan Y, Sun Z, Wu X, Yuan Y, Du P. MoP is a novel, noble-metal-free cocatalyst for enhanced photocatalytic hydrogen production from water under visible light. J Mater Chem A 2015;3(33):16941–7.
[86] Ni N, Qie B, Du S, Sang Z, Wang Q, Meng C, Tong Y. A novel all-solid-state S-scheme in CdS/ZnTHPP binary nanosystem for hydrogen evolution. Int J Hydrogen Energy 2022;47(26):13044–53.
[87] Li Z, Huang W, Liu J, Lv K, Li Q. Embedding CdS@ Au into ultrathin Ti3–x C2T y to build dual Schottky barriers for photocatalytic H2 production. ACS Catal 2021; 11(14):8510–20.
[88] Li J, Wang H, Gao Y, Fang H, Chen P, Huang F. Ultrathin CdS@ BDC nanosheets derived from 2D metal–organic frameworks for enhanced photoinduced-stability and photocatalytic hydrogen production. Mater Adv 2022;3(23):8579–87.
[89] Chao Y, Zheng J, Zhang H, Ma Y, Li F, Tan Y, Zhu Z. Constructing film photocatalyst with abundant interfaces between CdS and Ni3S2 nanosheets for efficient photocatalytic hydrogen production. Energy Technol 2018;6(11): 2132–8.
[90] Shi Y, Lei X, Xia L, Wu Q, Yao W. Enhanced photocatalytic hydrogen production activity of CdS coated with Zn-anchored carbon layer. Chem Eng J 2020;393: 124751.
[91] Tao J, Yang T, Liu Q, Hu J, Tang H. Designing 0D/2D CdS nanoparticles/g-C3N4 nanosheets heterojunction as efficient photocatalyst for improved H2-evolution. Surface Interfac 2021;26:101312.
[92] Chen L, Xie X, Su T, Ji H, Qin Z. Co3O4/CdS pn heterojunction for enhancing photocatalytic hydrogen production: Co-S bond as a bridge for electron transfer. Appl Surf Sci 2021;567:150849.
[93] Zhang Y, Ran L, Li Z, Zhai P, Zhang B, Fan Z, Wang C, Zhang X, Hou J, Sun L. Simultaneously efficient solar light harvesting and charge transfer of hollow octahedral Cu2S/CdS p–n heterostructures for remarkable photocatalytic hydrogen generation. Trans Tianjin Univ 2021;27(4):348–57.
[94] Yu K, Huang HB, Wang JT, Liu GF, Zhong Z, Li YF, Cao HL, Lue J, Cao R. Engineering cation defect-mediated Z-scheme photocatalysts for a highly efficient and stable photocatalytic hydrogen production. J Mater Chem A 2021;9(12): 7759–66.
[95] Rao VN, Sairam PK, Kim MD, Rezakazemi M, Aminabhavi TM, Ahn CW, Yang JM. CdS/TiO2 nano hybrid heterostructured materials for superior hydrogen production and gas sensor applications. J Environ Manag 2023 Aug;340:117895.
[96] Li W, Fang K, Zhang Y, Chen Z, Wang L, Bu Y. Fabrication of 1D/2D CdS/CoSx direct Z-scheme photocatalyst with enhanced photocatalytic hydrogen evolution performance. Int J Hydrogen Energy 2021;46(14):9351–9.
[97] Wang J, Yu L, Wang Z, Wei W, Wang K, Wei X. Constructing 0D/2D Z-scheme heterojunction of CdS/gC 3 N 4 with enhanced photocatalytic activity for H 2 evolution. Atal. Lett 2021;1:1–2.
[98] Gao Q, Cui Y, Zhang H, Wang S, Liu B, Liu C. Construction of Z–scheme 1D CdS nanorods/2D ultrathin CeO2 nanosheets toward enhanced photodegradation and hydrogen evolution. Sep Purif Technol 2021;274:119116.
[99] Yang Y, Chen J, Liu C, Sun Z, Qiu M, Yan G, Gao F. Dual-Z-scheme heterojunction for facilitating spacial charge transport toward ultra-efficient photocatalytic H2 production. Sol RRL 2021;5(8):2100241.
[100] Zhang T, Meng F, Cheng Y, Dewangan N, Ho GW, Kawi S. Z-scheme transition metal bridge of Co9S8/Cd/CdS tubular heterostructure for enhanced photocatalytic hydrogen evolution. Appl Catal, B 2021;286:119853.
[101] Zhang X, Chen Z, Luo Y, Han X, Jiang Q, Zhou T, Yang H, Hu J. Construction of NH2-MIL-125 (Ti)/CdS Z-scheme heterojunction for efficient photocatalytic H2 evolution. J Hazard Mater 2021;405:124128.
[102] Wang Z, Wang Z, Zhu X, Ai C, Zeng Y, Shi W, Zhang X, Zhang H, Si H, Li J, Wang CZ. Photodepositing CdS on the active cyano groups decorated g-C3N4 in Z-scheme manner promotes visible-light-driven hydrogen evolution. Small 2021;17 (39):2102699.
[103] Jia Y, Wang Z, Qiao XQ, Huang L, Gan S, Hou D, Zhao J, Sun C, Li DS. A synergistic effect between S-scheme heterojunction and Noble-metal free cocatalyst to promote the hydrogen evolution of ZnO/CdS/MoS2 photocatalyst. Chem Eng J 2021;424:130368.
[104] Li Z, Ma T, Zhang X, Wang Z. In2Se3/CdS nanocomposites as high efficiency photocatalysts for hydrogen production under visible light irradiation. Int J Hydrogen Energy 2021;46(29):15539–49.
[105] Huang J, Wang M, Zhang X, Tao J, Lu L, Qiao G, Liu G. Anchoring of 2D CdS on Nb2CTX MXene nanosheets for boosting photocatalytic H2 evolution. J Alloys Compd 2022;923:166256.
[106] Zhang Y, Jin Z, Yuan H, Wang G, Ma B. Well-regulated nickel nanoparticles functional modified ZIF-67 (Co) derived Co3O4/CdS pn heterojunction for efficient photocatalytic hydrogen evolution. Appl Surf Sci 2018;462:213–25.
[107] Zou Y, Guo C, Cao X, Zhang L, Chen T, Guo C, Wang J. Synthesis of CdS/CoP hollow nanocages with improved photocatalytic water splitting performance for hydrogen evolution. J Environ Chem Eng 2021;9(6):106270.
[108] Liu X, Bie C, He B, Zhu B, Zhang L, Cheng B. 0D/2D NiS/CdS nanocomposite heterojunction photocatalyst with enhanced photocatalytic H2 evolution activity. Appl Surf Sci 2021;554:149622.
[109] Liu H, Yan T, Jin Z, Ma Q. CoP nanoparticles as cocatalyst modified the CdS/ NiWO 4 p–n heterojunction to produce hydrogen efficiently. New J Chem 2020; 44(4):1426–38.
[110] He B, Bie C, Fei X, Cheng B, Yu J, Ho W, Al-Ghamdi AA, Wageh S. Enhancement in the photocatalytic H2 production activity of CdS NRs by Ag2S and NiS dual cocatalysts. Appl Catal, B 2021;288:119994.
[111] Chen T, Yang C, Rajendran S, Sawangphruk M, Zhang X, Qin J. Utilizing the built-in electric field of pn heterojunction to spatially separate the photogenerated charges in C, N co-doped Co3O4/CdS photocatalysts. Fuel 2023;331:125594.
[112] Deng L, Fang N, Wu S, Shu S, Chu Y, Guo J, Cen W. Uniform H-CdS@ NiCoP core–shell nanosphere for highly efficient visible-light-driven photocatalytic H2 evolution. J Colloid Interface Sci 2022;608:2730–9.
[113] Tan BY, Song XJ, Xian-yang S. In situ deposition of CdS on MoS2/rGO-based nanocomposites for highly efficient photocatalytic H2 evolution reaction with visible light. J Chem Technol Biotechnol 2021;96(8):2390–9.
[114] Dai K, Hu T, Zhang J, Lu L. Carbon nanotube exfoliated porous reduced graphene oxide/CdS-diethylenetriamine heterojunction for efficient photocatalytic H2 production. Appl Surf Sci 2020;512:144783.
[115] Shen L, Luo M, Liu Y, Liang R, Jing F, Wu L. Noble-metal-free MoS2 co-catalyst decorated UiO-66/CdS hybrids for efficient photocatalytic H2 production. Appl Catal, B 2015;166:445–53.
[116] Meng S, Cui Y, Wang H, Zheng X, Fu X, Chen S. Noble metal-free 0D–1D NiS x/ CdS nanocomposites toward highly efficient photocatalytic contamination

removal and hydrogen evolution under visible light. Dalton Trans 2018;47(36): 12671–83.
[117] Yi X, Li H, Wang P, Fan J, Yu H. Boosting antiphotocorrosion and hydrogen-production activity of cadmium sulfide by cobalt lactate complex. Appl Surf Sci 2020;512:144786.
[118] Zubair M, Svenum IH, Rønning M, Yang J. Core-shell nanostructures of graphene-wrapped CdS nanoparticles and TiO2 (CdS@ G@ TiO2): the role of graphene in enhanced photocatalytic H2 generation. Catalysts 2020 Mar 25;10(4):358.
[119] Zulfiqar S, Liu S, Rahman N, Tang H, Shah S, Yu XH, Liu QQ. Construction of S-scheme MnO 2@ CdS heterojunction with core–shell structure as H 2-production photocatalyst. Rare Met 2021;40:2381–91.
[120] Moniruddin MD, Oppong E, Stewart D, McCleese C, Roy A, Warzywoda J, Nuraje N. Designing CdS-based ternary heterostructures consisting of Co-metal and CoO x cocatalysts for photocatalytic H2 evolution under visible light. Inorg Chem 2019;58(18):12325–33.
[121] Mao S, Zou Y, Sun G, Zeng L, Wang Z, Ma D, Guo Y, Cheng Y, Wang C, Shi JW. Thio linkage between CdS quantum dots and UiO-66-type MOFs as an effective transfer bridge of charge carriers boosting visible-light-driven photocatalytic hydrogen production. J Colloid Interface Sci 2021;581:1. 0.
[122] Yousaf AB, Imran M, Zaidi SJ, Kasak P. Highly efficient photocatalytic Z-scheme hydrogen production over oxygen-deficient WO3–x nanorods supported Zn0. 3Cd0. 7S heterostructure. Sci Rep 2017;7(1):6574.
[123] Peng J, Shen J, Yu X, Tang H, Liu Q. Construction of LSPR-enhanced 0D/2D CdS/MoO3− x S-scheme heterojunctions for visible-light-driven photocatalytic H2 evolution. Chin J Catal 2021;42(1):87–96.
[124] Zubair M, Svenum IH, Rønning M, Yang J. Core-shell nanostructures of graphene-wrapped CdS nanoparticles and TiO2 (CdS@ G@ TiO2): the role of graphene in enhanced photocatalytic H2 generation. Catalysts 2020;10(4):358.
[125] Peng Y, Kang S, Hu Z. Pt nanoparticle-decorated CdS photocalysts for CO2 reduction and H2 evolution. ACS Appl Nano Mater 2020;3(9):8632–9.
[126] Tian H, Liang J, Ma X, Cao L, Hu X, Gao M, Yang H, Liang Z. Enhanced photoelectrocatalytic H2 evolution over two-dimensional MoS2 nanosheets loaded on Cu-doped CdS nanorods. Chemelectrochem 2019;6(3):714–23.
[127] Lv Z, Li W, Cheng X, Liu B, Guo Z, Zhuang T, Zhang C. Constructing internal electric field in CdS via Bi, Ni co-doping strategy for enhanced visible-light H2 production. Appl Surf Sci 2021;556:149758.
[128] Zhao F, Li H, Liu T, Wang Y. Spatially separated CdS hollow spheres with interfacial charge transfer and cocatalyst for enhancing photocatalytic hydrogen evolution. Mol Catal 2019;474:110418.
[129] Lu X, Tong A, Luo D, Jiang F, Wei J, Huang Y, Jiang Z, Lu Z, Ni Y. Confining single Pt atoms from Pt clusters on multi-armed CdS for enhanced photocatalytic hydrogen evolution. J Mater Chem A 2022;10(9):4594–600.
[130] Li C, Du S, Lu C, Ren K, Wang Q, Shan S, Li Q, Fang Z, Li X, Dou W. Bimetallic MMoS4 (M= Ni, Co, Cu) cocatalysts architected CdS nanoflowers for synergistically boosting visible-light-driven photocatalytic H2 evolution from water and benzyl alcohol. J Alloys Compd 2022;924:166645.
[131] Wang H, Zhang L, Chen Z, Hu J, Li S, Wang Z, Liu J, Wang X. Semiconductor heterojunction photocatalysts: design, construction, and photocatalytic performances. Chem Soc Rev 2014;43(15):5234–44.
[132] Billah A, Tojo F, Kubota S, Hirose F, Ahmmad B. Organic molecule embedded CdS nanocomposite for hydrogen generation from water: effect of precursors' concentrations. Int J Hydrogen Energy 2021;46(71):35302–10.
[133] Lin YR, Chang YC, Chiao YC, Ko FH. Au@ CdS nanocomposites as a visible-light photocatalyst for hydrogen generation from tap water. Catalysts 2022;13(1):33.
[134] Xiang X, Zhu B, Cheng B, Yu J, Lv H. Enhanced photocatalytic H2-production activity of CdS quantum dots using Sn2+ as cocatalyst under visible light irradiation. Small 2020;16(26):2001024.
[135] Li C, Naghadeh SB, Guo L, Xu K, Zhang JZ, Wang H. Cellulose as sacrificial biomass for photocatalytic hydrogen evolution over one-dimensional CdS loaded with NiS2 as a cocatalyst. ChemistrySelect 2020;5(4):1470–7.
[136] Sun Q, Yu Z, Jiang R, Hou Y, Sun L, Qian L, Li F, Li M, Ran Q, Zhang H. CoP QD anchored carbon skeleton modified CdS nanorods as a co-catalyst for photocatalytic hydrogen production. Nanoscale 2020;12(37):19203–12.
[137] Liu YT, Lu MY, Perng TP, Chen LJ. Plasmonic enhancement of hydrogen production by water splitting with CdS nanowires protected by metallic TiN overlayers as highly efficient photocatalysts. Nano Energy 2021;89:106407.
[138] Qiu S, Shen Y, Wei G, Yao S, Xi W, Shu M, Si R, Zhang M, Zhu J, An C. Carbon dots decorated ultrathin CdS nanosheets enabling in-situ anchored Pt single atoms: a highly efficient solar-driven photocatalyst for hydrogen evolution. Appl Catal, B 2019;259:118036.
[139] Huang L, Gao R, Xiong L, Devaraji P, Chen W, Li X, Mao L. Two dimensional Ni 2 P/CdS photocatalyst for boosting hydrogen production under visible light irradiation. RSC Adv 2021;11(20):12153–61.
[140] Wang X, Zhao F, Zhang N, Wu W, Wang Y. Hollow spherical Pd/CdS/NiS with carrier spatial separation for photocatalytic hydrogen generation. Nanomaterials 2023;13(8):1326.
[141] Liu H, Zhao L, Yu J, Xiong G, Liu Z, Zhang X, Chu B, Liu X, Liu H, Zhou W. S doped Ta2O5 decorated CdS nanosphere via interfacial diffusion for enhanced and stable photocatalytic hydrogen production. Chem Eng J 2022;436:131673.
[142] Zhang Y, Peng Z, Guan S, Fu X. Novel β-NiS film modified CdS nanoflowers heterostructure nanocomposite: extraordinarily highly efficient photocatalysts for hydrogen evolution. Appl Catal, B 2018;224:1000–8.
[143] Feng M, Sun R, Zhan H, Chen Y. Lossless synthesis of graphene nanosheets decorated with tiny cmium sulfide quantum dots with excellent nonlinear optical properties. Nanotechnology 2010;21(7):075601.
[144] Huang H, Xu B, Tan Z, Jiang Q, Fang S, Li L, Bi J, Wu L. A facile in situ growth of CdS quantum dots on covalent triazine-based frameworks for photocatalytic H2 production. J Alloys Compd 2020;833:155057.
[145] Liang Q, Zhang C, Xu S, Zhou M, Zhou Y, Li Z. In situ growth of CdS quantum dots on phosphorus-doped carbon nitride hollow tubes as active 0D/1D heterostructures for photocatalytic hydrogen evolution. J Colloid Interface Sci 2020;577:1. 1.
[146] Li W, Han J, Wu Y, Xiang Q, Qiao Y, Feng C, Chen Z, Deng X. In-situ synthesis of CdS quantum dots on CdCO3 cubic structure for enhanced photocatalytic hydrogen production performance. Mater Lett 2019;255:126560.
[147] Zhuge K, Chen Z, Yang Y, Wang J, Shi Y, Li Z. In-suit photodeposition of MoS2 onto CdS quantum dots for efficient photocatalytic H2 evolution. Appl Surf Sci 2021;539:148234.
[148] Ma D, Shi JW, Zou Y, Fan Z, Ji X, Niu C. Highly efficient photocatalyst based on a CdS quantum dots/ZnO nanosheets 0D/2D heterojunction for hydrogen evolution from water splitting. ACS Appl Mater Interfaces 2017;9(30):25377–86.
[149] Shi JW, Sun D, Zou Y, Ma D, He C, Ji X, Niu C. Trap-level-tunable Se doped CdS quantum dots with excellent hydrogen evolution performance without co-catalyst. Chem Eng J 2019;364:11–9.
[150] Stavitskaya A, Glotov A, Pouresmaeil F, Potapenko K, Sitmukhanova E, Mazurova K, Ivanov E, Kozlova E, Vinokurov V, Lvov Y. CdS quantum dots in hierarchical mesoporous silica templated on clay nanotubes: implications for photocatalytic hydrogen production. ACS Appl Nano Mater 2021;5(1):605–14.
[151] Xie J, Li Y, Nie D, Wang L, Chen J, Li B, He JB, Guo Z, Lau TC. Minutely dispersed ruthenium in tremella-like N-doped carbon for enhanced visible-light-driven photocatalytic hydrogen production by CdS quantum dots. Inorg Chem Front 2022;9(19):4999–5007.
[152] Cheng L, Xiang Q, Liao Y, Zhang H. CdS-based photocatalysts. Energy Environ Sci 2018;11(6):1362–91.
[153] Zhang L, Ai Z, Xu X, Shi D, Zhang B, Hu H, Yang M, Shao Y, Wu Y, Hao X. Research progress on synthetic and modification strategies of CdS-based photocatalysts. Ionics 2023;29(6):2115–39.
[154] Xu M, Jiang L, Wang J, Feng S, Tremblay PL, Zhang T. Efficient photocatalytic hydrogen evolution with high-crystallinity and noble metal-free red phosphorus-CdS nanorods. Int J Hydrogen Energy 2020;45(35):17354–66.
[155] Sheng CK, Aziz NA, Alrababah YM. Annealing temperature-dependent CdS phase tunability in improving photocatalytic efficiency towards aquatic dye decomposition. Results Mater 2023;19:100445.
[156] Li Q, Li X, Yu J. Surface and interface modification strategies of CdS-based photocatalysts. In: InInterface science and technology, vol. 31. Elsevier; 2020. p. 313–48.
[157] Bai S, Li H, Guan Y, Jiang S. The enhanced photocatalytic activity of CdS/TiO2 nanocomposites by controlling CdS dispersion on TiO2 nanotubes. Appl Surf Sci 2011;257(15):6406–9.
[158] Lang D, Xiang Q, Qiu G, Feng X, Liu F. Effects of crystalline phase and morphology on the visible light photocatalytic H 2-production activity of CdS nanocrystals. Dalton Trans 2014;43(19):7245–53.
[159] Metin H, Ari M, Erat S, Durmuş S, Bozoklu M, Braun A. The effect of annealing temperature on the structural, optical, and electrical properties of CdS films. J Mater Res 2010;25(1):189–96.
[160] Vaquero F, Navarro RM, Fierro JL. Influence of the solvent on the structure, morphology and performance for H2 evolution of CdS photocatalysts prepared by solvothermal method. ppl. Catal., B 2017;203:753–67.
[161] Bao N, Shen L, Takata T, Domen K. Self-templated synthesis of nanoporous CdS nanostructures for highly efficient photocatalytic hydrogen production under visible light. Chem Mater 2008;20(1):110–7.
[162] Wang Y, Zhang X, Liu Y, Zhao Y, Xie C, Song Y, Yang P. Crystallinity and phase controlling of g-C3N4/CdS hetrostructures towards high efficient photocatalytic H2 generation. nt. J. Hydrogen Energy 2019;44(57):30151–9.
[163] Deng Q, Chen L, Shen L, Xia X, Zhang Q. Centimeter-scale CdS single-crystal nanoscale-thick films via chemical vapor deposition for high-performance photodetectors. ACS Appl Nano Mater 2024.
[164] Naik VM, Haddad D, Naik R, Benci J, Auner GW. Optical properties of anatase, rutile and amorphous phases of TiO2 thin films grown at room temperature by RF magnetron sputtering. MRS Online Proc Libr 2002;755:DD11–12.
[165] Qin N, Li L, Zheng H, Cui Q. CdS with tunable crystalline phase structures: controllable preparation and enhanced photocatalytic properties. Res Chem Intermed 2023;49(12):5505–16.
[166] Yang X, Wang B, Mu Y, Zheng M, Wang Y. Photocatalytic performance of cubic and hexagonal phase CdS synthesized via different Cd sources. J Electron Mater 2019;48:2895–901.
[167] Shen Q, Xue J, Mi A, Jia H, Liu X, Xu B. The study on properties of CdS photocatalyst with different ratios of zinc-blende and wurtzite structure. RSC Adv 2013;3(43):20930–5.
[168] Yu J, Yu Y, Cheng B. Enhanced visible-light photocatalytic H 2-production performance of multi-armed CdS nanorods. RSC Adv 2012;2(31):11829–35.
[169] Bao N, Shen L, Takata T, Domen K, Gupta A, Yanagisawa K, Grimes CA. Facile Cd− thiourea complex thermolysis synthesis of phase-controlled CdS nanocrystals for photocatalytic hydrogen production under visible light. J Phys Chem C 2007; 111(47):17527–34.
[170] Yu H, Zhong W, Huang X, Wang P, Yu J. Suspensible cubic-phase CdS nanocrystal photocatalyst: facile synthesis and highly efficient H2-evolution performance in a sulfur-rich system. ACS Sustainable Chem Eng 2018;6(4):5513–23.
[171] Jin J, Yu J, Liu G, Wong PK. Single crystal CdS nanowires with high visible-light photocatalytic H 2-production performance. J Mater Chem A 2013;1(36): 10927–34.

[172] Nagakawa H, Tatsuma T. Highly crystalline wurtzite CdS prepared by a flux method and application to photocatalysis. CS Appl. Energy Mater 2022;5(12):14652–7.
[173] Vinodgopal K, Kamat PV. Enhanced rates of photocatalytic degradation of an azo dye using SnO2/TiO2 coupled semiconductor thin films. Environ Sci Technol 1995;29(3):841–5.
[174] Manna K, Ganguly P, Ghosh S. Role of metal-semiconductor interface in photocatalytic processes. J Mater Sci 2020;55(8):3864–78.
[175] Zaleska-Medynska A, Marchelek M, Diak M, Grabowska E. Noble metal-based bimetallic nanoparticles: the effect of the structure on the optical, catalytic and photocatalytic properties. Adv Colloid Interface Sci 2016;229:80–107.
[176] Kumari P, Bahadur N, Kong L, O'Dell LA, Merenda A, Dumée LF. Engineering Schottky-like and heterojunction materials for enhanced photocatalysis performance–a review. Mater Adv 2022;3(5):2309–23.
[177] Tian J, Zhao Z, Ling H, Zhang Z, Ablat H, Nurmamat X. Review on photocatalytic nitrogen fixation by local surface plasmon. Int J Hydrogen Energy 2024;87:686–98.
[178] Nazir MA, Najam T, Altaf M, Ahmad K, Hossain I, Assiri MA, Javed MS, ur Rehman A, Shah SS. Tuning the photocatalytic hydrogen production via co-catalyst engineering. J Alloys Compd 2024:174378.
[179] Li R, Gao T, Wang Y, Chen Y, Luo W, Wu Y, Xie Y, Wang Y, Zhang Y. Engineering of bimetallic Au–Pd alloyed particles on nitrogen defects riched g-C3N4 for efficient photocatalytic hydrogen production. Int J Hydrogen Energy 2024;63:1116–27.
[180] Li W, Chu XS, Wang F, Dang YY, Liu XY, Ma TH, Li JY, Wang CY. Pd single-atom decorated CdS nanocatalyst for highly efficient overall water splitting under simulated solar light. Appl Catal, B 2022;304:121000.
[181] Dong J, Duan L, Wu Q, Yao W. Facile preparation of Pt/CdS photocatalyst by a modified photoreduction method with efficient hydrogen production. Int J Hydrogen Energy 2018;43(4):2139–47.
[182] Li C, Naghadeh SB, Guo L, Xu K, Zhang JZ, Wang H. Cellulose as sacrificial biomass for photocatalytic hydrogen evolution over one-dimensional CdS loaded with NiS2 as a cocatalyst. ChemistrySelect 2020;5(4):1470–7.
[183] Gao R, Xiong L, Huang L, Chen W, Li X, Liu X, Mao L. A new structure of Pt NF@Ni (OH) 2/CdS heterojunction: preparation, characterization and properties in photocatalytic hydrogen generation. Chem Eng J 2022;430:132726.
[184] Mao L, Liu H, Liu S, Ba Q, Wang H, Gao L, Li X, Huang C, Chen W. Pt-Ru bi-metal co-catalyst: preparation, characterization and its effect on CdS's activity for water splitting under visible light. Mater Res Bull 2017;93:9–15.
[185] Ren Y, Li Y, Pan G, Wang N, Xing Y, Zhang Z. Recent progress in CdS-based S-scheme photocatalysts. J Mater Sci Technol 2024;171:162–84.
[186] Sajna MS, Vimal G, Sadasivuni KK. Plasmonic catalysis for energy conversion-an overview and recent trends. Top Catal 2022:1–20.
[187] Xiong J, Du X, Cheng G, Yang H, Chen J, Dou S, Li Z. One dimensional hierarchical nanostructures composed of CdS nanosheets/nanoparticles and Ag nanowires with promoted photocatalytic performance. Inorg Chem Front 2018;5(4):903–15.
[188] Kanan MW, Surendranath Y, Nocera DG. Cobalt–phosphate oxygen-evolving compound. Chem Soc Rev 2009;38(1):109–14.
[189] Di T, Zhu B, Zhang J, Cheng B, Yu J. Enhanced photocatalytic H2 production on CdS nanorod using cobalt-phosphate as oxidation cocatalyst. Appl Surf Sci 2016;389:775–82.
[190] Gopannagari M, Rangappa AP, Seo S, Kim E, Reddy KA, Bhavani P, Reddy DA, Kumar DP, Kim TK. Atomically engineered molybdenum di-sulfide by dual heteroatom doping for accelerating hydrogen evolution reaction on cadmium sulfide nanorods. Solid State Sci 2022;134:107047.
[191] Gai Q, Zheng X, Liu W, Dong Q, Wang Y, Gao R, Ren S. 2D-2D heterostructured CdS–CoP photocatalysts for efficient H2 evolution under visible light irradiation. Int J Hydrogen Energy 2019;44(50):27412–20.
[192] Chen T, Yang C, Rajendran S, Lei Y, Zhang X, Qin J. Boosting visible-light hydrogen evolution on CdS hollow nanospheres with CoN as cocatalyst. Fuel 2022;316:123307.
[193] Zhu W, Yang L, Liu F, Si Z, Huo M, Li Z, Chen Z. Metal Ni nanoparticles in-situ anchored on CdS nanowires as effective cocatalyst for boosting the photocatalytic H2 production and degradation activity. J Alloys Compd 2024;973:172747.
[194] Zhao H, Liu J, Zhong N, Larter S, Li Y, Kibria MG, Su BL, Chen Z, Hu J. Biomass photoreforming for hydrogen and value-added chemicals co-production on hierarchically porous photocatalysts. Adv Energy Mater 2023;13(21):2300257.
[195] Maurya A, Majhi KC, Yadav M. Progress on Ni-based as Co-catalysts for water splitting. In: Materials for hydrogen production. Conversion, and Storage; 2023. p. 575–623.
[196] Ke X, Dai K, Zhu G, Zhang J, Liang C. In situ photochemical synthesis noble-metal-free NiS on CdS-diethylenetriamine nanosheets for boosting photocatalytic H2 production activity. Appl Surf Sci 2019;481:669–77.
[197] Zheng Z, Wang T, Han F, Yang Q, Li B. Synthesis of Ni modified Au@ CdS core–shell nanostructures for enhancing photocatalytic coproduction of hydrogen and benzaldehyde under visible light. J Colloid Interface Sci 2022;606:47–56.
[198] Zhang B, Chen C, Liu J, Qiao W, Zhao J, Yang J, Yu Y, Chen S, Qin Y. Simultaneous Ni nanoparticles decoration and Ni doping of CdS nanorods for synergistically promoting photocatalytic H2 evolution. Appl Surf Sci 2020;508:144869.
[199] Nakibli Y, Mazal Y, Dubi Y, Wächtler M, Amirav L. Size matters: cocatalyst size effect on charge transfer and photocatalytic activity. Nano Lett 2018;18(1):357–64.
[200] Wang H, Chen W, Zhang J, Huang C, Mao L. Nickel nanoparticles modified CdS–A potential photocatalyst for hydrogen production through water splitting under visible light irradiation. Int J Hydrogen Energy 2015;40(1):340–5.
[201] Kim JY, Roh SH, Xia C, Sim U, Kim JK. MXene-based hybrid materials for electrochemical and photoelectrochemical H2 generation. J Energy Chem 2024.
[202] Pan J, Li H, Li S, Ou W, Liu Y, Wang J, Song C, Zheng Y, Li C. The enhanced photocatalytic hydrogen production of nickel-cobalt bimetals sulfide synergistic modified CdS nanorods with active facets. Renew Energy 2020;156:469–77.
[203] Sathyaseelan A, Elumalai V, Krishnamoorthy K, Sajeev A, Kim SJ. Sphere-like PdNi alloy: unveiling the twin functional properties toward oxygen reduction and temperature-dependent methanol oxidation for alkaline direct methanol fuel cells. ACS Sustainable Chem Eng 2023;11(14):5345–55.
[204] Lin M, Chen H, Zhang Z, Wang X. Engineering interface structures for heterojunction photocatalysts. Phys Chem Chem Phys 2023;25(6):4388–407.
[205] Andrä M, Funck C, Raab N, Rose MA, Vorokhta M, Dvorák F, Gunkel F. Effect of cationic interface defects on band alignment and contact resistance in metal/oxide heterojunctions. Advan Electron Mater 2020;6(1):1900808.
[206] Pande KP. Rectification properties of CdS Schottky barrier diodes with evaporated Au/Ti as blocking contact. Phys Status Solidi (a) 1977;42(2):615–9.
[207] Lu Z, Hou G, Zhu Y, Chen J, Xu J, Chen K. High efficiency organic–Si hybrid solar cells with a one-dimensional CdS interlayer. Nanoscale 2021;13(7):4206–12.
[208] Yang J, Yan H, Wang X, Wen F, Wang Z, Fan D, Li C. Roles of cocatalysts in Pt–PdS/CdS with exceptionally high quantum efficiency for photocatalytic hydrogen production. J Catal 2012;290:151–7.
[209] Fu H, Zhao H, Yang X, Xiong S, An X. High-performance MoS2/CdS nanodiamonds for photocatalytic hydrogen evolution under visible light irradiation. Powder Technol 2022;406:117596.
[210] Liu YT, Lu MY, Perng TP, Chen LJ. Plasmonic enhancement of hydrogen production by water splitting with CdS nanowires protected by metallic TiN overlayers as highly efficient photocatalysts. Nano Energy 2021;89:106407.
[211] Hussain E, Ishaq A, Abid MZ, Waleed MZ, Rauf A, Jin R, Rafiq K. Sunlight-driven hydrogen generation: acceleration of synergism between Cu–Ag cocatalysts on a CdS system. ACS Appl Energy Mater 2024;7(5):1914–26.
[212] Cai M, Cao S, Zhuo Z, Wang X, Shi K, Cheng Q, Xue Z, Du X, Shen C, Liu X, Wang R. Fabrication of Ni2P cocatalyzed CdS nanorods with a well-defined heterointerface for enhanced photocatalytic H2 evolution. Catalysts 2022;12(4):417.
[213] Feng LL, Yu G, Wu Y, Li GD, Li H, Sun Y, Asefa T, Chen W, Zou X. High-index faceted Ni3S2 nanosheet arrays as highly active and ultrastable electrocatalysts for water splitting. J Am Chem Soc 2015;137(44):14023–6.
[214] Ma Y, Hai G, Liu J, Bao J, Li Y, Wang G. Enhanced visible light photocatalytic hydrogen evolution by intimately contacted Ni2P decorated Ni-doped CdS nanospheres. Chem Eng J 2022;441:136002.
[215] Zhang K, Mou Z, Cao S, Wu S, Xu X, Li C. Well-designed NiS/CdS nanoparticles heterojunction for efficient visible-light photocatalytic H2 evolution. Int J Hydrogen Energy 2022;47(25):12605–14.
[216] Zhu Z, Zhang S, Chen G, Meng S, Zheng X, Chen S, Zhang F. Minimized Pt deposition on CdS simultaneously maximizes the performance of hydrogen production and aromatic alcohols oxidation. Appl Surf Sci 2021;564:150446.
[217] Guo C, Tian K, Wang L, Liang F, Wang F, Chen D, Ning J, Zhong Y, Hu Y. Approach of fermi level and electron-trap level in cadmium sulfide nanorods via molybdenum doping with enhanced carrier separation for boosted photocatalytic hydrogen production. J Colloid Interface Sci 2021;583:661–71.
[218] Reddy CV, Reddy KR, Harish VA, Shim J, Shankar MV, Shetti NP, Aminabhavi TM. Metal-organic frameworks (MOFs)-based efficient heterogeneous photocatalysts: synthesis, properties and its applications in photocatalytic hydrogen generation, CO2 reduction and photodegradation of organic dyes. Int J Hydrogen Energy 2020;45(13):7656–79.
[219] Li X, Gao Y, Li N, Ge L. In-situ constructing cobalt incorporated nitrogen-doped carbon/CdS heterojunction with efficient interfacial charge transfer for photocatalytic hydrogen.
[220] Sahoo DP, Nayak S, Reddy KH, Martha S, Parida K. Fabrication of a Co (OH) 2/ZnCr LDH "p–n" heterojunction photocatalyst with enhanced separation of charge carriers for efficient visible-light-driven H2 and O2 evolution. Inorg Chem 2018;57(7):3840–54. heterojunctions for effective photocatalytic H2 evolution. J. Mater. Sci. Technol 2022;112:85-3854.
[221] Zhao W, Liu J, Ding Z, Zhang J, Wang X. Optimal synthesis of platinum-free 1D/2D CdS/MoS2 (CM) heterojunctions with improved photocatalytic hydrogen production performance. J Alloys Compd 2020;813:152234.
[222] Zhang M, Lin H, Cao J, Guo X, Chen S. Construction of novel S/CdS type II heterojunction for photocatalytic H2 production under visible light: the intrinsic positive role of elementary α-S. Chem Eng J 2017;321:484–94.
[223] Kolivand A, Sharifnia S. Enhanced photocatalytic hydrogen evolution from water splitting by Z-scheme CdS/BiFeO3 heterojunction without using sacrificial agent. Int J Energy Res 2021;45(2):2739–52.
[224] Ma S, Xie J, Wen J, He K, Li X, Liu W, Zhang X. Constructing 2D layered hybrid CdS nanosheets/MoS2 heterojunctions for enhanced visible-light photocatalytic H2 generation. Appl Surf Sci 2017;391:580–91.
[225] Sumesh CK, Peter SC. Two-dimensional semiconductor transition metal based chalcogenide based heterostructures for water splitting applications. Dalton Trans 2019;48(34):12772–802.
[225a] Fu H, Zhao H, Yang X, Xiong S, An X. High-performance MoS2/CdS nanodiamonds for photocatalytic hydrogen evolution under visible light irradiation. Powder Technol 2022;406:117596.

[226] Wu A, Tian C, Jiao Y, Yan Q, Yang G, Fu H. Sequential two-step hydrothermal growth of MoS2/CdS core-shell heterojunctions for efficient visible light-driven photocatalytic H2 evolution. Appl Catal, B 2017;203:955–63.
[227] Liu Y, Niu H, Gu W, Cai X, Mao B, Li D, Shi W. In-situ construction of hierarchical CdS/MoS2 microboxes for enhanced visible-light photocatalytic H2 production. Chem Eng J 2018;339:117–24.
[228] Zhang ZW, Li QH, Qiao XQ, Hou D, Li DS. One-pot hydrothermal synthesis of willow branch-shaped MoS2/CdS heterojunctions for photocatalytic H2 production under visible light irradiation. Chin J Catal 2019;40(3):371–9.
[229] Lin H, Li Y, Li H, Wang X. Multi-node CdS hetero-nanowires grown with defect-rich oxygen-doped MoS 2 ultrathin nanosheets for efficient visible-light photocatalytic H 2 evolution. Nano Res 2017;10:1377–92.
[230] Zhuge K, Chen Z, Yang Y, Wang J, Shi Y, Li Z. In-suit photodeposition of MoS2 onto CdS quantum dots for efficient photocatalytic H2 evolution. Appl Surf Sci 2021;539:148234.
[231] Lu X, Chen W, Yao Y, Wen X, Hart JN, Tsounis C, Toe CY, Scott J, Ng YH. Photogenerated charge dynamics of CdS nanorods with spatially distributed MoS2 for photocatalytic hydrogen generation. Chem Eng J 2021;420:127709.
[232] Su L, Luo L, Wang J, Song T, Tu W, Wang ZJ. Lamellar flower-like porous MoS 2 as an efficient cocatalyst to boost photocatalytic hydrogen evolution of CdS. Catal Sci Technol 2021;11(4):1292–7.
[233] Yin XL, Li LL, Li DC, Li ZJ, Wang YX, Kong XJ, Zhao JS, Jiang JH, Qian JC, Pang DH, Du XX. Noble-metal-free CdS@ MoS2 core-shell nanoheterostructures for efficient and stabilized visible-light-driven H2 generation. Int J Hydrogen Energy 2019;44(31):16657–66.
[234] Feng C, Chen Z, Hou J, Li J, Li X, Xu L, Sun M, Zeng R. Effectively enhanced photocatalytic hydrogen production performance of one-pot synthesized MoS2 clusters/CdS nanorod heterojunction material under visible light. Chem Eng J 2018;345:404–13.
[235] Yang Y, Zhang Y, Fang Z, Zhang L, Zheng Z, Wang Z, Feng W, Weng S, Zhang S, Liu P. Simultaneous realization of enhanced photoactivity and promoted photostability by multilayered MoS2 coating on CdS nanowire structure via compact coating methodology. ACS Appl Mater Interfaces 2017;9(8):6950–8.
[236] Yu X, Du R, Li B, Zhang Y, Liu H, Qu J, An X. Biomolecule-assisted self-assembly of CdS/MoS2/graphene hollow spheres as high-efficiency photocatalysts for hydrogen evolution without noble metals. Appl Catal, B 2016;182:504–12.
[237] Xiong M, Yan J, Chai B, Fan G, Song G. Liquid exfoliating CdS and MoS2 to construct 2D/2D MoS2/CdS heterojunctions with significantly boosted photocatalytic H2 evolution activity. J Mater Sci Technol 2020;56:179–88.
[238] Zhang K, Mou Z, Cao S, Meng T, Li J, Ling G, Zhang X, Zhou Z, Meng W. MoS2 grown in situ on CdS nanosheets for boosted photocatalytic hydrogen evolution under visible light. Int J Hydrogen Energy 2022;47(5):2967–75.
[239] Liu P, Zhu J, Zhang J, Xi P, Tao K, Gao D, Xue D. P dopants triggered new basal plane active sites and enlarged interlayer spacing in MoS2 nanosheets toward electrocatalytic hydrogen evolution. ACS Energy Lett 2017;2(4):745–52.
[240] Yang S, Li G, Qu C, Wang G, Wang D. Simple synthesis of ZnO nanoparticles on N-doped reduced graphene oxide for the electrocatalytic sensing of l-cysteine. RSC Adv 2017;7(56):35004–11.
[241] Pan JB, Shen S, Chen L, Au CT, Yin SF. Core–shell photoanodes for photoelectrochemical water oxidation. Adv Funct Mater 2021;31(36):2104269.
[242] Jenjeti RN, Kumar R, Austeria MP, Sampath S. Field effect transistor based on layered NiPS 3. Sci Rep 2018;8(1):8586.
[243] Wang F, Shifa TA, He P, Cheng Z, Chu J, Liu Y, Wang Z, Wang F, Wen Y, Liang L, He J. Two-dimensional metal phosphorus trisulfide nanosheet with solar hydrogen-evolving activity. Nano Energy 2017;40:673–80.
[244] Ran J, Zhang H, Fu S, Jaroniec M, Shan J, Xia B, Qu Y, Qu J, Chen S, Song L, Cairney JM. NiPS3 ultrathin nanosheets as versatile platform advancing highly active photocatalytic H2 production. Nat Commun 2022;13(1):4600.
[245] Chen W, Liu TY, Huang T, Liu XH, Duan GR, Yang XJ, Chen SM. A novel yet simple strategy to fabricate visible light responsive C, N-TiO 2/gC 3 N 4 heterostructures with significantly enhanced photocatalytic hydrogen generation. RSC Adv 2015;5(122):101214–20.
[246] Zhang H, Kong X, Yu F, Wang Y, Liu C, Yin L, Huang J, Feng Q. Ni (OH) 2 nanosheets modified hexagonal pyramid CdS formed type II heterojunction photocatalyst with high-visible-light H2 evolution. ACS Appl Energy Mater 2021; 4(11):13152–60.
[247] Tso S, Li WS, Wu BH, Chen LJ. Enhanced H2 production in water splitting with CdS-ZnO core-shell nanowires. Nano Energy 2018;43:270–7.
[248] Guo X, Liu X, Yan J, Liu SF. Heteroepitaxial growth of core-shell ZnO/CdS heterostructure for efficient and stable photocatalytic hydrogen generation. Int J Hydrogen Energy 2022;47(81):34410–20.
[249] Ma D, Wang Z, Shi JW, Zou Y, Lv Y, Ji X, Li Z, Cheng Y, Wang L. An ultrathin Al 2 O 3 bridging layer between CdS and ZnO boosts photocatalytic hydrogen production. J Mater Chem A 2020;8(21):11031–42.
[250] Zhang M, Lin H, Cao J, Guo X, Chen S. Construction of novel S/CdS type II heterojunction for photocatalytic H2 production under visible light: the intrinsic positive role of elementary α-S. Chem Eng J 2017;321:484–94.
[251] Liu H, Tan P, Liu Y, Zhai H, Du W, Liu X, Pan J. Ultrafast interfacial charge evolution of the Type-II cadmium Sulfide/Molybdenum disulfide heterostructure for photocatalytic hydrogen production. J Colloid Interface Sci 2022;619:246–56.
[252] Zhang D, Teng J, Yang H, Fang Z, Song K, Wang L, Hou H, Lu X, Bowen CR, Yang W. Air-condition process for scalable fabrication of CdS/ZnS 1D/2D heterojunctions toward efficient and stable photocatalytic hydrogen production. Carbon Energy 2023;5(7):e277.
[253] Lang D, Shen T, Xiang Q. Roles of MoS2 and graphene as cocatalysts in the enhanced visible-light photocatalytic H2 production activity of multiarmed CdS nanorods. ChemCatChem 2015;7(6):943–51.
[254] Sun G, Shi JW, Mao S, Ma D, He C, Wang H, Cheng Y. Dodecylamine coordinated tri-arm CdS nanorod wrapped in intermittent ZnS shell for greatly improved photocatalytic H2 evolution. Chem Eng J 2022;429:132382.
[255] Lin Y, Zhang Q, Li Y, Liu Y, Xu K, Huang J, Zhou X, Peng F. The evolution from a typical type-I CdS/ZnS to type-II and Z-scheme hybrid structure for efficient and stable hydrogen production under visible light. ACS Sustainable Chem Eng 2020; 8(11):4537–46.
[256] Li P, Liu M, Li J, Guo J, Zhou Q, Zhao X, Wang S, Wang L, Wang J, Chen Y, Zhang J. Atomic heterojunction-induced accelerated charge transfer for boosted photocatalytic hydrogen evolution over 1D CdS nanorod/2D ZnIn2S4 nanosheet composites. J Colloid Interface Sci 2021;604:500–7.
[257] Liu H, Chen J, Guo W, Xu Q, Min Y. A high efficiency water hydrogen production method based on CdS/WN composite photocatalytic. J Colloid Interface Sci 2022; 613:652–60.
[258] Zhi Y, Wang Z, Zhang HL, Zhang Q. Recent progress in metal-free covalent organic frameworks as heterogeneous catalysts. Small 2020;16(24):2001070.
[259] Liang Q, Cui S, Liu C, Xu S, Yao C, Li Z. Construction of CdS@ UIO-66-NH2 core-shell nanorods for enhanced photocatalytic activity with excellent photostability. J Colloid Interface Sci 2018;524:379–87.
[260] Xia Z, Yu R, Yang H, Luo B, Huang Y, Li D, Shi J, Xu D. Novel 2D Zn-porphyrin metal organic frameworks revived CdS for photocatalysis of hydrogen production. Int J Hydrogen Energy 2022;47(27):13340–50.
[261] Wang Y, Liu C, Kong C, Zhang F. Defect MoS2 and Ti3C2 nanosheets co-assisted CdS to enhance visible-light driven photocatalytic hydrogen production. Colloids Surf, A 2022;652:129746.
[262] Bo T, Wang Y, Wang J, Zhao Z, Zhang J, Zheng K, Lin T, Zhang B, Shao L. Photocatalytic H2 evolution on CdS modified with partially crystallized MoS2 under visible light irradiation. Chem Phys Lett 2020;746:137305.
[263] Yin XL, Li LL, Li DC, Dou JM. One-pot synthesis of CdS-MoS2/RGO-E nano-heterostructure with well-defined interfaces for efficient photocatalytic H2 evolution. Int J Hydrogen Energy 2018;43(45):20382–91.
[264] Sun J, Yin M, Li Y, Liang K, Fan Y, Li Z. Efficient photocatalytic hydrogen production of ternary composite constituted by cubic CdS, MoS2 and activated carbon. J Alloys Compd 2021;874:159930.
[265] Cheng Y, Dou M, Yao M, Ding K, Shao H, Liu Y, Li S, Chen Y. Reverse-Type-I MnCo2S4/CdS heterojunction nanorods for highly efficient photocatalytic hydrogen production under visible light irradiation. ACS Appl Nano Mater 2023;6 (18):16837–45.
[266] Li Z, Wang Y, Luo Y, Xiao R, Ye H, Xie Y, Ma Y, Chen Y, Ling Y. CoP-modified CdS for enhanced stability and photocatalytic hydrogen production under visible light. Phys Chem Chem Phys 2023;25(29):19553–61.
[267] Yuan W, Zhang Z, Cui X, Liu H, Tai C, Song Y. Fabrication of hollow mesoporous CdS@ TiO2@ Au microspheres with high photocatalytic activity for hydrogen evolution from water under visible light. ACS Sustain Chem Eng 2018;6(11): 13766–9561.
[268] Manchala S, Gandamalla A, Vempuluru NR, Venkatakrishnan SM, Shanker V. High potential and robust ternary LaFeO3/CdS/carbon quantum dots nanocomposite for photocatalytic H2 evolution under sunlight illumination. J Colloid Interface Sci 2021;583:255–66.
[269] Sun B, Zheng J, Yin D, Jin H, Wang X, Xu Q, Liu A, Wang S. Dual cocatalyst modified CdS achieving enhanced photocatalytic H2 generation and benzylamine oxidation performance. Appl Surf Sci 2022;592:153277.
[270] Pan J, Wang P, Wang P, Yu Q, Wang J, Song C, Zheng Y, Li C. The photocatalytic overall water splitting hydrogen production of g-C3N4/CdS hollow core–shell heterojunction via the HER/OER matching of Pt/MnOx. Chem Eng J 2021;405: 126622.
[271] Cao J, Li X, Lin H, Chen S, Fu X. In situ preparation of novel p–n junction photocatalyst BiOI/(BiO) 2CO3 with enhanced visible light photocatalytic activity. J Hazard Mater 2012;239:316–24.
[272] Liu R, Wang F, Liu L, He X, Chen J, Li Y, Zhai T. Band alignment engineering in two-dimensional transition metal dichalcogenide-based heterostructures for photodetectors. Small Struct 2021;2(3):2000136.
[273] Lee SH, Lee SW, Jeon T, Park DH, Jung SC, Jang JW. Efficient direct electron transfer via band alignment in hybrid metal-semiconductor nanostructures toward enhanced photocatalysts. Nano Energy 2019;63:103841.
[274] Liu Z, Yao S, Zhang A, Li Y, Fu Y, Zhou Q. Intramolecular built-in electric field enhanced polymerized nitrogen-carbon homojunction π*-electron delocalization enrichment promotes photocatalytic uranium (VI) reduction. Appl Catal, B 2023; 338:123023.
[275] Li H, Zhou Y, Tu W, Ye J, Zou Z. State-of-the-art progress in diverse heterostructured photocatalysts toward promoting photocatalytic performance. Adv Funct Mater 2015;25(7):998–1013.
[276] Zhang L, Zhang X, Lu G. Band alignment in two-dimensional halide perovskite heterostructures: type I or type II? J Phys Chem Lett 2020;11(8):2910–6.
[277] Shokri A, Yazdani A. Band alignment engineering, electronic and optical properties of Sb/PtTe2 van der Waals heterostructure: effects of electric field and biaxial strain. J Mater Sci 2021;56(9):5658–69.
[278] Zhng J, Qiao SZ, Qi L, Yu J. Fabrication of NiS modified CdS nanorod p–n junction photocatalysts with enhanced visible-light photocatalytic H 2-production activity. Phys Chem Chem Phys 2013;15(29):12088–94.
[279] Zhang J, Zhu Z, Feng X. Construction of two-dimensional MoS2/CdS p–n nanohybrids for highly efficient photocatalytic hydrogen evolution. Chem Eur J 2014;20(34):10632–5.

[280] Kumar U, Das Chakraborty S, Sahu RK, Bhattacharya P, Mishra T. Improved interfacial charge transfer on noble metal-free biomimetic CdS-based tertiary heterostructure@ 2D MoS2-CdS-Cu2O with enhanced photocatalytic water splitting. Adv Mater Interfac 2022;9(2):2101680.
[281] Li Y, Zhao Q, Zhang Y, Li Y, Fan L, Li FT, Li X. In-situ construction of sequential heterostructured CoS/CdS/CuS for building "electron-welcome zone" to enhance solar-to-hydrogen conversion. Appl Catal, B 2022;300:120763.
[282] Deng C, Ye F, Wang T, Ling X, Peng L, Yu H, Ding K, Hu H, Dong Q, Le H, Han Y. Developing hierarchical CdS/NiO hollow heterogeneous architectures for boosting photocatalytic hydrogen generation. Nano Res 2022;1:1. 0.
[283] Chen L, Ning S, Xia Y, Liang L, Huang R, Yan G, Wang X. Spatial charge separation in nicale phosphide modified CDS nanorods for efficient photocatalytic hydrogen evolution. 2022. Available at: SSRN 4011870.
[284] He X, Zeng Q, Zheng H, Ong WJ, He Y, Huang B, Li L, Zeng D. Insight into NiCo-based nanosheets modified MnS/Mn0· 2Cd0· 8S hybrids for enhanced visible-light photocatalytic H2 evolution. Int J Hydrogen Energy 2022;47(29):13862–75.
[285] Ai Z, Zhang K, Shi D, Chang B, Shao Y, Zhang L, Wu Y, Hao X. Band-matching transformation between CdS and BCNNTs with tunable pn homojunction for enhanced photocatalytic pure water splitting. Nano Energy 2020;69:104408.
[286] Wei L, Zeng D, Xie Z, Zeng Q, Zheng H, Fujita T, Wei Y. NiO nanosheets coupled with CdS nanorods as 2D/1D heterojunction for improved photocatalytic hydrogen evolution. Front Chem 2021;9:655583.
[287] Liu S, Guo X, Wang W, Yang Y, Zhu C, Li C, Lin W, Tian Q, Liu Y. CdS-Cu1. 81S heteronanorods with continuous sublattice for photocatalytic hydrogen production. Appl Catal, B 2022;303:120909.
[288] Yu L, Li X, Duan L, Zhang Y, Zhu H. Oxygen vacancies-induced dendritic SrTiO3/CdS p–n heterostructures photocatalyst for ultrahigh hydrogen evolution. Sol RRL 2023;7(14):2300259.
[289] Ai Z, Huang M, Shi D, Yang M, Hu H, Zhang B, Shao Y, Shen J, Wu Y, Hao X. Phase engineering of CdS optimized by BP with pn junction: establishing spatial-gradient charges transmission mode toward efficient photocatalytic water reduction. Appl Catal, B 2022;315:121577.
[290] Zhang H, Feng Q, Zhang Y, Zhang J, Wu X, Li Y, Yin L, Huang J, Kong X. A CdS/MnS p–n heterojunction with a directional carrier diffusion path for efficient photocatalytic H 2 production. norg. Chem. Front 2022;9(6):1100–6.
[291] Hao X, Hu Z, Xiang D, Jin Z. Construction of CdS@ Cu2-xS core− shell pn heterojunction with enhanced charge separation for wide spectrum photocatalytic H2 evolution. Mol Catal 2022;528:112417.
[292] Fan X, Wang B, Heng Q, Chen W, Mao L. Facile in-situ synthesis of α-NiS/CdS pn junction with enhanced photocatalytic H2 production activity. Int J Hydrogen Energy 2022;47(76):32531–42.
[293] Yuan M, Zhou WH, Kou DX, Zhou ZJ, Meng YN, Wu SX. Cu2ZnSnS4 decorated CdS nanorods for enhanced visible-light-driven photocatalytic hydrogen production. Int J Hydrogen Energy 2018;43(45):20408–16.
[294] Vamvasakis I, Papadas IT, Tzanoudakis T, Drivas C, Choulis SA, Kennou S, Armatas GS. Visible-light photocatalytic H2 production activity of β-Ni (OH) 2-modified CdS mesoporous nanoheterojunction networks. ACS Catal 2018;8(9):8726–38.
[295] Tada H, Mitsui T, Kiyonaga T, Akita T, Tanaka K. All-solid-state Z-scheme in CdS–Au–TiO2 three-component nanojunction system. Nat Mater 2006;5(10):782–6.
[296] Chen W, Yan RQ, Zhu JQ, Huang GB, Chen Z. Highly efficient visible-light-driven photocatalytic hydrogen evolution by all-solid-state Z-scheme CdS/QDs/ZnIn2S4 architectures with MoS2 quantum dots as solid-state electron mediator. Appl Surf Sci 2020;504:144406.
[297] Yu J, Wang S, Low J, Xiao W. Enhanced photocatalytic performance of direct Z-scheme gC 3 N 4–TiO 2 photocatalysts for the decomposition of formaldehyde in air. Phys Chem Chem Phys 2013;15(39):16883–90.
[298] Zhang E, Zhu Q, Huang J, Liu J, Tan G, Sun C, Li T, Liu S, Li Y, Wang H, Wan X. Visually resolving the direct Z-scheme heterojunction in CdS@ ZnIn2S4 hollow cubes for photocatalytic evolution of H2 and H2O2 from pure water. Appl Catal, B 2021;293:120213.
[299] Mahmood W, Ali J, Zahid I, Thomas A, ul Haq A. Optical and electrical studies of CdS thin films with thickness variation. Optik 2018;158:1558–66.
[300] Zhang L, Hao X, Jian Q, Jin Z. Ferrous oxalate dehydrate over CdS as Z-scheme photocatalytic hydrogen evolution. J Solid State Chem 2019;274:286–94.
[301] Hu T, Li P, Zhang J, Liang C, Dai K. Highly efficient direct Z-scheme WO3/CdS-diethylenetriamine photocatalyst and its enhanced photocatalytic H2 evolution under visible light irradiation. Appl Surf Sci 2018;442:20–9.
[302] Cui H, Li B, Zhang Y, Zheng X, Li X, Li Z, Xu S. Constructing Z-scheme based CoWO4/CdS photocatalysts with enhanced dye degradation and H2 generation performance. Int J Hydrogen Energy 2018;43(39):18242–52.
[303] Li CQ, Du X, Jiang S, Liu Y, Niu ZL, Liu ZY, Yi SS, Yue XZ. Constructing direct Z-scheme heterostructure by enwrapping ZnIn2S4 on CdS hollow cube for efficient photocatalytic H2 generation. Adv Sci 2022;9(24):2201773.
[304] Guo F, Sun H, Shi Y, Zhou F, Shi W. CdS nanoparticles decorated hexagonal Fe2O3 nanosheets with a Z-scheme photogenerated electron transfer path for improved visible-light photocatalytic hydrogen production. Chin J Chem Eng 2022;43:266–74.
[305] Yin XL, Li LL, Gao GM, Lu Y, Shang QQ, Zhao HT, Li DC, Dou JM. Direct Z-Scheme NiWO4/CdS nanosheets-on-nanorods nanoheterostructure for efficient visible-light-driven H2 generation. Int J Hydrogen Energy 2022;47(17):9895–904.
[306] Liang S, Sui G, Li J, Guo D, Luo Z, Xu R, Yao H, Wang C, Chen S. ZIF-L-derived porous C-doped ZnO/CdS graded nanorods with Z-scheme heterojunctions for enhanced photocatalytic hydrogen evolution. Int J Hydrogen Energy 2022;47(21):11190–202.
[307] Song T, Wang J, Su L, Xu H, Bai X, Zhou L, Tu W. Promotion effect of rhenium on MoS2/ReS2@ CdS nanostructures for photocatalytic hydrogen production. Mol Catal 2021;516:111939.
[308] Zhou FQ, Fan JC, Xu QJ, Min YL. BiVO4 nanowires decorated with CdS nanoparticles as Z-scheme photocatalyst with enhanced H2 generation. Appl Catal, B 2017;201:77–83.
[309] Wang J, Yu L, Wang Z, Wei W, Wang K, Wei X. Constructing 0D/2D Z-scheme heterojunction of CdS/gC 3 N 4 with enhanced photocatalytic activity for H 2 evolution. Catal Lett 2021:1–2.
[310] Li W, Fang K, Zhang Y, Chen Z, Wang L, Bu Y. Fabrication of 1D/2D CdS/CoSx direct Z-scheme photocatalyst with enhanced photocatalytic hydrogen evolution performance. Int J Hydrogen Energy 2021;46(14):9351–9.
[311] Feng C, Chen Z, Jing J, Sun M, Han J, Fang K, Li W. Synergistic effect of hierarchical structure and Z-scheme heterojunction constructed by CdS nanoparticles and nanoflower-structured Co9S8 with significantly enhanced photocatalytic hydrogen production performance. J Photochem Photobiol, A 2021;409:113160.
[312] Xue C, Zhang P, Shao G, Yang G. Effective promotion of spacial charge separation in direct Z-scheme WO3/CdS/WS2 tandem heterojunction with enhanced visible-light-driven photocatalytic H2 evolution. Chem Eng J 2020;398:125602.
[313] Sheng J, Wang C, Duan F, Yan S, Lu S, Zhu H, Du M, Chen X, Chen M. Direct Z-scheme CdS–NiPc heterojunctions as noble metal-free photocatalysts for enhanced photocatalytic hydrogen evolution. Catal Sci Technol 2021;11(23):7683–93.
[314] Li Z, Chen H, Li Y, Wang H, Liu Y, Li X, Lin H, Li S, Wang L. Porous direct Z-scheme heterostructures of S-deficient CoS/CdS hexagonal nanoplates for robust photocatalytic H 2 generation. CrystEngComm 2022;24(2):404–16.
[315] Liu X, Dai D, Cui Z, Zhang Q, Gong X, Wang Z, Liu Y, Zheng Z, Cheng H, Dai Y, Huang B. Optimizing the reaction pathway by active site regulation in the CdS/Fe2O3 Z-scheme heterojunction system for highly selective photocatalytic benzylamine oxidation integrated with H2 production. ACS Catal 2022;12(19):12386–97.
[316] Bao T, Tang C, Li S, Qi Y, Zhang J, She P, Rao H, Qin JS. Hollow structured CdS@ZnIn2S4 Z-scheme heterojunction for bifunctional photocatalytic hydrogen evolution and selective benzylamine oxidation. J Colloid Interface Sci 2024;659:788–98.
[317] Zhu B, Li N, Huo L, Dong Q, Huang L, Ma J. Fabrication of Co2RuS6/CdS Z-scheme heterojunction with sulfur vacancy for enhanced piezo-photocatalytic H2 evolution and in-depth analysis of charge-separation mechanism. Int J Hydrogen Energy 2024;51:1267–76.
[318] Li P, Yan X, Gao S, Cao R. Boosting photocatalytic hydrogen production coupled with benzyl alcohol oxidation over CdS/metal–organic framework composites. Chem Eng J 2021;421:129870.
[319] Feng Y, Li J, Ye S, Gao S, Cao R. Growing COFs in situ on CdS nanorods as core–shell heterojunctions to improve the charge separation efficiency. Sustain Energy Fuels 2022;6(22):5089–99.
[320] Ran Y, Cui Y, Zhang Y, Fang Y, Zhang W, Yu X, Lan H, An X. Assembly-synthesis of puff pastry-like g-C3N4/CdS heterostructure as S-junctions for efficient photocatalytic water splitting. Chem Eng J 2022;431:133348.
[321] Zhang L, Jiang X, Jin Z, Tsubaki N. Spatially separated catalytic sites supplied with the CdS–MoS 2–In 2 O 3 ternary dumbbell S-scheme heterojunction for enhanced photocatalytic hydrogen production. J Mater Chem A 2022;10(19):10715–28.
[322] Liu Y, Wan J, Wu G, Qin F, Wang X, Sun Q, Yao D, Kan J. Template-free synthesized porous ZnO-CdS spherical-shell S-scheme heterostructure assisted with Pt nanoparticle for enhanced photocatalytic H2-production. Mater Sci Eng B 2024;301:117127.
[323] Liu Y, Lu H, Qin F, Wan J, Wu G, Deng L, Sun Q, Wang X, Yao D, Kan J. Flower-shaped S-scheme CdS-ZnO nanorods heterojunction assisted with SPR of low-content Au for accelerating photocatalytic hydrogen production. Int J Hydrogen Energy 2024;58:302–9.
[324] Li H, Li X, Que L, Xu X, Cao J, Pan J, Zhu M. S-scheme core-shell nanorods heterojunction of g-C3N4 quantum dots modified Er: WO3/CdS towards visible light H2 evolution via up-conversion fluorescence synergism. Int J Hydrogen Energy 2024;51:1440–50.
[325] Güy N, Atacan K, Özacar M. Rational construction of pnp CuO/CdS/CoWO4 S-scheme heterojunction with influential separation and directional transfer of interfacial photocarriers for boosted photocatalytic H2 evolution. Renew Energy 2022;195:107–20.
[326] Wu H, Zhao L, He X, Chen H, Fang W, Du X, Li W, Wang D. Boosted charge carrier concentration via luminescent quenching of photoexcited electrons in CdS/FI S-scheme heterostructures for efficient photocatalytic hydrogen production. J Clean Prod 2023;425:138921.
[327] Lu H, Liu Y, Zhang S, Wan J, Wang X, Deng L, Kan J, Wu G. Clustered tubular S-scheme ZnO/CdS heterojunctions for enhanced photocatalytic hydrogen production. Mater Sci Eng B 2023;289:116282.
[328] Sun L, Li L, Yang J, Fan J, Xu Q. Fabricating covalent organic framework/CdS S-scheme heterojunctions for improved solar hydrogen generation. Chin J Catal 2022;43(2):350–8.
[329] Chen D, Li X, Dai K, Zhang J, Dawson G. Microwave-assisted synthesis of organic–inorganic hybrid porous g-C3N4/CdS–diethylenetriamine S-scheme heterojunctions with enhanced visible light hydrogen production. J Phys D Appl Phys 2022;55(24):244001.
[330] Sun L, Yu X, Tang L, Wang W, Liu Q. Hollow dodecahedron K3PW12O40/CdS core-shell S-scheme heterojunction for photocatalytic synergistic H2 evolution and benzyl alcohol oxidation. Chin J Catal 2023;52:164–75.

[331] Fan L, Han J, Wei K, Ma C, Feng S, Zhou Y, Dai X, Ye Z, Wang Y. Mn-doped CdS/Cu2O: an S-scheme heterojunction for photocatalytic hydrogen production. J Alloys Compd 2023;960:170382.
[332] Orlianges JC, Champeaux C, Dutheil P, Catherinot A, Mejean TM. Structural, electrical and optical properties of carbon-doped CdS thin films prepared by pulsed-laser deposition. Thin Solid Films 2011;519(21):7611–4.
[333] Jang JS, Ji SM, Bae SW, Son HC, Lee JS. Optimization of CdS/TiO2 nano-bulk composite photocatalysts for hydrogen production from Na2S/Na2SO3 aqueous electrolyte solution under visie light (λ≥ 420 nm). J Photochem Photobiol, A 2007;188(1):112–9.
[334] Liu S, Chen Z, Zhang N, Tang ZR, Xu YJ. An efficient self-assembly of CdS nanowires–reduced graphene oxide nanocomposites for selective reduction of nitro organics under visible light irradiation. J Phys Chem C 2013;117(16):8251–61.
[335] Jia L, Wang DH, Huang YX, Xu AW, Yu HQ. Highly durable N-doped graphene/CdS nanocomposites with enhanced photocatalytic hydrogen evolution from water under visible light irradiation. J Phys Chem C 2011;115(23):11466–73.
[336] Dreyer DR, Todd AD, Bielawski CW. Harnessing the chemistry of graphene oxide. Chem Soc Rev 2014;43(15):5288–301.
[337] Zeng P, Zhang Q, Peng T, Zhang X. One-pot synthesis of reduced graphene oxide–cadmium sulfide nanocomposite and its photocatalytic hydrogen production. Phys Chem Chem Phys 2011;13(48):21496–502.
[338] Hong Y, Shi P, Wang P, Yao W. Improved photocatalytic activity of CdS/reduced graphene oxide (RGO) for H2 evolution by strengthening the connection between CdS and RGO sheets. Int J Hydrogen Energy 2015;40(22):7045–51.
[339] Zubair M, Vanhaecke EM, Svenum IH, Rønning M, Yang J. Core-shell particles of C-doped CdS and graphene: a noble metal-free approach for efficient photocatalytic H2 generation. Green Energy Environ 2020;5(4):461–72.
[340] Sakizadeh J, Cline JP, Snyder MA, Kiely CJ, McIntosh S. Tailored coupling of biomineralized CdS quantum dots to rGO to realize ambient aqueous synthesis of a high-performance hydrogen evolution photocatalyst. ACS Appl Mater Interfaces 2020;12(38):42773–80.
[341] Tang S, Xia Y, Fan J, Cheng B, Yu J, Ho W. Enhanced photocatalytic H2 production performance of CdS hollow spheres using C and Pt as bi-cocatalysts. Chin J Catal 2021;42(5):743–52.
[342] Zhu C, Liu CA, Fu Y, Gao J, Huang H, Liu Y, Kang Z. Construction of CDs/CdS photocatalysts for stable and efficient hydrogen production in water and seawater. Appl Catal, B 2019;242:178–85.
[343] Deng L, Li Y, Zhang Z, Zhang Y, Zhong J, Zhang C, Zhang H, Zhuang C. In situ growth of ultrathin CdS nanosheets on porous carbon aerogels for improved photocatalytic H2 production. ACS Appl Nano Mater 2023;6(17):16009–15.
[344] Chen C, Huang Y, Huo S. Preparation and photocatalytic H2 production property of graphene oxide/CdS/single crystal ZnO nanorod ternary hybrids. Vacuum 2022;205:111467.
[345] An H, Yan X, Li H, Yang B, Wei J, Yang G. Increased active sites by in situ growth of CoP quantum dots on CdS/rGO to achieve efficient photocatalytic H2 production. ACS Appl Energy Mater 2019;2(6):4195–204.
[346] Ali MB, Jo WK, Elhouichet H, Boukherroub R. Reduced graphene oxide as an efficient support for CdS-MoS2 heterostructures for enhanced photocatalytic H2 evolution. Int J Hydrogen Energy 2017;42(26):16449–58.
[347] Wang JJ, Wang J, Feng K, Zhang HH, Li ZJ, Liu B, Tung CH, Wu LZ. Enhanced visible-light-driven hydrogen generation by in situ formed photocatalyst RGO–CdS–Ni x S from metal salts and RGO–CdS composites. J Mater Chem A 2017;5(20):9537–43.
[348] Hareesh K, Dhole SD, Phase DM, Williams JF. One-step bacterial assisted synthesis of CdS/rGO nanocomposite as Hydrogen production catalyst. Mater Res Bull 2019;110:82–9.
[349] Yin XL, Li LL, Li DC, Dou JM. One-pot synthesis of CdS-MoS2/RGO-E nano-heterostructure with well-defined interfaces for efficient photocatalytic H2 evolution. Int J Hydrogen Energy 2018;43(45):20382–91.
[350] Mandal S, Sarkar A, Mukherjee P, Das S, Banerjee D, Ganguly S, Kargupta K. Organic alginate encapsulated rGO-CdS millispheres for remarkable photocatalytic solar hydrogen production. Int J Hydrogen Energy 2024;51:1167–85.
[351] Yan Z, Yu X, Han A, Xu P, Du P. Noble-metal-free Ni (OH) 2-modified CdS/reduced graphene oxide nanocomposite with enhanced photocatalytic activity for hydrogen production under visible light irradiation. J Phys Chem C 2014;118(40):22896–903.
[352] Tonda S, Kumar S, Gawli Y, Bhardwaj M, Ogale S. g-C3N4 (2D)/CdS (1D)/rGO (2D) dual-interface nano-composite for excellent and stable visible light photocatalytic hydrogen generation. Int J Hydrogen Energy 2017;42(9):5971–84.
[353] Li L, Wu J, Liu B, Liu X, Li C, Gong Y, Huang Y, Pan L. NiS sheets modified CdS/reduced graphene oxide composite for efficient visible light photocatalytic hydrogen evolution. Catal Today 2018;315:110–6.
[354] Xue M, Dong Y, Ye X, Guan X, Guo L. A cation exchange strategy to construct highly dispersed copper-doped CdS nanoparticles for photocatalytic hydrogen production. nt. J Hydrogen Energy 2024;87:1110–20.
[355] Zhang X, Puttaswamy M, Bai H, Hou B, Verma SK. CdS/ZnS core–shell nanorod heterostructures co-deposited with ultrathin MoS2 cocatalyst for competent hydrogen evolution under visible-light irradiation. J Colloid Interface Sci 2024;665:430–42.
[356] Kumaravel V, Imam MD, Badreldin A, Chava RK, Do JY, Kang M, Abdel-Wahab A. Photocatalytic hydrogen production: role of sacrificial reagents on the activity of oxide, carbon, and sulfide catalysts. Catalysts 2019;9(3):276.
[357] Qin Y, Li H, Lu J, Meng F, Ma C, Yan Y, Meng M. Nitrogen-doped hydrogenated TiO2 modified with CdS nanorods with enhanced optical absorption, charge separation and photocatalytic hydrogen evolution. Chem Eng J 2020;384:123275.
[358] Meissner D, Benndorf C, Memming R. Photocorrosion of cadmium sulfide: analysis by photoelectron spectroscopy. Appl Surf Sci 1987;27(4):423–36.
[359] Chen Y, Zhong W, Chen F, Wang P, Fan J, Yu H. Photoinduced self-stability mechanism of CdS photocatalyst: the dependence of photocorrosion and H2-evolution performance. J Mater Sci Technol 2022;121:19–27.
[360] Zhang S, Sun S, Song L, Liu E. Chiral induction enhances hydrogen generation performance of CdS quantum dots. Int J Hydrogen Energy 2023;48(87):33903–12.
[361] Sun G, Xiao B, Zheng H, Shi JW, Mao S, He C, Li Z, Cheng Y. Ascorbic acid functionalized CdS–ZnO core–shell nanorods with hydrogen spillover for greatly enhanced photocatalytic H 2 evolution and outstanding photostability. J Mater Chem A 2021;9(15):9735–44.
[362] Ning X, Zhen W, Wu Y, Lu G. Inhibition of CdS photocorrosion by Al2O3 shell for highly stable photocatalytic overall water splitting under visible light irradiation. Appl Catal, B 2018;226:373–83.
[363] Fang X, Song J, Pu T, Wang C, Yin C, Wang J, Kang S, Shi H, Zuo Y, Wang Y, Cui L. Graphitic carbon nitride-stabilized CdS@ CoS nanorods: an efficient visible-light-driven photocatalyst for hydrogen evolution with enhanced photo-corrosion resistance. Int J Hydrogen Energy 2017;42(47):28183–92.
[364] Zhou W, Li F, Yang X, Yang W, Wang C, Cao R, Zhou C, Tian M. Peanut-chocolate-ball-inspired construction of the interface engineering between CdS and intergrown Cd: boosting both the photocatalytic activity and photocorrosion resistance. J Energy Chem 2023;76:75–89.
[365] Liu X, Xu J, Jiang Y, Du Y, Zhang J, Lin K. In-situ construction of CdS@ ZIS Z-scheme heterojunction with core-shell structure: defect engineering, enhance photocatalytic hydrogen evolution and inhibit photo-corrosion. Int J Hydrogen Energy 2022;47(83):35241–53.
[366] Wu C, Huang W, Liu H, Lv K, Li Q. Insight into synergistic effect of Ti3C2 MXene and MoS2 on anti-photocorrosion and photocatalytic of CdS for hydrogen production. Appl Catal, B 2023;330:122653.
[367] Liu Y, Ma X, Wang H, Li Y, Jin Z. CdS photocorrosion protection by MoSe 2 modification for photocatalytic hydrogen production. Catal Surv Asia 2019;23:231–44.
[368] Wang C, Wang L, Jin J, Liu J, Li Y, Wu M, Chen L, Wang B, Yang X, Su BL. Probing effective photocorrosion inhibition and highly improved photocatalytic hydrogen production on monodisperse PANI@ CdS core-shell nanospheres. Appl Catal, B 2016;188:351–9.
[369] Zhong Y, Zhao G, Ma F, Wu Y, Hao X. Utilizing photocorrosion-recrystallization to prepare a highly stable and efficient CdS/WS2 nanocomposite photocatalyst for hydrogen evolution. Appl Catal, B 2016;199:466–72.
[370] Liu Q, Wang S, Ren Q, Li T, Tu G, Zhong S, Zhao Y, Bai S. Stacking design in photocatalysis: synergizing cocatalyst roles and anti-corrosion functions of metallic MoS 2 and graphene for remarkable hydrogen evolution over CdS. J Mater Chem A 2021;9(3):1552–62.
[371] Irfan RM, Tahir MH, Nadeem M, Maqsood M, Bashir T, Iqbal S, Zhao J, Gao L. Fe3C/CdS as noble-metal-free composite photocatalyst for highly enhanced photocatalytic H2 production under visible light. Appl Catal, A 2020;603:117768.
[372] Lu Y, Cheng X, Tian G, Zhao H, He L, Hu J, Wu SM, Dong Y, Chang GG, Lenaerts S, Siffert S. Hierarchical CdS/m-TiO2/G ternary photocatalyst for highly active visible light-induced hydrogen production from water splitting with high stability. Nano Energy 2018;47:8–17.
[373] Liu X, Zhang T, Li Y, Zhang J, Du Y, Yang Y, Jiang Y, Lin K. CdS@ Polydopamine@ SnO2-x sandwich structure with electrostatic repulsion effect and oxygen deficiency: enhanced photocatalytic hydrogen evolution activity and inhibited photo-corrosion. Chem Eng J 2022;434:134602.
[374] Wu K, Wu P, Zhu J, Liu C, Dong X, Wu J, Meng G, Xu K, Hou J, Liu Z, Guo X. Synthesis of hollow core-shell CdS@ TiO2/Ni2P photocatalyst for enhancing hydrogen evolution and degradation of MB. Chem Eng J 2019;360:221–30.
[375] Zhou X, Zhang N, Yin L, Zhao Y, Zhang B. Few-layered WS2 nanosheets onto 1D CdS@ ZnCdS as efficient visible-light photocatalyst for hydrogen evolution. Ceram Int 2020;46(16):26100–8.
[376] Li S, Wang L, Li Y, Zhang L, Wang A, Xiao N, Gao Y, Li N, Song W, Ge L, Liu J. Novel photocatalyst incorporating Ni-Co layered double hydroxides with P-doped CdS for enhancing photocatalytic activity towards hydrogen evolution. Appl Catal, B 2019;254:145–55.
[377] Lei Y, Ng KH, Zhu Y, Zhang Y, Li Z, Xu S, Huang J, Hu J, Chen Z, Cai W, Lai Y. Mo-activated VC as effective cocatalyst for an enhanced photocatalytic hydrogen evolution activity of CdS. Chem Eng J 2023;452:139325.
[378] Lv J, Zhang J, Liu J, Li Z, Dai K, Liang C. Bi SPR-promoted Z-scheme Bi2MoO6/CdS-diethylenetriamine composite with effectively enhanced visible light photocatalytic hydrogen evolution activity and stability. ACS Sustainable Chem Eng 2018;6(1):696–706.
[379] Schröder M, Kailasam K, Borgmeyer J, Neumann M, Thomas A, Schomäcker R, Schwarze M. Hydrogen evolution reaction in a large-scale reactor using a carbon nitride photocatalyst under natural sunlight irradiation. Energy Technol 2015;3(10):1014–7.
[380] Domen K, Naito S, Onishi T, Tamaru K. Photocatalytic hydrogen production from a mixture of water and 2-propanol on some semiconductors. Chem Lett 1982;11(4):555–8.
[381] Kambe S, Fujii M, Kawai T, Kawai S, Nakahara F. Photocatalytic hydrogen production with Cd (S, Se) solid solution particles: determining factors for the highly efficient photocatalyst. Chem Phys Lett 1984;109(1):105–9.

[382] Yoshimura J, Tanaka A, Kondo JN, Domen K. Visible light induced hydrogen evolution on CdS/K4Nb6O17 photocatalyst. Bull Chem Soc Jpn 1995;68(8):2439–45.
[383] Yu ZG, Pryor CE, Lau WH, Berding MA, MacQueen DB. Core-shell nanorods for efficient photoelectrochernical hydrogen production. Hydrogen Cycle-Gen Storage Fuel Cell 2006;885:273.
[384] Bao N, Shen L, Takata T, Lu D, Domen K. Highly ordered Pt-loaded CdS nanowire arrays for photocatalytic hydrogen production under visible light. Chem Lett 2006;35(3):318–9.
[385] Wang Y, Wang Y, Xu R. Synthesis of Zn–Cu–Cd sulfide nanospheres with controlled copper locations and their effects on photocatalytic activities for H2 production. Int J Hydrogen Energy 2010;35(11):5245–53.
[386] Jang JS, Ji SM, Lee JS, Li W, Oh SH. Anoxic hydrogen production over CdS-based composite photocatalysts under visible light irradiation (λ≥ 420nm). Stud Surf Sci Catal 2006:201–4.
[387] Ke D, Liu S, Dai K, Zhou J, Zhang L, Peng T. CdS/regenerated cellulose nanocomposite films for highly efficient photocatalytic H2 production under visible light irradiation. J Phys Chem C 2009;113(36):16021–6.
[388] Yu J, Zhang J, Jaroniec M. Preparation and enhanced visible-light photocatalytic H 2-production activity of CdS quantum dots-sensitized Zn 1− x Cd x S solid solution. Green Chem 2010;12(9):1611–4.
[389] Kale BB, Baeg JO, Apte SK, Sonawane RS, Naik SD, Patil KR. Confinement of nano CdS in designated glass: a novel functionality of quantum dot–glass nanosystems in solar hydrogen production. J Mater Chem 2007;17(40):4297–303.
[390] Repo E, Rengaraj S, Pulkka S, Castangnoli E, Suihkonen S, Sopanen M, Sillanpää M. Photocatalytic degradation of dyes by CdS microspheres under near UV and blue LED radiation. Sep Purif Technol 2013;120:206–14.
[391] Fang J, Gu J, Liu Q, Zhang W, Su H, Zhang D. Three-dimensional CdS/Au butterfly wing scales with hierarchical rib structures for plasmon-enhanced photocatalytic hydrogen production. ACS Appl Mater Interfaces 2018;10(23):19649–55.

List of Abbreviations

0D: = Zero-dimensional
1D: = One-dimensional
2D: = Two-dimensional
3D: = Three-dimensional
ALD: = Atomic layer deposition
AQY: = Apparent quantum yield
AQE: = Apparent quantum efficiency
BET: = Brunauer, Emmett and Teller
CB: = Conduction band
CdS/CA: = Cysteamine-capped CdS
CdS: = Cadmium sulfide
CdS-MC: = CdS–MoS2/C
CF: = CdS/α-Fe_2O_3
CNTs: = Carbon nanotubes
COFs: = Covalent organic frameworks
Co-Pi: = Cobalt-phosphate
CQDs: = Carbon quantum dots
CSZS-VZn: = Zn-vacancy defect-mediated CdS/ZnS
CV: = Crystal violet
CW40: = 40 wt% CdS/$W_{18}O_{49}$
DDA: = Dodecylamine
DETA: = Diethylenetriamine
DFT: = Density Functional Theory
e^-: = Electron
ECB: = Conduction band potential
EF: = Fermi energy
E_{Fm}: = Energy of Fermi level of metal
E_{Fs}: = Energy of Fermi level of semiconductor
EIS: = Electro-chemical impedance spectroscopy
eV: = Electron volt
G: = Graphene
g-C_3N_4: = Graphitic carbon nitride
GO: = Graphene oxide
h^+: = holes
H^+: = Proton
HER: = Hydrogen evolution reaction
HNPs: = Hollow NPs
HOMO: = Highest occupied molecular orbital
HS: = Hollow spheres
HZB: = Helmholtz-Zentrum Berlin
KJ: = Kilo-Joule
LA: = Lactic acid
LED: = Light emitting diode
LSPR: = Localized surface plasmon resonance
MC-CdS: = Mesoporous carbon-CdS
MMCS: = MnS/Mn0·2Cd0·8S
MOF: = Metal organic framework
MPCx: = Metal phosphorous chalcogenides
MSs: = Metal sulfides
MWCNTs: = Multi-walled carbon nanotubes
MXenes: = Transition metal carbides
N–C: = N-doped carbon
NCs: = Nanocrystals
NF: = Ni-foam
NFs: = Nanoframes
NHE: = Normal Hydrogen Electrode
NIR: = Near-infrared
nm: = Nanometer
NPs: = Nanoparticles
NRs: = Nanorods
NSs: = Nanosheets
NTs: = Nanotubes
NWs: = Nanowires
OER: = Oxygen evolution reaction
OP: = Oxidation photocatalyst
PANI: = Polyaniline
PC: = Photocatalyst
PL: = Photo-luminescence
PRGO: = Polymer reduced graphene oxide
PSGM: = Polymer-supported graphene microsphere
PT: = Pyrene-alttriphenylamine
PVP: = Polyvinylpyrrolidone
QDs: = Quantum Dots
QE: = Quantum Efficiency
φ_b: = Barrier's height
QY: = Quantum yield
Rct: = Arc radius
rGO: = Reduced graphene oxide
RP: = Reduction photocatalyst
SAs: = Single atoms
SC: = Semiconductor

SHE= Standard Hydrogen Electrode
SPP: = Surface plasmon polariton
STH: = Solar to Hydrogen conversion efficiency
SWCNT: = Single-wall carbon nanotube
TEOA: = Triethanolamine
TMDC: = Transition metal-based dichalcogenides
TMPs: = Transition metal phosphides
TON: = Turn over number
UV: = Ultraviolet
VB: = Valance band
VCC: = V_2O_5/CdS/CoS_2
W_{Fm}: = Work function of metal
W_{Fs}: = Work function of semiconductor
XPS: = X-ray photoelectron spectroscopy
X_s: = Electron affinity
ZIS: = ZnIn2S4/CdS
Zn-TCPP: = Zn-porphyrin NSs
ZP48: = NaY zeolite